Fall 1-22-2014

Revisiting Volcanology and Composition of Rhyolites and Associated REE Rich Mafic Clasts of the Three Fingers Caldera, SE Oregon

Phillip Ira Marcy
Portland State University

Revisiting Volcanology and Composition of Rhyolites and Associated REE Rich Mafic Clasts of the Three Fingers Caldera, SE Oregon

by

Phillip Ira Marcy

A thesis submitted in partial fulfillment of the
requirements for the degree of

Master of Science
in
Geology

Thesis Committee:
Martin J. Streck, Chair
Michael L. Cummings
Robert B. Perkins

Portland State University
2013

Abstract

Two adjacent caldera systems, the Mahogany Mountain and the Three Fingers caldera constitute voluminous rhyolitic volcanic deposits on the eastern margin of the Oregon-Idaho graben during the middle-Miocene. Both calderas are part of the Lake Owyhee volcanic field that in turn is part of widespread rhyolite deposits associated with the Columbia River Basalt province. We focus on establishing relationships between intracaldera units of Three Fingers caldera and caldera-forming tuff of Spring Creek and surveying the distribution of entrained mafic clasts which often display anomalous concentrations of rare earth elements.

Previous mapping identified two intra-caldera facies and one outflow facies of the tuff of Spring Creek, in addition to a younger rhyolite within the caldera (Trp). New $^{40}Ar/^{39}Ar$ dates show these units are nearly time equivalent at 15.64 ± 0.08 Ma for Trp and 15.64 ± 0.09 Ma for tuff of Spring Creek. Field evidence shows extensive coverage of Trp and associated facies emplaced after a period of sedimentation within the caldera. The main reinterpretations are: i) the mostly devitrified units of Trp are time equivalent to flows and domes of glassy, vesicular, or brecciated rhyolite previously mapped as intra-caldera tuff of Spring Creek; and ii) mafic clasts present in dense glass

and porous rhyolite are fragments of mafic lava flows entrained by the subsequent eruptions.

New geochemical and mineralogical evidence clearly distinguish the outflow tuff of Spring Creek and intracaldera rhyolites. Compared to the outflow tuff, intracaldera rhyolite flows are less Fe-rich, (2 vs. 3 wt.% FeO), and higher silica (77 vs. 74 wt.% SiO_2) rhyolites that lack vitrophyric texture. I interpret the investigated area as a rhyolite dome field, erupted subsequent to caldera collapse. The proximity of vents resulted in a complex stratigraphic overlap of rhyolite flows and clastic debris issued from coalescing domes. The predominance of high-standing dome interiors reflects the more resistant nature of dense devitrified rhyolite as compared to pumiceous, glassy, or brecciated facies of intra-caldera rhyolite.

Enrichment of REE in mafic clasts is highly variable, and does not correlate with their entrainment in a specific facies of intra-caldera rhyolite. Individual clasts contain up to 2400 ppm Nd, 1800 ppm Ce, and 1400 ppm La in the most enriched samples. Linear regression shows these highly anomalous concentrations are not correlated with variations in major element chemistry between enriched and un-enriched clasts. The geographic extent of mafic clast-bearing units is limited to less than 5 percent of the

area mapped, and their distribution within these units is typically volumetrically insignificant, limiting their economic potential. Mechanisms for enrichment of REE within these rocks is however significant to our understanding of a yet unexplained phenomenon and may lead to further discoveries with greater economic potential.

ACKNOWLEDGEMENTS

I would especially like to thank my advisor, Dr. Martin J. Streck for his patience and guidance throughout this study, and for providing me with the spark of curiosity since my arrival at PSU. I would also like to thank Dr. Robert Perkins for his assistance in the laboratory, and Dr. Michael Cummings for keeping a watchful eye on my use of the English language.

The field portion of this study was made possible by patience and endurance of my field assistants, Kathy Breen, Adam Large, and Matthew Gibson, who did not hesitate to join me in a harsh and unfriendly landscape. I am grateful for the hard work of fellow students Ellie Brown and Brian Webb, who provided me with microprobe data and the insight to understand it. Nancy Eriksson deserves special thanks for her detailed and personal assistance, without which I and so many others would be lost.

Nobody has been more important to me in the pursuit of this project than the members of my family. I would like to thank my parents and my brother, who continue to support and encourage me in all that I pursue. Most of all, I wish to thank my loving and supportive wife, Amy, and my three wonderful children, Evan, Alex, and Abby, for their continued love and inspiration.

Table of Contents

List of Figures

List of Tables

Introduction

Three Fingers caldera is a middle-Miocene silicic center, considered part of the Lake Owyhee volcanic field (LOVF), as defined by Rytuba et al., (1991). Mahogany Mountain caldera is located only 5 km to the southwest and is also part of the LOVF. Both calderas are positioned on the eastern flank of the Oregon-Idaho graben (OIG) (Cummings et al., 2000). The subsidence of the OIG is contemporaneous with the most voluminous silicic eruptions in the area, following the most significant eruptions of Columbia River Basalt and Steens Basalt (Camp et al,, 2003).

The Three Fingers Rock 7.5' quadrangle was initially mapped by Vander Meulen et al. (1986, 1989) who mapped a post-collapse, intra-caldera rhyolite and the presence of 'basalt bombs' within the intra-caldera fill sequence, with select samples containing anomalously high REE (Vander Meulen et al., 1991; Ferns and Cummings, 1996). The most aerially extensive unit on the Three Fingers Rock quadrangle map is the tuff of Spring Creek, whose eruption resulted in the collapse of Three Fingers caldera at 15.4 Ma (Rytuba et al., 1991). A detailed geochemical investigation of later erupted intra-caldera rhyolites has not been performed, and existing age dates are older K/Ar analyses.

Increasing demand for rare earth elements (REE) in a wide variety of high-tech applications, in addition to recent export quotas applied by China for the year 2011 (Reuters, 2010) highlight the importance of investigating potential sources of REE and the processes by which they are concentrated. High concentrations of REE in preliminary studies (Erickson et al., 1986; Hageman et al., 1993; Ferns and Cummings, 1996) indicate that Three Fingers caldera may be a viable REE resource. Studies of stream sediments draining the caldera show abundances as high as 5000 ppm yttrium and 2000 ppm lanthanum in some samples (Erickson et al., 1986; Hageman et al., 1993). Surveys by Ferns and Cummings (unpublished report, 1996) and Vander Meulen et al. (1986, 1989), showed up to 1500 ppm cerium in 'mafic clots' within what was mapped as intra-caldera Spring Creek Tuff. Such high concentrations are considered ore-grade deposits, and are the basis for this further study to determine the distribution, abundance, and likely processes concentrating REE in rocks of the Three Fingers Caldera.

The purpose of this study is to determine the aerial extent and geologic relations of eruptive units of Three Fingers caldera and assess the distribution of REE-rich rocks within the caldera to determine likely processes for REE enrichment. In addition, we

obtain absolute age dates using the $^{40}Ar/^{39}Ar$ method at Oregon State University to place the eruptions of the tuff of Spring Creek and intra-caldera rhyolites in the proper timeframe of regional volcanism. The study area was mapped during the summers of 2011 and 2012, leading to the production of a 1:24,000 geologic map (unpublished). Geochemical data is here compiled from 56 total analyses of mafic clasts and 32 analyses of units from the Three Fingers/Mahogany Mountain area. Samples collected for this study and nearby studies of Martin Streck and students were analyzed using X-ray fluorescence (XRF) and inductively coupled plasma mass spectrometry (ICP-MS) at Washington State University, ICP-OES at Portland State University, with three unpublished analyses included from the thesis work of Brian Zimmerman (written communication with Mark Ferns, 1990) provided by Mark Ferns (written communication, 2011). The resulting map and geochemical data allow for determination of the location of REE-rich rocks within the caldera system. Observed chemical and mineralogical data are compared with established petrologic and hydrothermal models to determine the likely processes leading to enrichment of REE.

Location

Middle-Miocene Three Fingers caldera is located in Malheur County, Oregon, directly to the east of Lake Owyhee, about 38 km southwest of Caldwell, Idaho and 62 km south of Ontario, Oregon (Figure 1). This structure is accompanied by nearby Mahogany Mountain caldera about 5 km to the southwest, and is part of a regional axis of mid-Miocene silicic volcanism along the eastern margin of the north-south trending, 50 km wide Oregon-Idaho graben (Ferns, 1997; Cummings et al., 2000). Topography ranges from about 1000 to 1400 meters in elevation, and is dominated by north trending ridges and deeply eroded canyons. The drainage of the area is primarily toward the west, where it empties into the Owyhee Reservoir (Erickson et al., 1986).

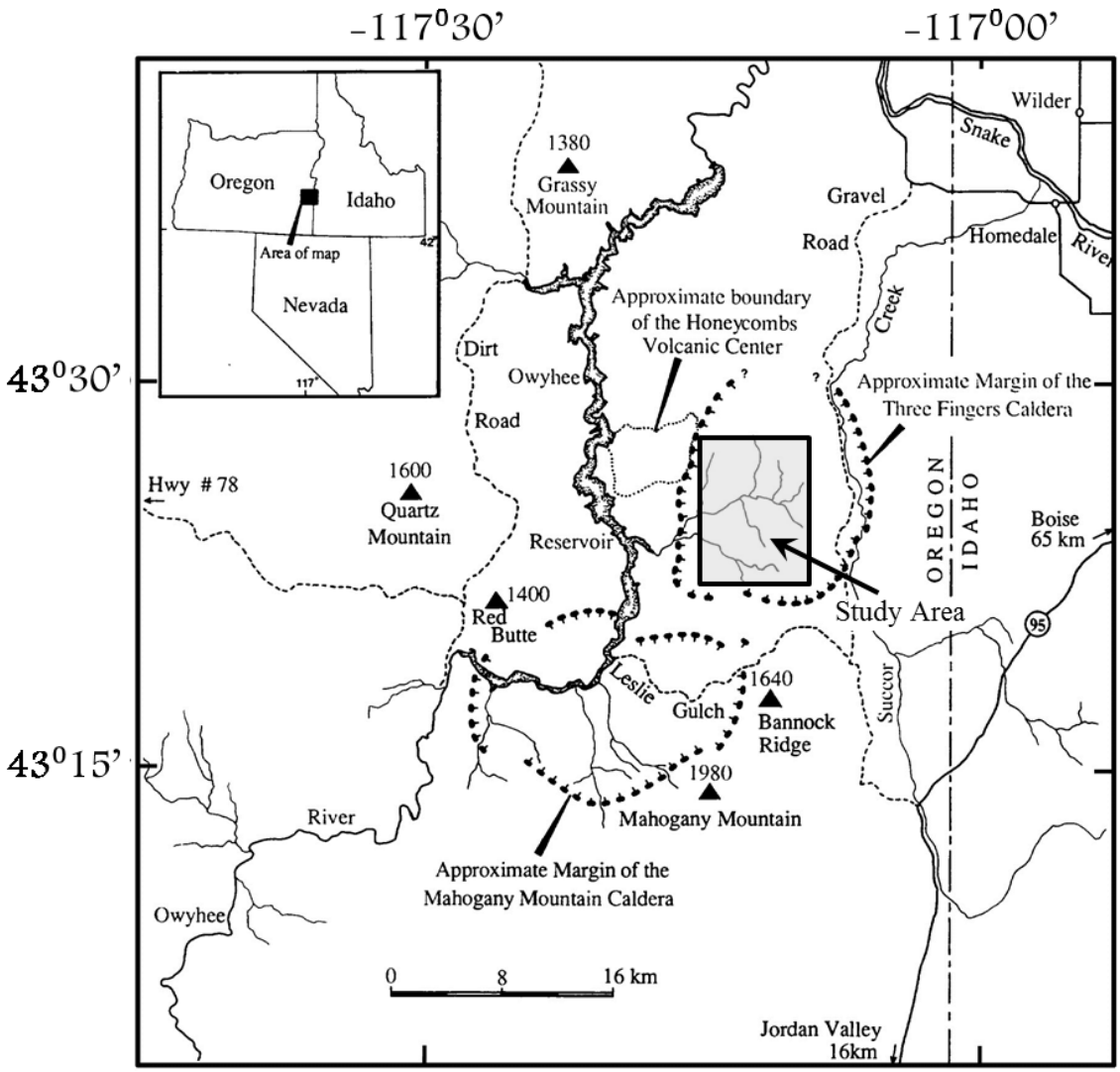

Figure 1. Map showing location of the study area within Three Fingers caldera. Also shown are Mahogany Mountain caldera to the SW and the Honeycombs volcanic center to the W-NW. These calderas occur near the eastern margin of the Oregon-Idaho graben. Modified from VanderMeulen (1989).

Chapter 1 – Geology of Three Fingers Caldera

1.1 - Background

1.1.1 - Regional Geology

The Oregon-Idaho graben is positioned at the western edge of the Snake River Plain, the eastern margin of the Oregon High Lava Plains, and the northern terminus of the Basin and Range provinces. This geographic and structural position is responsible for a diversity of magmatic products, from plume-related flood basalts to voluminous rhyolitic tuffs. Certainly, extension has played a role in the evolution of this landscape, as evidenced by the subsidence of the Oregon-Idaho graben and numerous north-south striking fault zones observed along an axis from SE Washington to NW Nevada.

Two competing hypotheses exist as to the cause of widespread voluminous middle-Miocene basaltic volcanism. The first cites the influence of a mantle plume beneath the North American plate, leading to weakening of the continental lithosphere (Camp, 1995). This idea is supported by continued development of high volume eruptive centers from the middle Miocene to the present across the Snake River Plain leading to a current position beneath Yellowstone. The second model involves back-arc spreading related to the subduction beneath the Cascade magmatic arc (Carlson and

Hart, 1987). This extension is proposed to have caused rifting along suture zones where terranes were accreted onto the North American craton. This is evidenced as widespread rifting and volcanism along an axis roughly parallel with the inferred cratonic margin and the Cascade magmatic arc (Leeman et al., 1992).

Voluminous regional volcanism during the middle Miocene began with the eruption of the Steens Basalt, at ~16.6 Ma (Hooper et al., 2002). Eruptions of plagioclase phyric basalts were followed by northward migration of eruptive loci, producing the Columbia River flood basalts. By 14 Ma, more than 97% of the total volume of flood basalts had been erupted in the region, and basaltic eruptions became more confined in a north-south trend along the continental craton. At the same time, a new trend emerged with magmatism expanding westward into the Oregon Plateau and eastward into the Snake River Plain of Idaho (Jordan et al. 2004). After this time, extensive basaltic volcanism ceased along the cratonic margin except within the Owyhee Plateau region.This region continued to experience many smaller-scale eruptions, including the Owyhee Basalt with upper flows dated at 13.4 Ma ± 0.3 (Watkins and Baksi, 1974), the Basalt of Succor Creek at 13.08 Ma ± 0.56 (Lees, 1994), and the Blackjack Basalt at 12.8 Ma ± 0.4 (Ferns and Cummings, 1996).

1.1.2 – The Oregon–Idaho Graben

The subsidence of the Oregon–Idaho graben was initiated following the most voluminous period of flood basalt eruptions, including the tholeiitic basalt of Malheur Gorge at 16.5 Ma ± 0.62 (Cummings et al., 2000), that is nearly contemporaneous with the onset of rhyolitic magmatism in the region. At ~16.7 Ma pulse of rhyolite volcanism is observed, beginning at the Santa Rosa–Calico and McDermitt volcanic fields to the south (Rytuba and McKee, 1984; Henry et al., 2006) and continuing northward to Dooley Mountain at ~14.7 Ma (Evans, 1992). Rhyolites of the Owyhee volcanic field were erupted along this axis between 15.5–15.2 Ma (Rytuba et al., 1991; Rytuba and Vander Meulen, 1991).

Regional NW–SE extension related to Basin and Range tectonism has been proposed to be a controlling factor in large silicic eruptions along the inferred suture zone with the cratonic margin to the east (Rytuba, 1989). The Owyhee Volcanic Field is situated near the northern terminus of the Basin and Range province, thought to be defined by the Brothers Fault zone to the west, and the Vale fault Zone to the north (Vander Meulen et al., 1989). Development of topography within the graben was largely controlled by development of horst and graben features related to Basin and

Range extension, beginning at ~15.3 Ma (Cummings et al., 2000). Minimum ages for regional extension are provided by late Miocene sedimentary successions and basalt flows overlying tuffs (Kittleman et al., 1967).

Cummings et al. (2000) indicate three main stages in the development of the Oregon-Idaho graben. Stratigraphic relations show that subsidence of the graben had begun before 15.2 Ma, with extension along north-south striking fault zones. Cross-cutting, N-S trending rhyolitic dykes within the Mahogany Mountain complex (Vander Meulen et al., 1989) suggest E-W extension continued after the formation of this caldera system. During this initial stage, large caldera-forming eruptions of rhyolitic ash-flow and air-fall tuff occurred on the eastern margin of the newly subsiding graben. Sediment inputs at this time were primarily from the east, off of the continental craton, as arkosic sandstones intermingled with locally derived tuffaceous siltstone and mudstone deposited along the axis of the graben, onlapping constructional highs formed by rhyolitic dome and pyroclastic eruptions.

The second stage of development is defined by continued extension along intra-graben fault zones, and the development of distinct sub-basins within the graben. During this period (14.3-12.6 Ma), smaller scale eruptions of calc-alkalic lavas

continued along N-S striking fault zones, suggesting their ascent may have utilized magmatic conduits established during large-scale silicic eruptions. Extensive hydrothermal activity began along these active fault structures with the incursion of meteoric waters. Numerous hot spring systems are evidenced by deposits of bedded sinter, chert, and hydrothermal eruption breccias (Cummings et al., 2000).

Volcanism continued through the third stage of graben development, with resulting aggradation of volcanic and sedimentary products exceeding the rate of subsidence. Low-lying sub-basins were filled in by lacustrine and fluvial sediments, and subsidence of the Oregon-Idaho graben ceased at ~10.5 Ma (Cummings et al. 2000).

1.1.3 - Calderas of the Lake Owyhee volcanic field

The Lake Owyhee volcanic field, as defined by Rytuba and others (1990), is comprised of at least five calderas: Mahogany Mountain caldera, Three Fingers Caldera, Castle Rock, Saddle Butte, and Star Peak. In addition to caldera eruptions, the rhyolite of Cottonwood Mountain erupted at ~15.2 Ma, after significant sedimentation within the graben, and the Littlefield Rhyolite erupted along N-S striking, synvolcanic fault structures in the Hog Creek fault zone (Cummings, et al., 2000). These eruptions took

place during the middle-Miocene and after emplacement of the Steens Basalt and contemporaneous basalt of Malheur Gorge.

Of these structures, only Mahogany Mountain and Three Fingers caldera have significant exposures of their internal stratigraphy (Ferns, 1997). Three Fingers caldera was first recognized by Rytuba and others (1989) in 1987, after the Mahogany Mountain caldera was discovered in 1984 by Rytuba and others (1985) during surveys by the U.S. Geological Survey. Although topographic expression of these calderas is faint, arcuate sections of thick ash-flow tuff deposits with corresponding gravity anomalies are interpreted as collapse structures (Vander Meulen et al., 1989; Rytuba et al., 1990). Both calderas are bounded to the east by the Devil's Gate Fault Zone, which continued to be an active magmatic and hydrothermal conduit throughout the later evolution of the Oregon-Idaho graben (Ferns, 1997; Cummings et al., 2000).

Mahogany Mountain caldera has a potassium argon date of 15.5 ± 0.5 Ma (Vander Meulen et al., 1987), and lies 5 km SW of Three Fingers caldera. Principal stages in the development of Mahogany Mountain caldera included eruption of pre-caldera lavas and caldera-forming voluminous ash-flow tuff, followed by eruption of post-caldera rhyolite dikes, domes, plugs, and flows (Vander Meulen et al., 1989). A

large central vent structure fed the eruption of volcanic domes within Mahogany Mountain through two N-S striking dikes, which have a potassium age date of 14.7 ± 0.4 Ma (Vander Meulen et al., 1987).

1.1.4 - Three Fingers Caldera

Three Fingers caldera was formed by explosive pyroclastic eruptions, resulting in collapse along ring fractures and vent structures (Ferns, 1997). This is evidenced in the Honeycomb Hills, a series of silicic vents that formed along the western flank of the caldera before collapse (Cummings et al., 2000) and are now topographic highs. The caldera-forming eruption produced the outflow tuff of Spring Creek, a metaluminous ash-flow tuff, and an intracaldera facies mapped by VanderMuelen et al. (1989). Rhyolite domes and flows erupted after collapse, along ring fractures and north-south striking faults within, and at the eastern margin of the caldera.

In many outcrops close to the center of the caldera, angular blocks of more mafic rock are entrained within both the presumed rhyolitic intracaldera tuff and the post-collapse rhyolite domes. This basal portion of intra-caldera tuff of Spring Creek was initially mapped as the "Basalt Bomb Member" by Vander Meulen et al., (1989), and contains clusters of mafic blocks up to 30 cm in length. These "bombs" are described as

spindle shaped, aphyric to slightly porphyritic rocks, containing xenocrysts of quartz and sanidine, often encapsulated by reaction rims of microcrystalline pyroxene and amphibole.

1.2 – Methods

1.2.1 – Field Mapping and Sampling

Field mapping was conducted to determine stratigraphic and aerial relationships between intra-caldera units and aerial extent of rhyolite lava flows erupted following caldera collapse. In particular, facies distributions of intra-caldera rhyolites associated with devitrified dome interiors (mapped as Trp by Vander Meulen et al., 1989) were noted, along with variations in dip angles of exposed bedding planes. Rhyolites were mapped and differentiated by lithological characteristics such as devitrification, porosity, and presence or absence of clastic debris. Attention was given to stratigraphic relations where possible to establish relative timing of their deposition. Clusters of entrained mafic clasts were assessed in terms of their relative abundance, distribution, and size range. Field descriptions of mafic clasts include: diameter, color, angularity, degree of weathering, and host lithology. Individual clasts were sampled from a variety of host facies to determine possible differences in mineralogy or geochemistry.

Samples of intra-caldera rhyolites were collected for geochemical analysis, representing the variety of facies and emplacement styles associated with these lavas. Final selection of 29 rhyolite samples to be analyzed at Washington State University was based upon encompassing a range of devitrification, porosity, and crystal content. In addition, two samples of glassy rhyolite were selected for $^{40}Ar/^{39}Ar$ analysis at Oregon State University, one from the intra-caldera rhyolites and one from the outflow tuff of Spring Creek. Other rocks included for geochemical analysis at WSU include nine mafic clasts, resistant tuffaceous sediments, volcaniclastic sandstone, and a pumice-bearing ash-flow tuff.

1.2.2 - Analysis Methods

Whole rock samples processed for geochemical analysis were composed of the freshest portions of the collected specimens. These portions were crushed into fine gravel size fragments of 2-4 mm using a jaw crusher, ensuring proper cleaning of the machine between samples to avoid contamination. Further processing for XRF and ICP-MS analysis was conducted in the GeoAnalytical laboratory at WSU, where samples were first ground into powder using a tungsten carbide swing mill, and homogenously mixed with dilithium tetraborate ($Li_2B_4O_7$) at a ratio of 1 to 2. Resulting mixtures were

then fused into glass beads in a muffle furnace, reground, and fused once again before analysis to ensure complete homogenization (Johnson et al., 1999).

Analysis of 10 major elements and 20 trace elements were performed using a ThermoARL Advant XP sequential X-ray fluorescence spectrometer. The X-ray intensity of each element within the final prepared glass beads is compared to the intensities measured in glass beads prepared from known standards with similar matrices. Trace element analyses of 14 REE and 13 additional trace elements were performed using an Agilent 4500 ICP-MS, after fluxing with dilithium tetraborate and further dissolution in a mixture of nitric acid, hydrofluoric acid, and hydrochloric acid in a closed Teflon vessel. After complete evaporation of the resultant solutions, additional nitric and hydrofluoric acids were added, as well as hydrogen peroxide before final dilution with de-ionized water.

Fresh samples selected for determination of age dates were composed of dense, black glassy groundmass, containing abundant phenocrysts of alkali feldspar and quartz. Rocks were crushed to fine chips by use of a jaw crusher and sieved into three size fractions: 1) less than 300 μm, 2) 300-900 μm, 3) 900-2000 μm. Alkali feldspar phenocrysts were picked from the resultant fragments under a binocular microscope

and set aside for analysis by $^{40}Ar/^{39}Ar$ method in the geochronology lab at OSU. Final preparation for analysis involves a mild acid cleaning using HNO_3 to remove carbonates and minor alteration of mineral grains, in addition to a 5 minute wash in a 5% hydrofluoric acid solution.

Determination of absolute age using the $^{40}Ar/^{39}Ar$ method requires irradiation to generate the isotope ^{39}Ar, and comparing it to natural decay product ^{40}Ar. This method is advantageous to K/Ar dating in that measured products all come from the same aliquot. Measurement of isotopes requires incremental heating of minerals to release stored Ar in a stepwise fashion. This produces a spectrum of dates related to the thermal history of the rock, and agreement between ratios of $^{40}Ar/^{39}Ar$ across successive stages is used to constrain the final age date.

1.3 – Results

1.3.1 – Lithology of units from Three Fingers caldera

Preserved stratigraphy within Three Fingers caldera displays three major periods of development. The oldest exposures within the study area are a sequence of tuffaceous sediments likely derived from loosely consolidated material within the basin. The remnants of later erupted intra-caldera rhyolite lavas are generally distributed along

N-S striking ridges, in agreement with the orientation of exposed dikes and devitrified plug features. Rhyolite lava flows erupted through these conduits occur above tuffaceous sediments, but are also overlain by a second succession of fine-grained tuffaceous sediments. Silicification is observed within all lithologies, but is most common amongst more porous rocks. Mafic clasts recognized by Vander Meulen et al. (1989) occur primarily near the base of intra-caldera rhyolite flows, often alongside clasts of underlying tuffaceous sedimentary rocks.

1.3.1.1 - Intra-caldera Rhyolite

Effusively erupted rhyolites erupted after caldera collapse are divided into four facies based on lithology: i) dense glassy rhyolite and associated breccias; ii) porous glassy rhyolite; iii) dense devitrified rhyolite; iv) porous devitrified rhyolite. All four facies have similar mineralogy and geochemistry, but display a wide range of textures, from pumiceous to dense black glass with a perlitic texture. Exposures of dense intra-caldera rhyolite display alternating bands at transitions between glassy and devitrified facies and gradational contacts (Figure 2) indicating that these are the same units and not separate flows. Porous intra-caldera rhyolites rarely show a clear boundary

between glassy and devitrified facies, displaying gradational contacts with a variable fraction of glassy groundmass material.

1.3.1.1a – Intra-caldera rhyolite – dense devitrified facies

Dense devitrified rhyolite flows make up the majority of the high standing features within the study area due to their relatively resistant nature. Outcrops often show vertical to steeply dipping flow banding, aligned with gradational transition zones to dense glassy rhyolite, as can be found near the base of Three Fingers Rock. In these cases, exfoliation produces long, trailing talus slopes composed of platy, jointed rhyolite ranging from 20 to 50 cm in diameter that generally fill small gullies. In large part, these outcrops are distributed in parallel ridges running primarily N-S throughout the study area, concordant with orientation of normal faults.

Lava flows of dense devitrified rhyolite also outcrop in low angle orientations, illustrated by visible flow bands of more and less devitrified material (Figure 2). In some cases, vesicles are stretched to indicate direction of travel from the vent, but phenocrysts typically maintain random orientations within these rocks. Examples of low angle contact relationships with dense glass are preserved near the top of N-S striking ridges, with resistant dense devitrified material capping the less resistant dense glassy margin.

No mafic clasts could be clearly identified within the rhyolite of the dense devitrified facies.

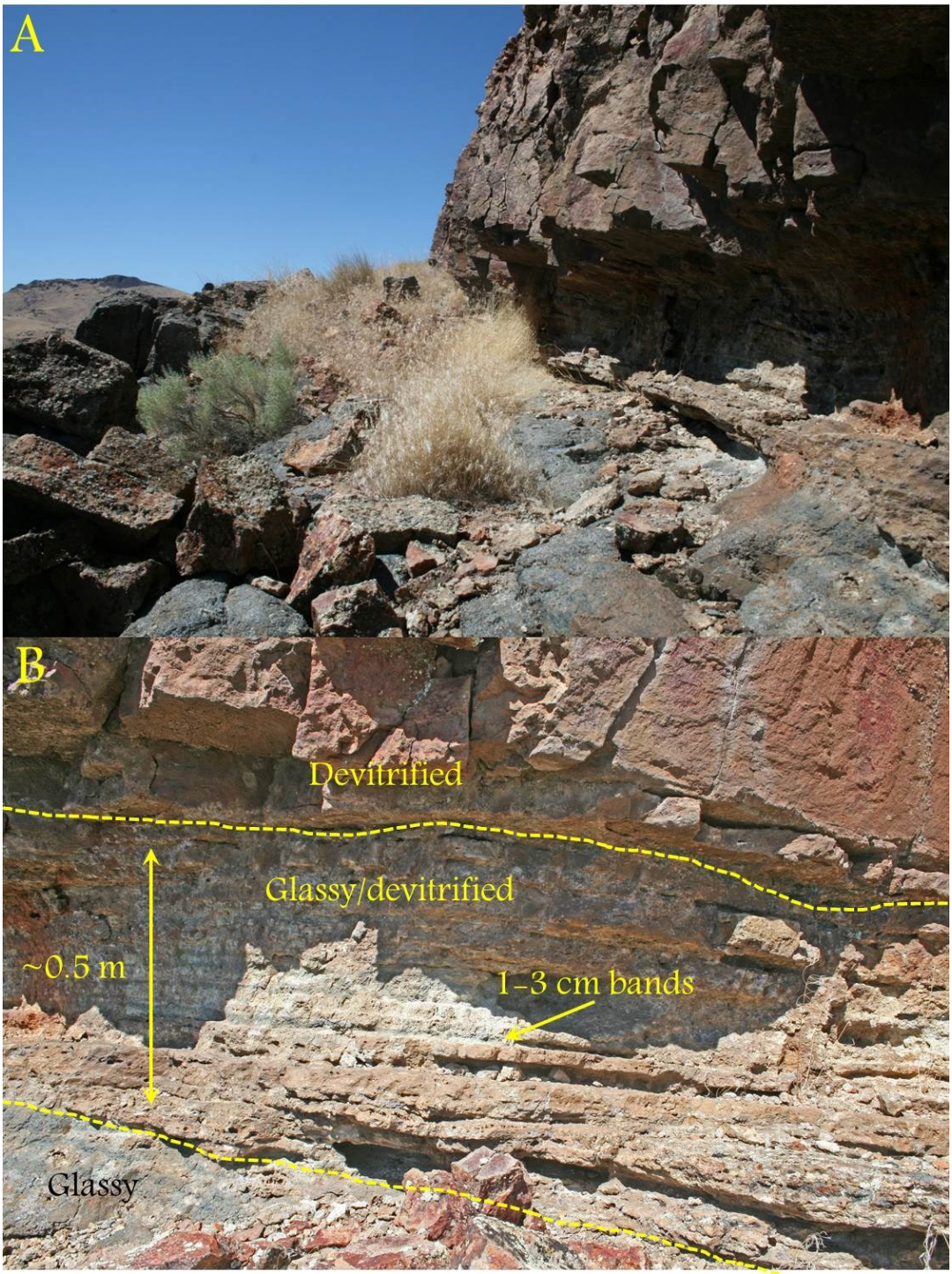

Figure 2: Dense devitrified rhyolite in contact with dense black rhyolite glass. Crude columnar jointing occurs in the upper devitrified zone (A), which shows much greater resistance to weathering. A sharp transition occurs between rock that is devitrified, and rock that is largely glassy, (B) shows varying degrees of devitrification within alternating bands, typically on the order of ~1-3cm. Below this contact zone is massive dense glassy rhyolite.

1.3.1.1b – Intra-caldera rhyolite – porous devitrified facies

Rhyolite of the porous devitrified facies rarely forms topographic highs, but is the most widespread facies of exposed intra-caldera rhyolites within the study area. Resistance to weathering within this facies varies greatly, often creating chaotic, craggy, or skeletal outcrops interspersed with very friable material of the same origin. At the contact between this facies and low angle glassy rhyolite sheets, more resistant exposures may appear as a rind or crust overlying dense glass. These resistant outcrops of porous devitrified material often form short (1-3 meter) weathered columns and low ridges. These outcrops appear bright white where fresh, but color is largely dependent on degree of weathering (yellow to brown), hydrothermal alteration (green), and presence of fractured but intact glass beads (grey). This facies is the most common host for mafic clasts, which are often found protruding from more weathered host rhyolite.

1.3.1.1c – Intra-caldera rhyolite – dense glassy facies

Exposures of dense glassy rhyolite vary considerably from isolated blocks of a few meters lodged in more porous material, to expansive sheets covering the land surface. Gradations in vesicularity of glass from one outcrop to another vary and alter the appearance dramatically, from deep black to medium gray, with altered glass

commonly brown at the surface, or green along silicified fractures. Variable amounts of course sand-size black glass fragments grade into porous glass facies at gradational contacts. Many times gradational contacts are accompanied by zones of glassy 'pseudo-breccias', called so because the original position of volcanic glass is maintained, while appearing to have been cut through by fluids or gases under extreme pressure. These breccias display a wide range of textural variation, from outcrops showing few large veins to those profusely altered by a threadlike network of sub-millimeter devitrified veinlet structures. These facies relationships are best exposed near the eastern end of Three Fingers Gulch as a series of steep cliffs composed entirely of rhyolitic glass.

Dense, glassy margins in contact with dense devitrified rhyolite are often banded, with alternating layers of glass showing variable porosity. Such outcrops occur at the base of Three Fingers Rock and in numerous other places, clearly marking the transition from glassy to entirely devitrified, with alternating parallel bands from <1 cm to 3 cm in width in a high angle orientation. This outcrop measures 2 to 3 meters in overall width from the devitrified core, where it terminates in the dense glassy facies. Outcrops of banded dense glass are also exposed beneath flows of dense devitrified rhyolite, with measured thicknesses of up to 3 meters (Figure 3A), observed primarily

near the top of ridges and isolated peaks where dense devitrified rhyolites form a resistant cap. Some examples of dense glassy rhyolite show a similar banding, with dips ranging from near horizontal to greater than 30 degrees, but with no observed contact with dense devitrified facies (Figure 3B). In this example, flow banded glass appears to cross cut crudely formed columns of similar glassy material, likely exposed due to erosion of overlying units.

Figure 3: Dense glassy rhyolite exposed beneath dense devitrified facies (A) forms exposures of up to 3 meters in height. Lithology of dense glass facies can vary considerably within a single outcrop (B), from finely laminated flow banded glassy rhyolite (upper left), that here appears to emerge from crude columns of dense glassy rhyolite (lower right).

1.3.1.1d – Intra-caldera rhyolite – porous glass facies

The least common facies of intra-caldera rhyolite shares common mineralogy with other facies, but is lighter in color and more friable than dense glassy rhyolite. Outcrops of porous glass are variable shades of medium to light grey and often appear to grade into porous devitrified rhyolite. This facies is also a common host rock to mafic clasts, but general lack of exposures limits observations of their abundance. Observed thickness of porous glass outcrops is no more than 2 meters, and its appearance is generally associated with either a transition between dense glass and porous devitrified rhyolite, or as entrained clasts within glassy autobreccias. Hand lens observations of these transitions reveal changes in color directly relate to the proportion of sub-millimeter black glass fragments.

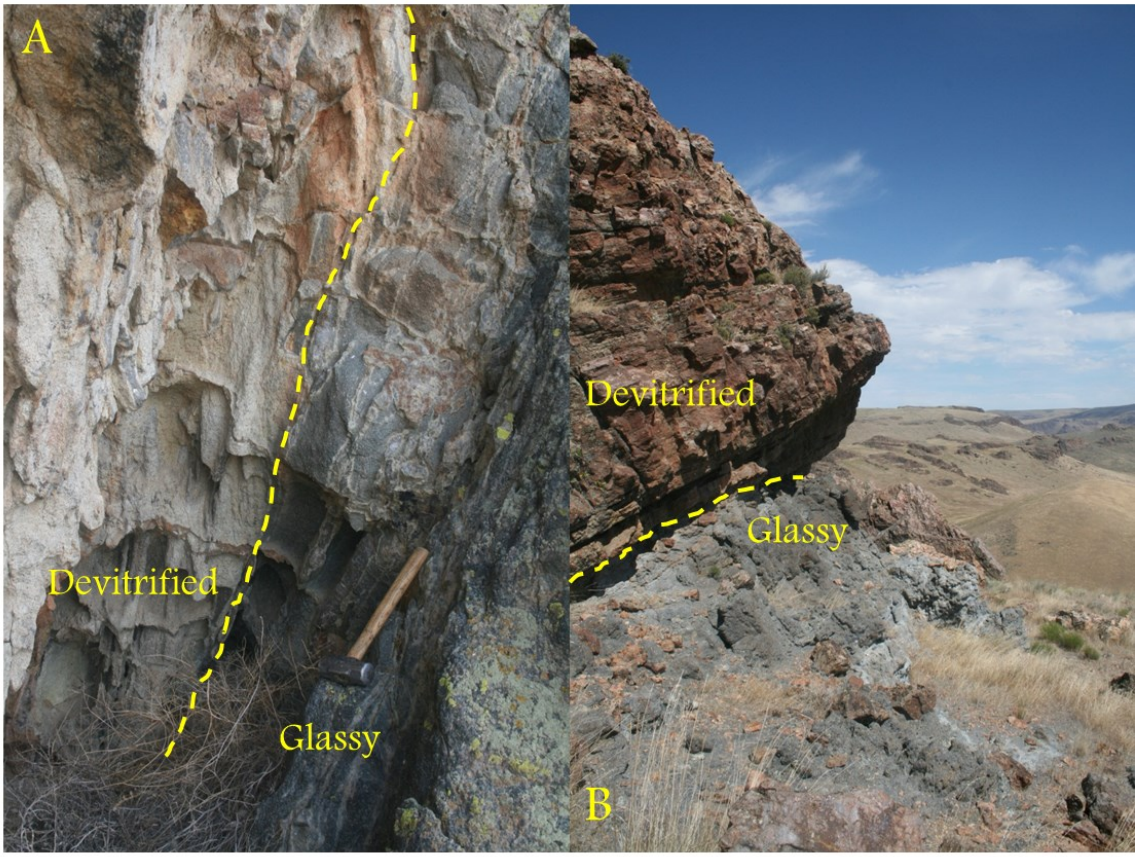

Figure 4: Two types of transitions between dense glassy rhyolite and devitrified facies. (A) shows a gradual transition from dense glassy rhyolite (right), to porous devitrified rhyolite, with increasing abundance of devitrified veinlets near the contact resulting in a transition through the porous glassy facies. (B) shows an abrupt transition between dense glassy rhyolite (bottom) overlain by banded dense devitrified lava.

1.3.1.2 – Glassy rhyolite autobreccia and pseudo-breccia

Rhyolite breccias are composed of variable proportions of dense black glass, porous glass, and nearly white fractured matrix glass. Most often, these appear as matrix-supported breccias, with subrounded to subangular blocks of <5 to 30 cm in diameter, with some blocks reaching up to 1m in diameter (Figure 5A). Blocks are primarily composed of dense black glass and porous glassy rhyolite, but also present in

minor amounts are angular clasts of very resistant, altered green glass (Figure 5B) and 1-5 cm angular mafic clasts making up less than 5% of the rock. Dense and revesiculated glass clasts appear to maintain their primary texture, indicated by uninterrupted parallel banding in some dense glass blocks showing original flow foliation.

Some outcrops bearing a similar appearance to glassy rhyolite autobreccia display textural evidence suggesting they are not truly breccias. Consistent banding across features of varying porosity (Figure 6B) indicate 'pseudo-breccias' are due to secondary processes acting upon a cohesive deposit in place. In select cases, outcrops of pseudo-breccias grade downward into dense black glass that is cross-cut by devitrified veinlets, creating a puzzle-like fit between 'clasts' (Figure 6A). Exposures of cross-cut glassy rhyolite vary between those where devitrified, light-colored veins occupy only 5-10% of the rock to those where the proportion dense black glass is less than 10%, and can be easily mistaken for a matrix supported autobreccia.

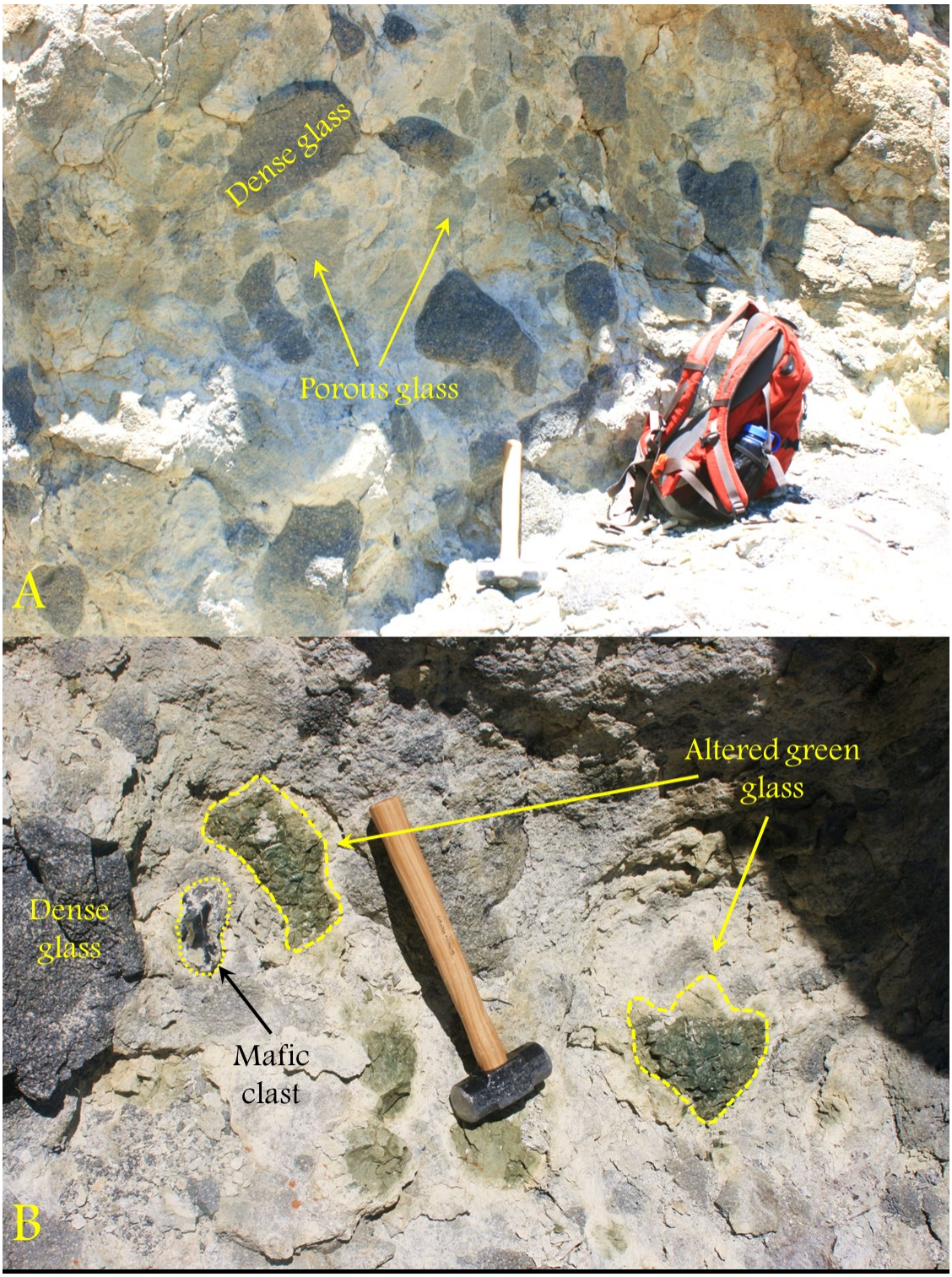

Figure 5: Monomict rhyolitic breccia, including clasts of dense and porous glass (A) is supported in a porous matrix with similar mineralogy. Near the base of glassy breccias, mafic clasts and altered green glass are observed (B). Alteration is also observed in a zones of host rock near the head of the hammer, lacking a clearly defined margin.

Deposits of glassy autobreccia are typically massive in lithology, while 'pseudo-breccias' commonly show formation of resistant fins and ledges at high angles (70-90 degrees) to the land surface (Figure 7B). In many cases, devitrified material is less resistant than the dense glassy parent rock, resulting in successions of fins and knobs of dense glass that shows little alteration. In fewer cases, devitrified material is more resistant than the dense glassy rhyolite, and erosion of glass leads to a honeycomb-like texture in weathered outcrops. True breccias are also overlain by continuous sheets of dense black glass, while 'pseudo-breccias' many times grade upward into porous devitrified rhyolite. The change in appearance upsection is due to the proliferation of fine veinlets that are typically larger and fewer in number downsection.

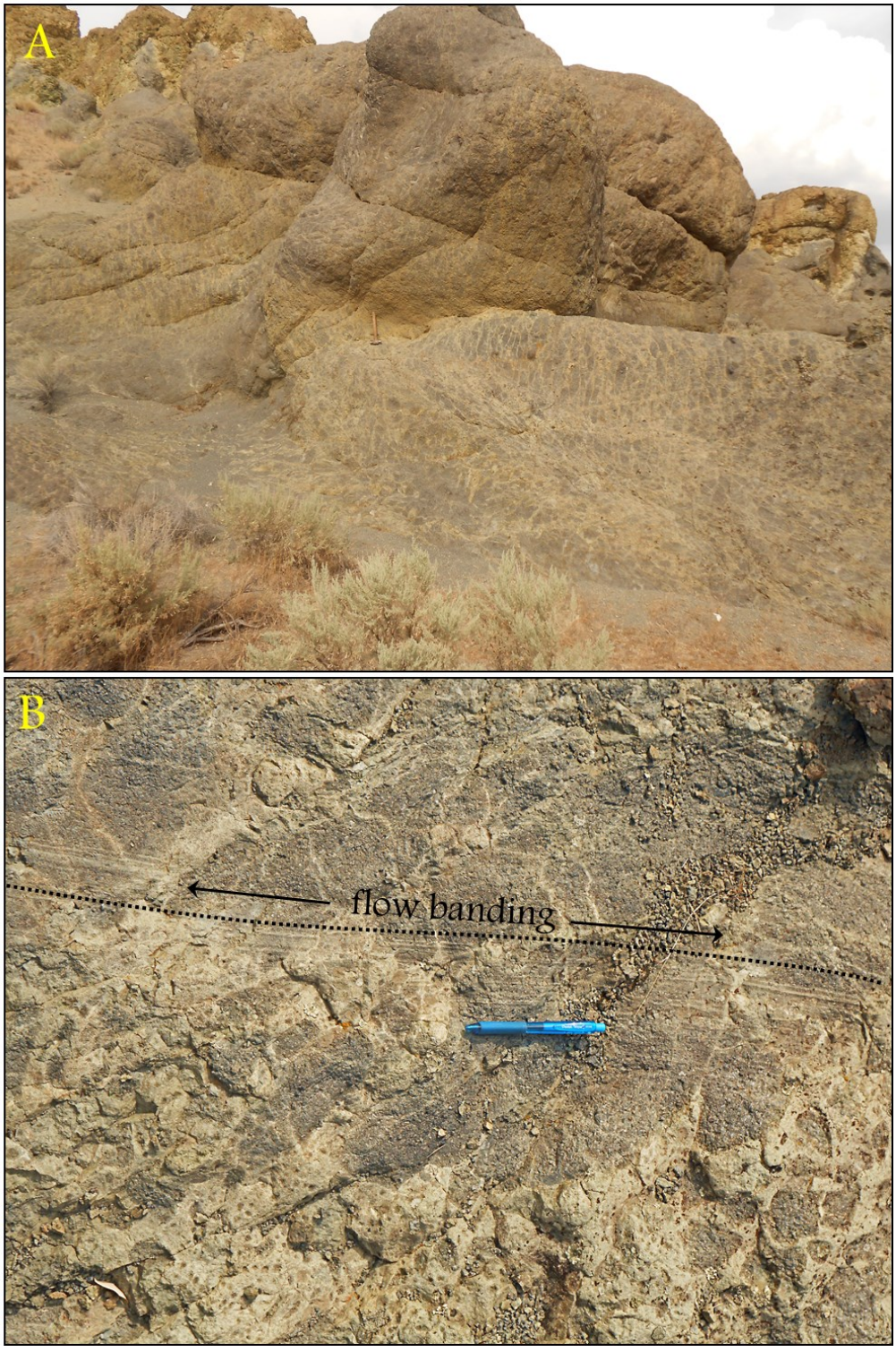

Figure 6: The puzzle-like appearance displayed in outcrops of glassy 'pseudo-breccia' is caused by fine veinlets of devitrified glassy rhyolite (A). The proportion of devitrified material increases upsection as veinlets become more dispersed. Flow banding common to dense glass and devitrified matrix indicate these do not represent true breccias (B).

Figure 7: Pseudo-breccias of intra-caldera rhyolite showing dense glass within a fractured devitrified matrix (A). Dense blocks are typically angular, and range from 2-20 cm (chisel is ~15 cm). Rhyolite pseudo-breccias are typically exposed in steep sided canyons, with finely intruded deposits often interspersed with thicker veins of devitrification (B).

1.3.1.4 – Pumice-bearing ash-flow tuff

Ash-flow tuffs exposed within the caldera are typically light green to tan, measuring up to 10 meters in thickness, and commonly contain oblate, sub-rounded lapilli-sized pumice between 5 and 10 mm. Pumices vary in appearance, from darker green in light green samples, to tan or yellow in lighter colored samples, and are often quite friable relative to ashy matrix. Outcrops are typically welded and display void spaces from 10 to 50 cm in diameter as distinct weathering features, generally oblong

in shape with long axes parallel to the ground surface. Ash-flow tuffs are most commonly exposed beneath tuffaceous sediments either in deeply incised stream valleys or near the base of uplifted fault blocks, and represent the earliest deposited post-collapse unit exposed within Three Fingers caldera. Ash-flow tuff is also observed directly beneath porous rhyolite and in contact with dense, devitrified rhyolite, and dense glassy rhyolite, but these instances are rare.

1.3.1.5 - Tuffaceous sediments

The majority of outcrops of tuffaceous sediments are composed of fine particles, deposited in parallel bedding planes of 0.5 to 10 cm in thickness. Few laminations of sand-size particles are observed these exposures, and are typically only 1-2 mm in thickness, with the majority of laminations composed of fine ashy material. Bedding is largely obscured in more resistant, silicified deposits, which appear massive in texture. Tuffaceous sediments appear beneath polymict breccia of volcaniclastic debris that often include angular clasts of this unit and angular mafic clasts, referred to as 'basalt bombs' by Vander Meulen et al., (1989). Dip angles range up to 30^0, and are often oriented away from N-S striking ridges where intracaldera rhyolites have emerged during possible dome eruptions. Exposures range from less than 1 meter to greater than

20 meters in thickness, with more resistant outcrops producing vertical cliff faces (Figure 8A).

Groundmass in fine sediments can vary between powdery, lightweight, and friable in weathered samples to waxy, dense, and very resistant in silicified rocks. Weathered outcrops with a powdery texture tend to reach no more than 2 meters in thickness and white to tan in color, while silicified siltstone can reach as high as 20 meters, appearing white and pink, with some outcrops deep green in color and extremely resistant. Some cases exist where more friable outcrops are preserved by a capping veneer of resistant porous rhyolite, often containing inclusions of this unit and less commonly angular mafic clasts. The base of this unit is exposed in the western part of Three Fingers Gulch, where it overlies coarser sediments near the bottom of the valley.

Parallel bedded tuffaceous sandstone is largely composed of 0.25–0.5 mm grains in a matrix of finer tuffaceous debris. The lower 5–7 meters of sandstone exposures are laminated, and grade upward into massive deposits with total thickness reaching 18–20 meters. Cross-bedding is rare and limited to a zone about 2 meters above the base of the exposure in Three Fingers Gulch. Laminations of finer material near the base contain

plant fossils, and indicate these sediments were deposited in a low-energy environment. Tuffaceous sandstone is often weathered to an orange-brown color (Figure 8B), but can also be white, containing accretionary lapilli of less than 0.5 cm, subrounded mineral grains, and a greater proportion of fine sediment.

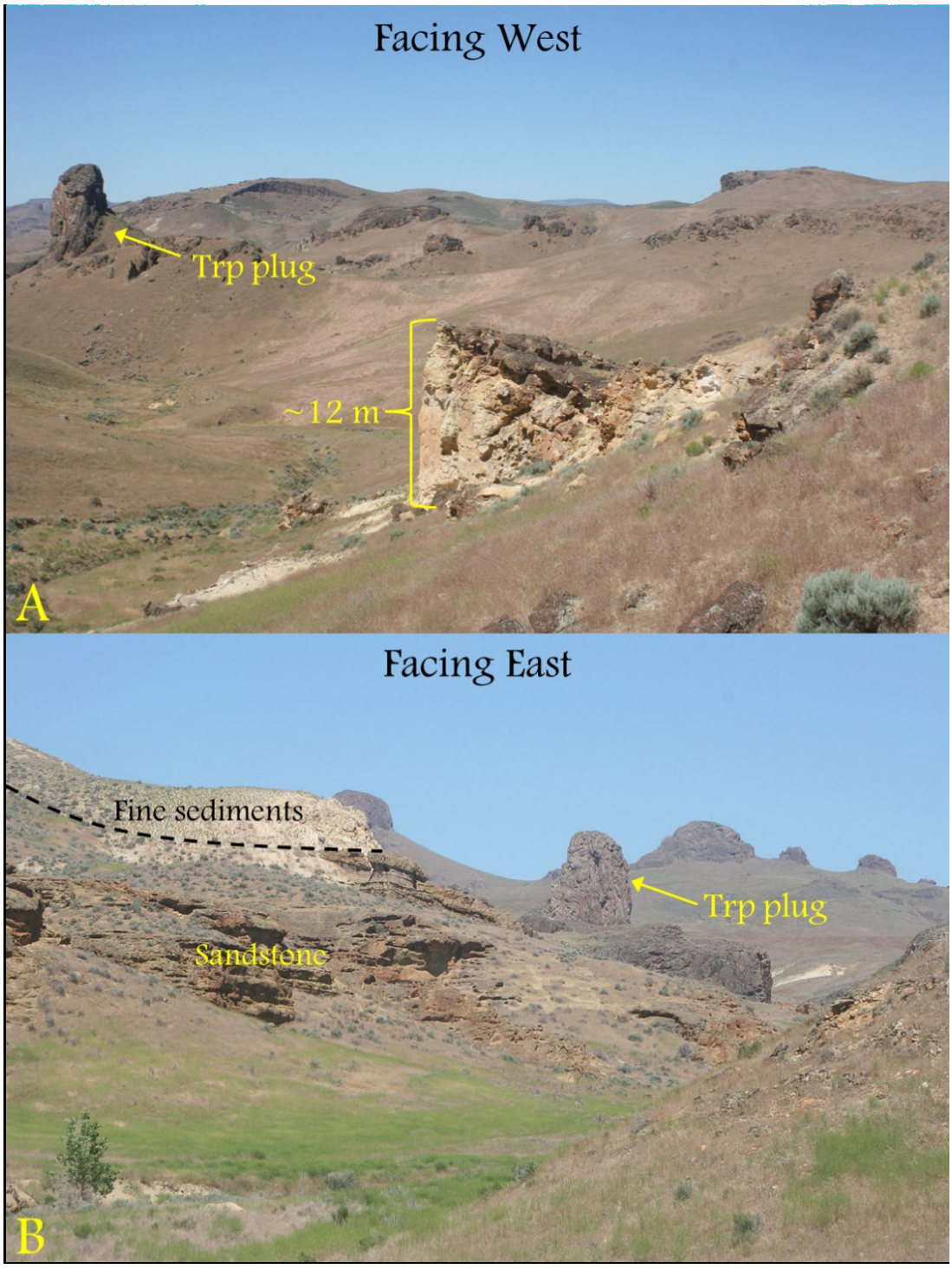

Figure 8: Tuffaceous siltstone exposed in two locations near a steep sided plug of devitrified rhyolite (Trp). Steep sided cliffs are common where sediments have been extensively silicified (A). These outcrops often show high angle dips, either affected by post-emplacement faulting or uplift by growth of cryptodomes. The base of these fine sediments is rarely exposed, but is seen here overlying coarser volcaniclastic sandstone deposits (B).

1.3.1.6 – Matrix supported polymict rhyolite breccia

Most often exposed at the base of porous devitrified rhyolite facies, this unit is defined by an abundance of clastic debris entrained within a crystal-rich host rock. Underlying lithology varies by location, which largely determines the nature of entrained clasts. The most predominant inclusions are angular blocks of aphyric, silicified tuffaceous siltstone, often along with somewhat less abundant angular mafic clasts (Figure 9B). Less commonly, crystal-poor, pumiceous clasts are entrained and typically have undergone extensive weathering, with lapilli-size pumices dark yellow and very friable where not completely eroded out of their host rocks.

Typically, polymict breccias form a thin drape over the land surface of less than 2 meters (Figure 9A), but sometimes form resistant ledges that outcrop in linear arrays across eroded stream canyons.

Figure 9: Quarry location reveals contact relationship between tuffaceous siltstone and overlying porous devitrified rhyolite flow, with a 4-6 foot zone of polymict breccias existing between these units (A). Breccias are composed primarily of porous devitrified rhyolite, and variably contain siltstone and dark colored lithic fragments (B).

1.3.1.7 – Mafic clasts

The mafic inclusions distinguishing the 'basalt bomb member' of Vander Meulen et al. (1989) typically occur near the base of intra-caldera rhyolite deposits, and can vary in distribution from less than 1% to over 15% of the total volume of rock in a given outcrop. These mafic clasts range in size from 3 to 30 cm in diameter, but most examples are from 5 to 10 cm, and are typically sub-angular to angular. These

clasts exhibit sharp contact with the surrounding rhyolite, and in many cases have developed a weathering rind that can vary from dark yellow to dark red, staining the host rock where significant weathering has taken place. Mafic clasts are observed in all but the dense devitrified facies of intra-caldera rhyolite where they may have been obliterated by the devitrification process, and are most commonly observed in the lower 5 meters of porous devitrified rhyolite deposits.

Depending on setting, mafic clasts can appear nearly black with a smooth texture, to medium gray with a fine gritty texture. Lighter colored clasts are often friable and can be broken by hand while darker colored samples can be difficult to fracture with a hammer. Sub-parallel, wavy flow banding is frequently observed in these rocks, producing angular or tabular blocks, but many samples have no such foliation, and produce largely sub-angular to sub-rounded clasts. Flow banding becomes more apparent with higher degrees of weathering, resulting in planes of weakness.

The presence of mafic clasts is often accompanied by the occurrence of 10-50 cm blocks of platy tan to white tuffaceous siltstone. The texture of these accidentals is

typically waxy to powdery, depending on degree of silicification, and correspond to the lithology of fine grained tuffaceous sediments within the caldera.

1.3.2 – Petrography of units within Three Fingers Caldera

1.3.2.1 – Intra-caldera rhyolite

Thin section analysis of intra-caldera rhyolites shows variable phenocryst content, typically ranging from 12 to 25%, with a few crystal-rich examples (up to 30%) found near the base of exposures. Crystal-rich deposits primarily vary in the abundance of large (6-10 mm) alkali feldspar crystals, while abundances of 2-4 mm feldspar and 1-2 mm quartz remain largely unchanged upsection. Larger feldspars are euhedral and blocky, often nearly square, and make up as much as 50% of all phenocrysts in crystal-rich samples. Smaller, euhedral feldspars typically range from 2-4 mm in length and 1-2 mm in width. Quartz phenocrysts vary in diameter from 0.5-2.0 mm, and are anhedral, generally comprising no more than 25% of modal abundance. Also present as a minor phase is dark green clinopyroxene, forming narrow sub-millimeter phenocrysts, often as intergrowths with alkali feldspar.

1.3.2.2 – Dense glassy intra-caldera rhyolite

Samples of dense glassy rhyolite exhibit hyaloophitic texture with a perlitic, glassy groundmass (Figure 10). Small fractures likely created by expansion of glass as a result of hydration often show the growth of microlites, giving the rock a grayer appearance in hand sample. Lighter colored rhyolite glasses display a higher number of fractures. The darkest versions of these rocks have little to no perlitic fractures, few threadlike fractures, and lack the growth of microlites.

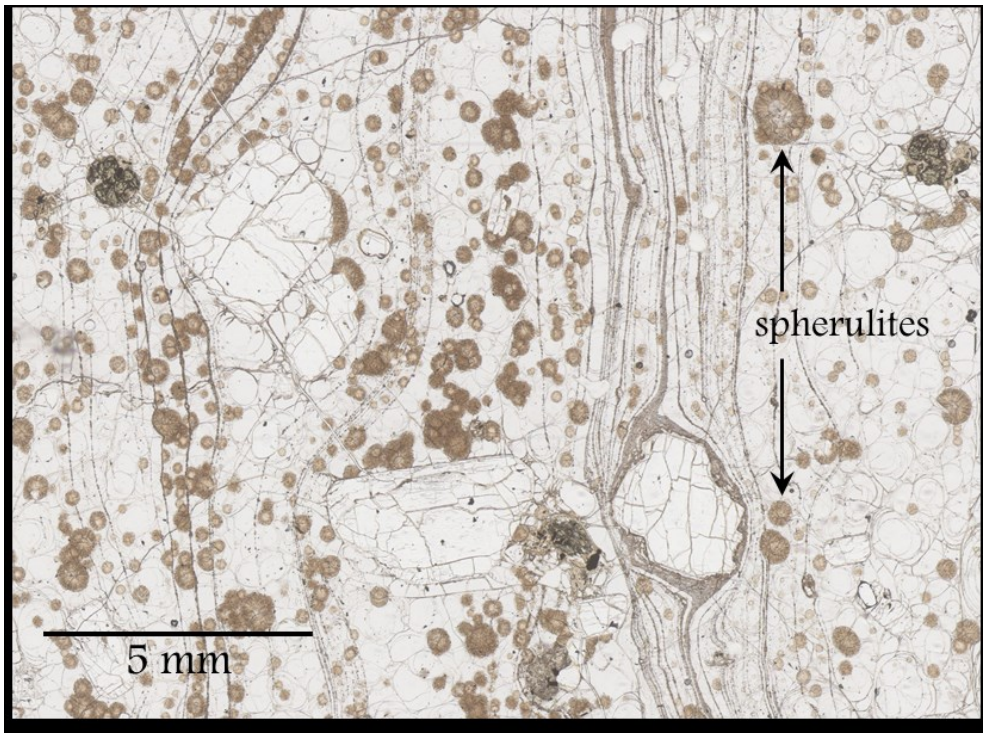

Figure 10: Dense glassy intra-caldera rhyolite with hyaloophitic texture is often finely banded at the margins of devitrified rhyolite plugs. The pattern of parallel bands is often distorted around larger phenocrysts of alkali feldspar. This sample (TF-295) also shows minor devitrification in the form of spherulite growth.

1.3.2.3 – Dense devitrified rhyolite

The dense rhyolite forming high standing ridges, plugs, and flows is spherulitic in texture with complete replacement of glass by the growth of spherulites (Figure 11). The devitrified groundmass contrasts with transparent, subhedral alkali feldspar and irregularly shaped small open spaces that make up 5–7% of the volume of the rock. Large 8 mm alkali feldspar are rarely observed in this facies of intra-caldera rhyolite.

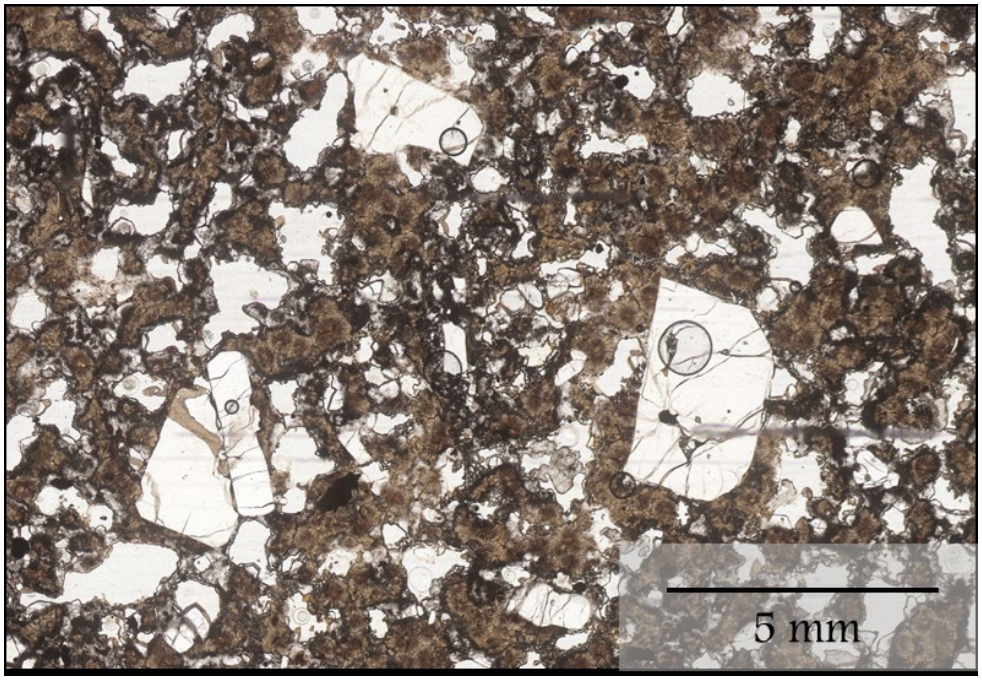

Figure 11: Dense devitrified rhyolite exhibits extensive spherulite formation, rendering the groundmass less transparent than in glassy rhyolites. Large alkali feldspar phenocrysts are often fractured and subhedral, clearly contrasting with the darker groundmass.

1.3.2.4 – Porous devitrified rhyolite

Porous intra-caldera rhyolites are finely vesiculated, with a hyaloophitic texture of transparent crystals in a translucent, devitrified groundmass (Figure 12). Vesicles are typically 0.1 mm or less and range from spherical to oblate in some samples to stretched and tube-like in others. Small scale (<5 mm) regions of deformation and alignment of vesicles often exist, randomly oriented with respect to one another. These are typically enclosed by porous glass showing stretched vesicles sub-parallel to one another, suggesting these rhyolites were in motion as they cooled. Phenocrysts are generally euhedral, and are often concentrated along flow foliations that bend to accommodate

larger alkali feldspar phenocrysts. In these cases, vesicles are stretched and asymmetric, showing rotation of these grains during flow. Growth of microcrystals is ubiquitous along the vesicle walls in porous devitrified rhyolites.

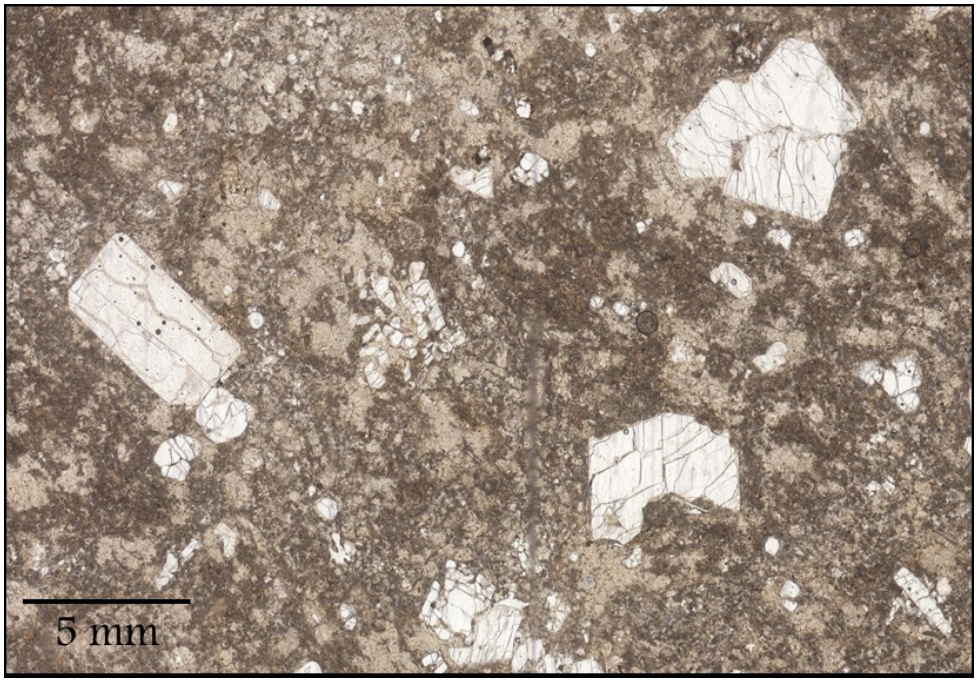

Figure 12: Porous devitrified rhyolite also contains large alkali feldspar phenocrysts, and a finely vesiculated groundmass texture.

1.3.2.5 – Sparsely phyric basalt

Mafic lava flows display hypidiomorphic granular texture, with subhedral plagioclase typically less than 1 mm composing less than 2% of the rock, and minor proportions of olivine, clinopyroxene, and orthopyroxene (Figure 13). Many larger specimens of plagioclase (~1 mm) appear partially resorbed with a spongy texture, suggesting these were not in equilibrium within the magma before eruption.

Groundmass is made up of fibrous plagioclase, oxide minerals, and glass, with very small (less than 0.1 mm) olivine visible under crossed polars. Many plagioclase laths show preferred orientation, suggesting trachytic texture induced during flowage, which is not surprising as formation of well-defined columns suggests this was likely a valley fill flow.

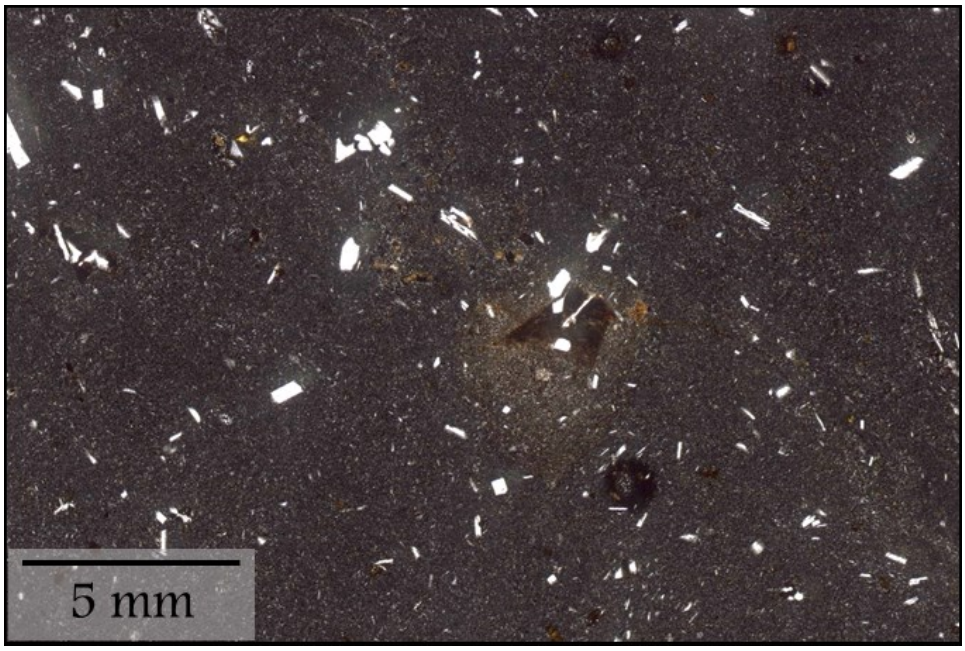

Figure 13: Sparsely phyric basalt flow sample TF-330 contains less than 2% plagioclase phenocrysts, with minor pyroxene, olivine, and amphibole. Groundmass texture is extremely fine, composed of 50-60% plagioclase, 20% oxides, and interstitial glass.

1.3.2.6 - Pumice-bearing ash-flow tuff

Overall texture is vitroclastic, with fractured phenocrysts distributed within a groundmass of distorted, devitrified glass shards. Phenocrysts include 5-10% alkali feldspar of 2-3 mm, 5% plagioclase of 1-2 mm and minor proportions of pyroxene and

anhedral fayalite, typically less than 1 mm. This unit often contains less than 1% sub-millimeter size lithic fragments, ranging from deep red to brown. Lapilli-size pumice of 0.5-1.0 cm are rounded to slightly oblate in shape, and vesicles are stretched where visible. Replacement of glass by devitrification often obscures their primary texture.

1.3.2.7 – Tuffaceous sedimentary rocks

Two distinct types of sedimentary rocks appear within Three Fingers Caldera, distinguished by the abundance of sand-size crystalline particles. Most commonly, tuffaceous sedimentary rocks are nearly free of visible crystals, composed nearly entirely of silt to clay sized particles of volcanic ash, with only occasional bands containing minor proportions of rounded feldspar and quartz grains. The second type is poorly sorted, with 25-30% rounded to subrounded mineral grains in a matrix composed of fine glass fragments and quartz. Mineral grains are typically 0.5 to 1.0 mm in a poorly sorted, ungraded arrangement (Figure 14), composed of ~80% feldspar and 20% quartz. Also present are 3-5% rounded pumices (< 1 mm), and 1-2% dark lithic fragments (< 0.5 mm). The textural difference between these rocks suggest that while water may have been involved with their formation, the more crystal-rich portion likely represents a mudflow or lahar deposit derived from non-welded tuff.. The

abundance of anhedral phenocrysts combined with a lack of sorting indicate that these materials traveled only a short distance from their source.

Figure 14: Sample TF-407 is composed of rounded crystals and minor lithic fragments in a matrix of finer tuffaceous material. The dark streak through the center of the frame represents banding observed in hand specimen.

1.3.3 – Geochemistry of units within Three Fingers Caldera

Samples collected from within Three Fingers caldera for this study are compared to units from nearby Mahogany Mountain caldera, three samples of tuff of Leslie Gulch and two from rhyolitic dikes emplaced within the core of the Mahogany Mountain Caldera complex. Samples collected from both younger and older McIntyre Ridge rhyolite flows are also compared, erupted on the eastern margin of Three Fingers caldera, vitrophyres from Spring Creek outflow tuff, and the regionally extensive 10.6 ±

0.3 Ma (Rytuba et al. 1991) Jump Creek Rhyolite of Kittleman et al. (1965, 1967). Also included is one sample from the 13.5 ± 3.5 Ma (Ferns and Cummings, 1992) Dam Rhyolite, so named for its emplacement abutting the dam of nearby Owyhee Reservoir. Distinctions between eruptive units were guided by the use of trace element and REE diagrams, leading to comparison of sets of elements in variation diagrams, including Total Alkali versus Silica (TAS), index of peralkalinity, and graphical representation of the europium anomaly (Eu/Eu*).

The europium anomaly was calculated for each sample using the following (all normalized to C1 chondrite values):

$$Eu/Eu^* = Eu/\sqrt{Sm \times Gd}$$

1.3.3.1 – Major elements

Classification of samples using total alkali versus silica (Figure 15) shows the tuff of Spring Creek averaging slightly higher alkali content than intra-caldera rhyolite, with widest variations observed in intra-caldera glass. Devitrified intra-caldera rhyolites are overall highest in silica and lowest in Al and alkali content of rhyolites within the Three Fingers-Mahogany Mountain area, with these features are likely the product of alteration. Aphyric lava flow sample TF-330 plots just within the field of

basaltic andesite, with 5 of 9 mafic clasts falling in a fairly distinct trend through the andesite and dacite fields. Two of the mafic clasts sampled are trachytic in composition, with silica contents in the basaltic andesite to andesite fields. Alkali content is quite variable amongst mafic clasts, with total alkali content of three dacite samples ranging from 4.44 to 7.11 wt. % Na_2O+K_2O, but containing similar silica, ranging from ~64.4–65.5 wt.% SiO_2.

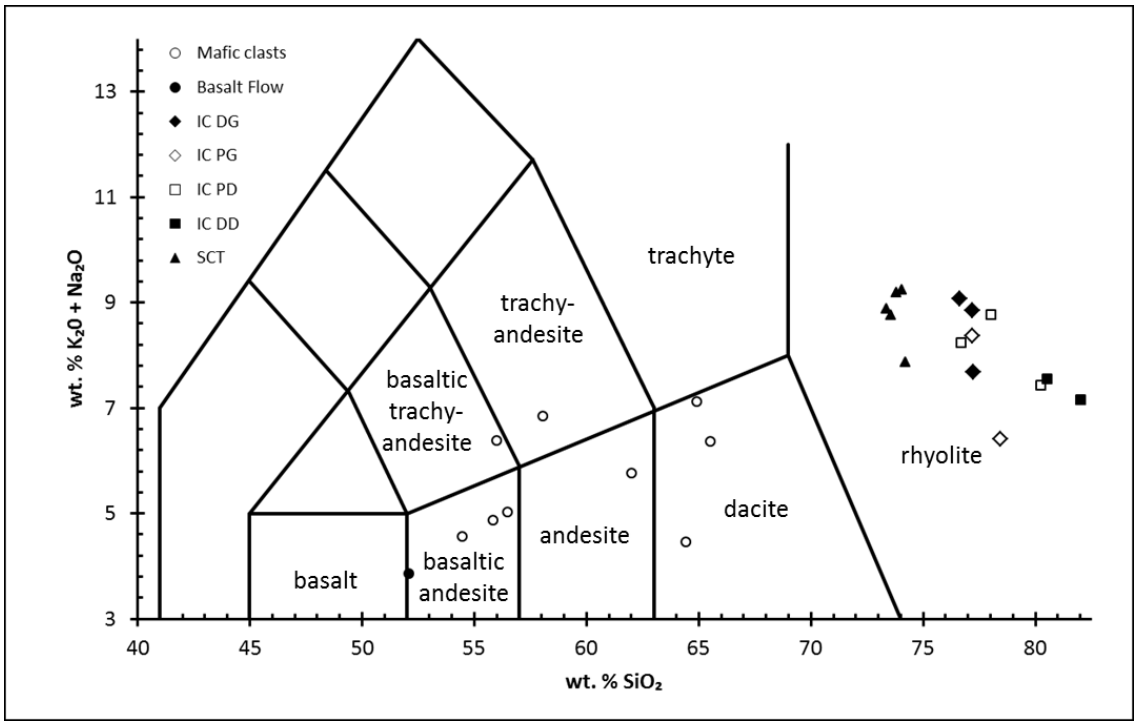

Figure 15: Total alkali versus silica diagram (TAS) for intracaldera units, including dense glassy rhyolite (IC DG), porous glassy rhyolite (IC PG), porous devitrified (IC PD), dense devitrified (IC DD), the tuff of Spring Creek (SCT), mafic clasts entrained within rhyolites, and sample TF-330 from an intra-caldera basalt flow. A significant silica gap appears between ~66 – 72% SiO_2 with a clear separation between local rhyolites and more mafic rocks. Mafic clasts span a wide range in silica content, from ~52% to ~66%, with only two clasts showing trachyitic composition.

Most samples from within Three Fingers caldera are nominally metaluminous to peraluminous, with only dense devitrified rhyolites with molar K_2O+Na_2O/Al_2O_3 greater than 1 (Figure 16), likely representing the effects of alteration. Devitrified samples of both intra-caldera rhyolites and Mahogany Mountain caldera dikes contain both lower aluminum and alkali content compared to other rhyolites. These differences possibly result from mobilization of selected elements during devitrification or later alteration, discussed later in this volume. Higher Ca content of the tuff of Spring Creek

samples distinguishes these from the other groups plotted, containing similar ratios of aluminum to alkalis. Two glassy intra-caldera samples, dense glass lens TF-23B and porous glass TF-32A show significant depletion of alkalis compared to other igneous rocks in this study. Porous devitrified rhyolite sample TF-331 is also anomalously depleted in K and Na, but comparatively enriched in Ca.

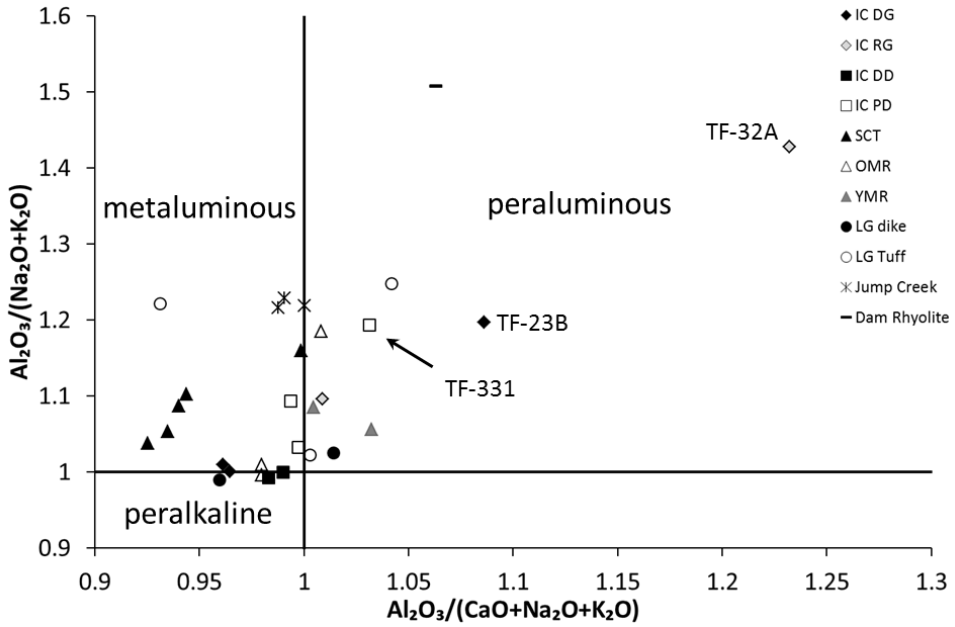

Figure 16: Agpaitic index (y-axis) versus Al index (Maniar and Piccoli, 1989) for intra-caldera rhyolites and other local units shows only dense devitrified samples falling within the peralkaline field, including intra-caldera rhyolites and rhyolite dikes of Mahogany Mountain caldera (IC dike). Tuff of Spring Creek (SCT) samples are distinctly metaluminous, while glassy intra-caldera rhyolites are peraluminous, and show large deviations in alkali content. Considerable scatter is observed in samples from tuff of Leslie Gulch (LG Tuff) as well as older and younger flows of McIntyre Ridge Rhyolite (OMR and YMR, respectively).

Little variation in FeO is observed for glassy intra-caldera rhyolites, falling in a cluster that includes samples of the Mahogany Mountain dike and tuff of Leslie Gulch (Figure 17). Older McIntyre Ridge rhyolites plot concordantly between the tuff of

Spring Creek and intra-caldera glassy rhyolites, with younger McIntyre lavas equivalent to intra-caldera glass in terms of silica content, but falling well off the trend with significantly lower FeO. Note that samples having greater than 80 wt.% SiO_2 are not plotted in this section, but are included later in section 1.3.3.2, where effects of devitrification are discussed.

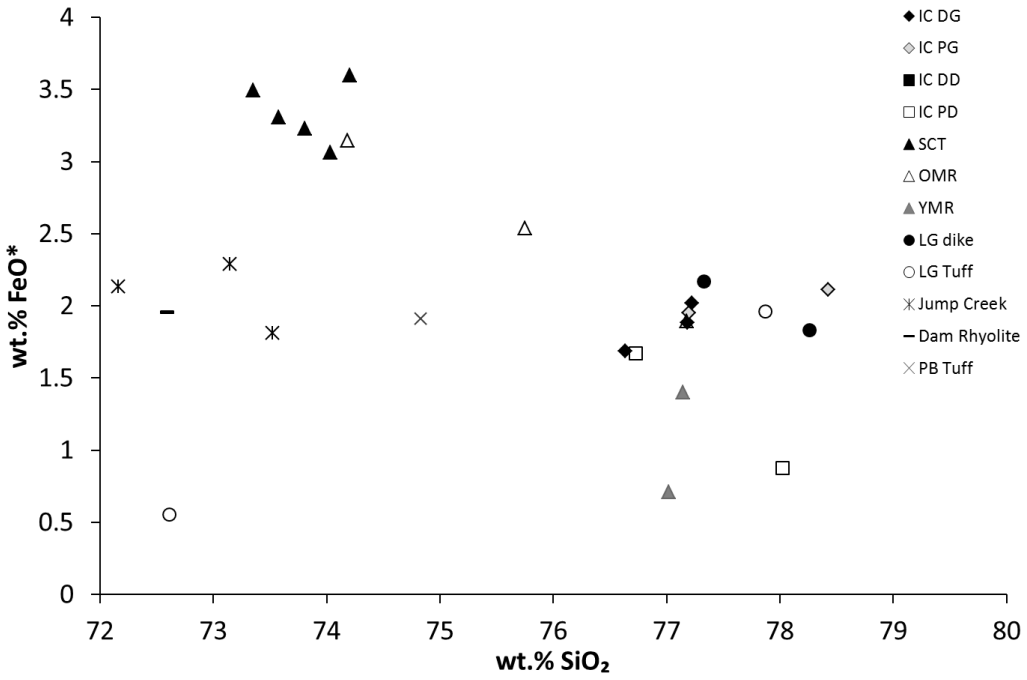

Figure 17: Tuff of Spring Creek contains significantly more iron and less silica than intra-caldera rhyolites and rhyolite dikes of Mahogany Mountain Caldera. Older McIntyre Ridge lavas show a closer affinity to Spring Creek Tuff while younger McIntyre Ridge Rhyolites are more similar to intra-caldera units. Perhaps the most noticeable feature is the low iron content in tuff of Leslie Gulch sample MS-12-39b, which is significantly lower in silica than other Leslie Gulch Tuff samples. Note that samples containing <80 wt.% SiO_2 are not shown in this section, and are discussed later in section 1.3.3.2.

Calcium displays systematic depletion as silica increases (Figure 18), but the pattern is not as distinct as in FeO*. The tuff of Spring Creek contains much higher average CaO than intra-caldera rhyolites (~0.93 versus ~0.40 wt.%), which again

appear as end members in regard to calcium content. Rhyolite dikes within Mahogany Mountain caldera show close affinity to intra-caldera rhyolites and younger McIntyre Ridge Rhyolite flows in terms of calcium, as in other major elements.

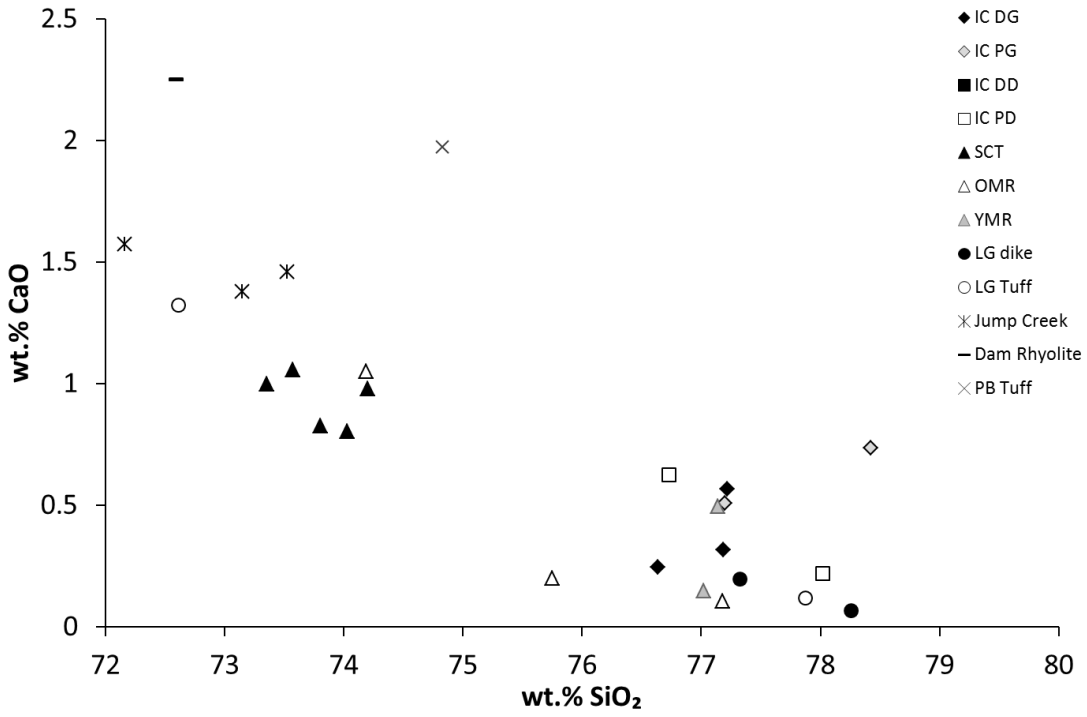

Figure 18: Intra-caldera rhyolites contain less calcium than tuff of Spring Creek, and overall calcium content declines with increasing silica. The majority of McIntyre Ridge Rhyolites are low-Ca, except for one sample of older flows that corresponds closely to tuff of Spring Creek. Tuff of Leslie Gulch samples show large variation in Ca, corresponding to changes in silica content, while cross-cutting dikes in Mahogany Mountain caldera are very similar to intra-caldera rhyolites.

A systematic decrease in titanium content occurs with increased silica content (Figure 19), with the tuff of Spring Creek containing an average of 0.343 wt.% TiO_2, roughly twice the proportion of intra-caldera rhyolites, which average 0.168 wt.% TiO_2. At similar silica values, titanium content in younger McIntyre Ridge Rhyolites is only slightly lower than intra-caldera rhyolites, at 0.152 wt.%. Again, younger McIntyre

Ridge lavas plot very closely to intracaldera glass facies and rhyolitic dikes emplaced within the core of the Mahogany Mountain complex. Jump Creek rhyolites are a later erupted unit with even greater Ti and lower Si than the tuff of Spring Creek, but do not appear to lie on this trend line.

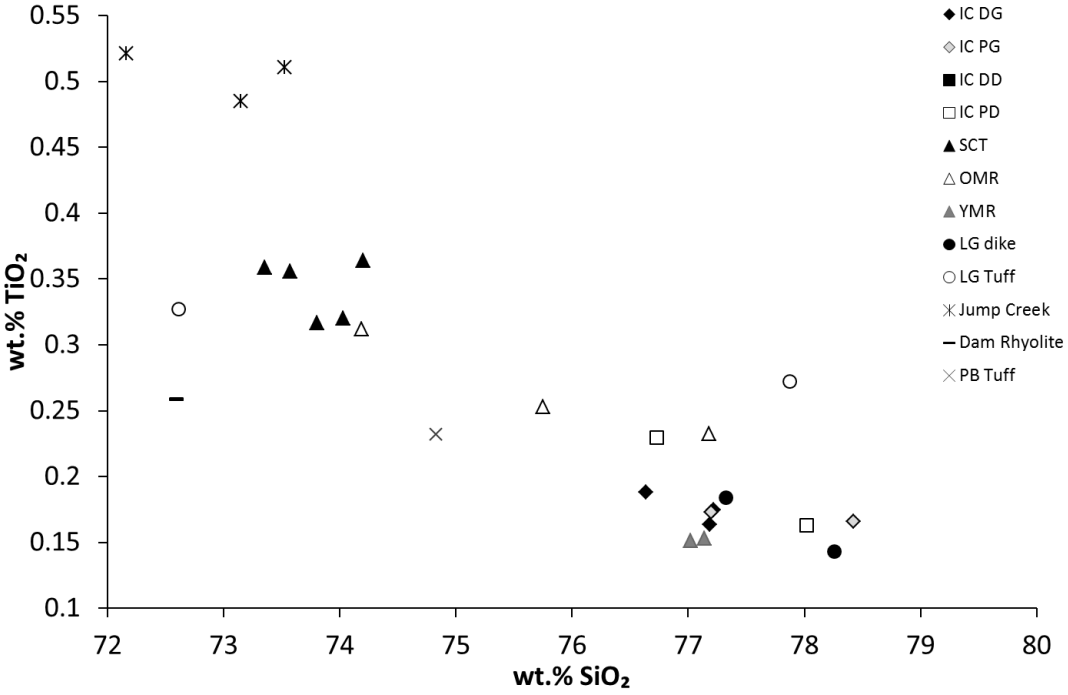

Figure 19: Little variation is observed between devitrified and glassy intra-caldera rhyolites in terms of Ti content, and share close affinity to values for rhyolite dikes of Mahogany Mountain and the majority of McIntyre Ridge Rhyolites. Once again, basal autobreccia of McIntyre Ridge Rhyolite (sample EJ-12) shows close affinity to the tuff of Spring Creek.

Aluminum content also shows an expected inverse correlation with increasing silica (Figure 20), once again showing the tuff of Spring Creek (12.6 wt.% Al_2O_3) and dense devitrified intracaldera rhyolite (9.8 wt.% Al_2O_3) as the two end members. Loss of Al due to alteration in devitrified samples may account for a large proportion of these

differences, as glassy intracaldera rhyolites average 11.9 wt.% Al_2O_3. One sample of the older McIntyre Ridge rhyolite plots within the cluster of tuff of Spring Creek, while others more closely align with glassy intra-caldera rhyolites. Rhyolite dikes within Mahogany Mountain fall directly on the inferred evolutionary path in this case, about halfway between the tuff of Spring Creek and dense devitrified rhyolites in terms of silica content. In this case, porous devitrified facies of intra-caldera rhyolite fall slightly above the trend observed for denser facies, with higher aluminum values, with some plotting very near younger McIntyre Ridge flows.

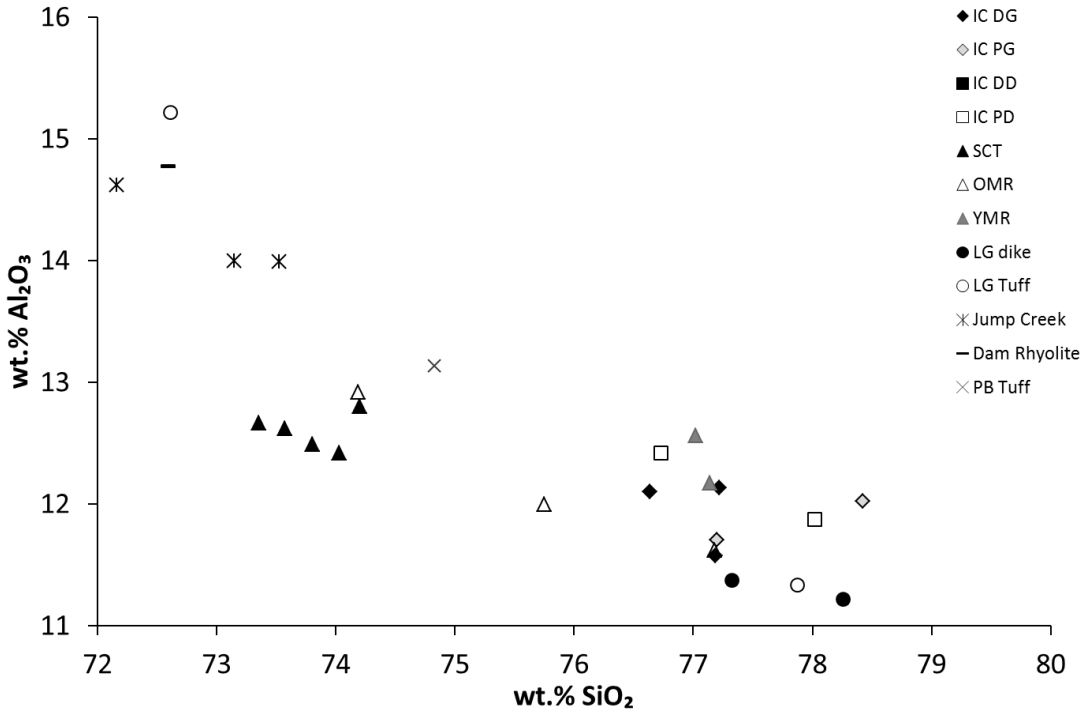

Figure 20: Aluminum versus silica plot for Three Fingers/Mahogany Mountain area. Later erupted Jump Creek Rhyolite and Dam Rhyolite show significantly greater aluminum than those associated with Three Fingers and Mahogany Mountain Calderas, except for one sample of Leslie Gulch Tuff. Intra-caldera rhyolites exhibit significant variability in Al content, with high-Al samples appearing similar to younger McIntyre Ridge Rhyolites, and low-Al samples showing closer affinity to rhyolite dikes of Mahogany Mountain Caldera.

Variations in major element content illustrate that intra-caldera rhyolites are substantially different compositionally than tuff of Spring Creek. Commonly observed as end members in terms of major elements, intra-caldera rhyolites and the tuff of Spring Creek suggest an evolutionary trend beginning with the caldera-forming eruption of the tuff of Spring Creek, followed by eruption of higher silica rhyolites with lower proportions of iron, calcium, titanium, and aluminum. In addition, most major elements show good agreement between intra-caldera rhyolites and those of rhyolitic dikes within the core of Mahogany Mountain caldera and younger McIntyre Ridge Rhyolites.

One sample of older McIntyre Ridge Rhyolite (EJ-12) appears similar in composition to the tuff of Spring Creek, suggesting eruption from a shared magma reservoir.

1.3.3.2 - Effects of devitrification

Noticeable variations in major element content occur between glassy and devitrified facies of intra-caldera rhyolite. Significant reductions in aluminum content, paired with increases in silica appear to correlate with devitrification, when comparing devitrified to nearby glassy rocks originating from the same magma. Dense devitrified intra-caldera samples contain only up to ~10.0 wt.% Al_2O_3, compared to an average of 11.9 wt.% in glassy samples. Both samples of dense devitrified rhyolite contain greater than 80 wt.% SiO_2, with glassy samples averaging only 77.4 wt.%.

Comparison of chemistries for all samples analyzed reveals that devitrified facies of intra-caldera rhyolite have lower concentrations of iron, manganese, magnesium, and calcium than their glassy counterparts (Table 1). In terms of FeO, devitrified samples contain an average of 1.15 wt.%, versus 1.95 wt.% for glassy intra-caldera facies. In addition, glassy samples contain more than three times as much manganese (0.028 versus 0.009 wt.% MnO) and almost four times as much magnesium (0.071 versus 0.019 wt.% MgO) as devitrified samples. Enrichments are also observed in

devitrified samples, which contain greater than four times the phosphorus (0.045 versus 0.01 wt.% P_2O_5) of glassy intra-caldera rhyolites (Table 1). Titanium content appears relatively unaffected by devitrification, possibly making it a useful indicator of devitrification versus magmatic variation.

Dense glassy rhyolite sample TF-299 was collected at the base of Three Fingers Rock, less than 10 meters from dense devitrified sample TF-295. Direct comparison of these two samples shows general decreases in trace element content (Figure 21) with devitrification, corresponding to an increase in silica from 77.2 to 80.5 wt. % SiO_2. A notable exception is the concentration of phosphorus, which is 2 times higher in devitrified TF-295 than in the dense glassy rhyolite (182 ppm versus 76 ppm). The most substantial losses occur in uranium and the REE, with Ba appearing the least affected by devitrification.

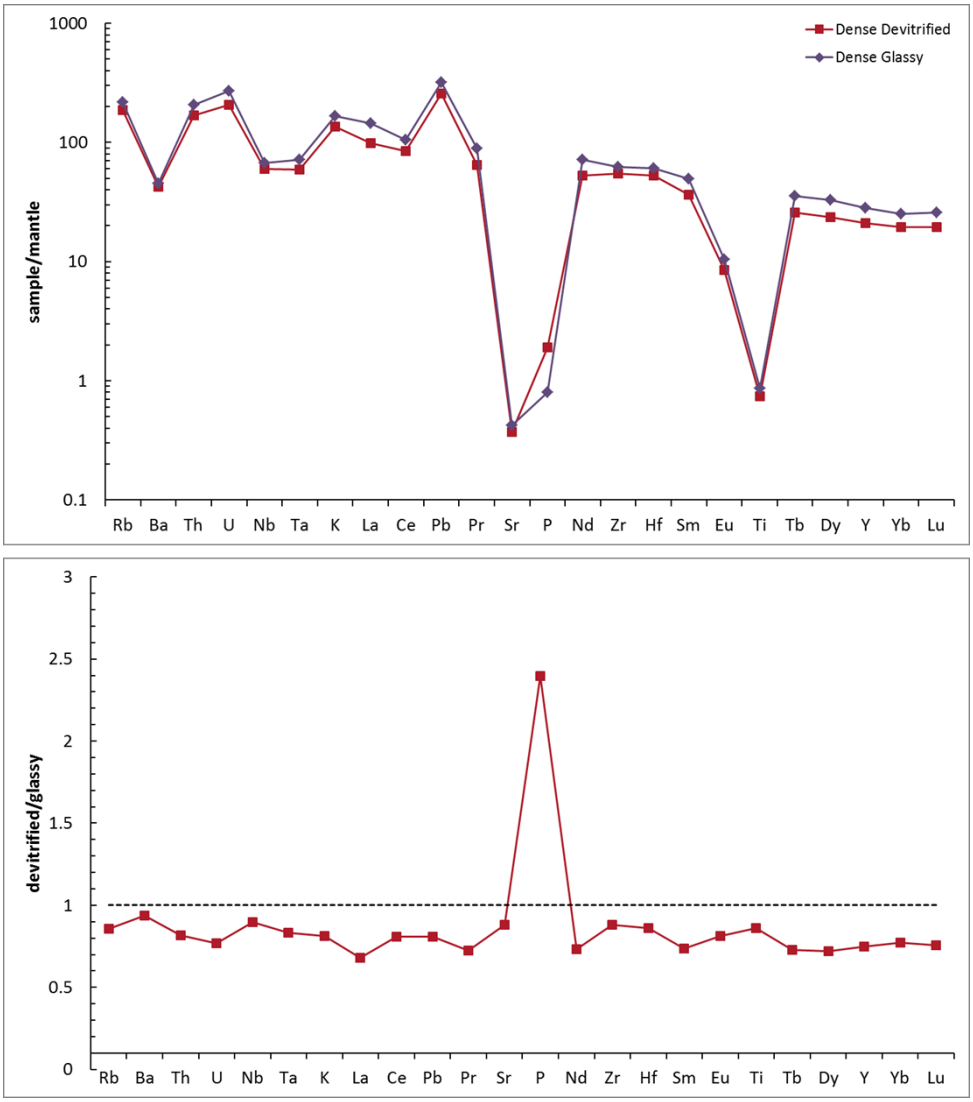

Figure 21: Comparison of elemental concentrations measured in dense devitrified rhyolite sample TF-295 and dense glassy rhyolite sample TF-299 (top) normalized to mantle values of Sun and McDonough (1989). Normalizing the devitrified sample concentrations by the glassy rhyolite concentrations (bottom) shows the most significant loss in lanthanum and uranium content, and the substantially elevated phosphorus content of nearly 2.5 times that of glassy rhyolites.

The difference between dense glassy rhyolites and dense devitrified rhyolites in terms of REE is fairly uniform, except for Ce and Eu content (Figure 22). The two samples here show a greater difference in LREE than HREE content, with devitrified sample TF-295 containing only 67ppm La, compared with 100 ppm La in glassy sample

TF-299. The majority of REE values in sample TF-295 are between 72-77% of those in TF-299, with Ce and Eu at greater than 80%. Whether these elements were mobilized during devitrification is unclear, considering observed increases in silica that would effectively dilute the concentrations of trace elements in devitrified samples.

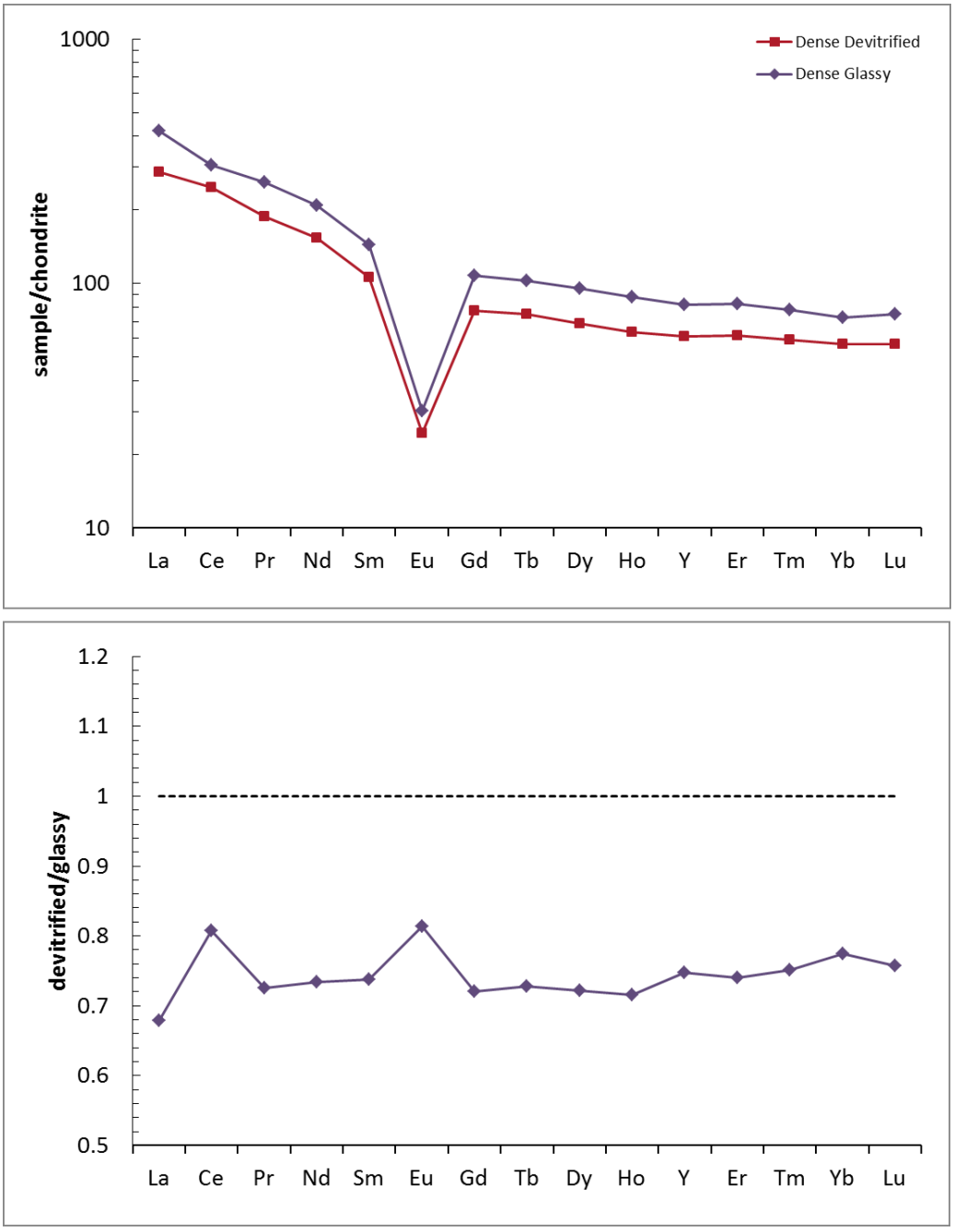

Figure 22: REE content is lower for all elements in dense devitrified rhyolite versus dense glassy rhyolite, as shown in the chondrite normalized REE diagram (top). Devitrified sample TF-295 contains less than 80 percent of nearly all REE contained in glassy sample TF-299 (bottom). Cerium and europium appear less affected by devitrification, with values slightly more comparable to those of dense glassy rhyolites. Chondrite values of Sun and McDonough (1989).

Table 1: Average major element content of glassy and devitrified facies of intra-caldera rhyolites of Three Fingers caldera. Significant variations appear between the two groups, with glassy samples comparatively enriched in aluminum, iron, manganese, magnesium, and calcium. Devitrified facies contain greater phosphorus, and show higher variability in most components.

	Glassy facies				Devitrified facies			
	dense	porous	total	std. dev.	dense	porous	total	std. dev.
SiO_2	77.014	77.812	77.413	0.658	81.281	78.335	79.808	2.117
TiO_2	0.175	0.169	0.172	0.010	0.149	0.177	0.163	0.038
Al_2O_3	11.937	11.864	11.900	0.251	9.801	11.728	10.765	1.199
FeO*	1.863	2.032	1.947	0.162	1.308	0.987	1.147	0.534
MnO	0.029	0.026	0.028	0.006	0.009	0.009	0.009	0.006
MgO	0.062	0.079	0.071	0.060	0.015	0.023	0.019	0.014
CaO	0.376	0.623	0.500	0.198	0.053	0.544	0.298	0.339
Na_2O	3.542	2.761	3.151	0.536	3.354	3.286	3.320	0.869
K_2O	4.996	4.624	4.810	0.741	3.993	4.858	4.426	0.764
P_2O_5	0.011	0.009	0.010	0.005	0.037	0.053	0.045	0.014

Table 2: XRF data for major and trace elements of samples of this study.

	lava flow	mafic clasts											
sample	TF-330	TF-152Fc	TF-388c	TF-431c	TF-316c	TF-21c	TF-218c	BBM-05	TF-158c	386c-B	BBM-01	BBM-04	TF-181c
XRF - wt.% (normalized)													
SiO_2	52.09	54.48	55.86	56.02	56.51	58.06	62.04	62.64	64.44	64.93	64.97	65.33	65.51
TiO_2	1.34	1.30	1.30	1.54	1.38	2.18	1.69	1.46	1.19	1.56	1.02	1.02	1.25
Al_2O_3	16.43	16.09	16.64	17.28	14.86	21.77	20.52	14.76	14.90	16.94	14.32	13.98	14.33
FeO*	10.03	9.22	7.77	8.61	9.82	6.50	3.47	7.20	5.95	5.38	6.10	6.31	6.50
MnO	0.19	0.19	0.20	0.26	0.19	0.10	0.07	0.18	0.18	0.08	0.15	0.17	0.16
MgO	6.22	4.20	3.94	2.45	3.80	0.19	0.37	1.71	1.95	0.19	1.74	1.76	1.34
CaO	9.39	9.63	9.00	7.07	7.97	3.94	5.72	5.95	6.62	3.47	4.80	4.46	4.14
Na_2O	3.20	3.28	3.50	4.00	3.56	4.52	4.01	3.58	3.13	4.07	3.56	3.51	3.52
K_2O	0.66	1.29	1.36	2.38	1.45	2.33	1.73	2.11	1.32	3.04	3.10	3.19	2.84
P_2O_5	0.45	0.34	0.42	0.39	0.45	0.41	0.36	0.41	0.32	0.34	0.24	0.27	0.40
Total	100.00	100.00	100.00	100.00	100.00	100.00	100.00	100.00	100.00	100.00	100.00	100.00	100.00
XRF - ppm													
Ni	76.6	37.1	19.7	18.5	19	7.6	12.8	8	18.1	6.1	5	8	2.5
Cr	142.5	121.9	115	52.6	51.2	n.d.	124.7	22	90.7	2.5	22	8	2.6
Sc	31.8	34.7	34.8	31.7	32.9	27.3	26.3	24	28.9	9.9	15	14	19.8
V	264.8	277.3	270.8	299.8	297.4	309.7	204.8	302	253.1	235.7	198	195	33.1
Ba	449.1	436.2	454.3	671.1	565.2	869.2	541.1	733	448.2	830.5	614	769	1002.8
Rb	15.7	29.6	23.3	44.5	52.1	30.8	28.6	41.3	17.7	54.3	50.7	60.8	80.8
Sr	447.5	389.1	376.9	374	355.5	371.7	533.9	354	366.7	359.6	260	249	310
Zr	137.2	157.9	186.2	252.4	202.2	226.9	166.6	188	217.6	278.5	353	289	255.9
Y	31.2	76.6	562.2	822.9	73.2	429.5	537.7	182.5	88.5	1108.4	260.1	121.8	48.4
Nb	9.2	22	32.7	45.2	14	30.9	11.7	38.4	18.5	95.5	44.6	32.8	15.5
Ga	17.8	20	25.1	36.4	20.4	38.3	35.5	22	23.1	33.6	28.8	32.8	20
Cu	87.5	119	21.9	18.9	126.3	29.1	53.6	67	97.5	3	33	20	8.4
Zn	105.1	117.8	390.8	293.4	125.9	1944.8	1829.4	126	156.7	177.9	195	277	117.2
Pb	4.6	7.3	29.2	49.9	7.9	91	79	14	9.1	55.7	64	45	14.7
La	15.7	26.7	671.5	1515.4	35.2	984.2	770.2	35	45.1	546.1	186	372	32.1
Ce	43.6	46.2	849.3	579.7	60.7	3123	1710.5	80	92.3	1539.7	241	923	74.5
Th	1.5	2.8	6.9	6.1	3.5	4.5	2.8	3.8	5.2	18.2	11.5	11.2	8.1
Nd	24.5	31.7	770.5	2439.9	33	1706.6	1002.7		52.3	948.8			40.1
U	1.6	7.5	19.3	47.4	0.6	27.8	4.4	11.1	5.4	34	23.1	11.7	4.2
Cs	0		1.5	2.2	1.1	4.7			0	3			

Table 2 (continued): Geochemical data for major and trace elements of samples of this study.

	lava flow	mafic clasts										
sample	TF-330	TF-152Fc	TF-388c	TF-431c	TF-316c	TF-21c	TF-218c	BBM-05	TF-158c	386c-B	BBM-01	BBM-04	TF-181c
ICP-MS - ppm													
La	18.2	24.8	661.9	1491.3	35.5	969.9	841.6		42.4	552.1			33.6
Ce	40.1	44.0	854.5	577.5	62.0	3150.7	1819.2		89.7	1476.6			71.0
Pr	5.2	7.2	167.4	589.5	8.2	482.6	262.9		11.7	254.0			9.3
Nd	22.5	31.1	739.0	2312.9	35.1	1640.5	1125.8		49.4	909.0			38.7
Sm	5.3	8.3	202.2	579.1	8.4	352.5	282.6		13.7	198.1			8.9
Eu	1.7	1.7	6.2	16.5	1.8	11.3	11.6		1.5	6.7			2.3
Gd	5.5	9.9	196.8	334.2	10.2	165.3	279.1		15.5	120.0			8.7
Tb	0.9	1.9	31.4	58.4	1.7	25.7	37.8		3.1	25.5			1.4
Dy	5.7	13.2	182.2	295.0	11.3	116.5	161.3		21.4	198.7			9.1
Ho	1.2	2.9	32.3	48.4	2.5	18.1	22.0		4.4	49.7			1.9
Er	3.3	8.7	84.3	114.5	6.8	42.2	39.7		12.0	159.1			5.1
Tm	0.5	1.3	12.3	15.3	0.9	5.4	4.2		1.7	25.0			0.8
Yb	3.0	8.4	79.9	87.1	5.5	30.3	20.6		9.8	152.1			4.8
Lu	0.5	1.3	11.4	11.6	0.9	4.5	2.8		1.4	23.0			0.8
Ba	441.3	435.2	437.7	652.2	555.7	861.3	564.0		446.6	822.7			1045.3
Th	1.4	2.7	5.9	5.3	4.0	4.5	2.9		4.5	18.4			7.6
Nb	8.8	21.0	31.5	44.6	13.9	30.0	12.2		17.4	94.7			15.3
Y	30.1	76.8	642.6	1012.2	72.7	478.2	630.2		86.6	1650.8			48.4
Hf	3.4	4.1	5.0	7.1	5.3	6.0	4.9		5.9	7.2			6.9
Ta	0.5	0.6	0.7	1.0	0.8	0.8	0.7		0.9	1.2			1.0
U	0.5	7.0	18.8	46.3	1.6	28.0	4.5		5.0	34.1			3.4
Pb	4.4	7.5	31.4	57.0	8.3	97.0	87.9		8.8	56.8			14.4
Rb	14.1	29.7	23.8	45.3	49.9	31.0	31.2		16.9	56.9			83.6
Cs	0.5	0.6	0.8	1.7	2.2	0.8	1.0		0.5	2.7			3.5
Sr	441.4	395.8	389.9	390.6	355.3	388.0	571.3		366.0	373.4			321.0
Sc	31.9	35.0	34.4	32.8	31.8	27.4	27.3		29.3	10.2			19.8
Zr	133.4	156.5	184.9	255.6	196.8	230.7	178.5		212.2	283.0			260.0

Table 2 (continued): Geochemical data for major and trace elements of samples of this study.

	dense glass			porous glass		porous devitrified			dense devitrified		tuff. sed.	volc. ss
sample	TF-23B	TF-88A	TF-299	TF-32A	TF-157A	TF-127	TF-213	TF-331	TF-295	TRP-1	TF-46	TF-407
XRF - wt.% (normalized)												
SiO_2	77.22	77.19	76.63	78.43	77.20	78.02	76.73	80.26	80.53	82.03	87.31	82.94
TiO_2	0.17	0.16	0.19	0.17	0.17	0.16	0.23	0.14	0.16	0.14	0.12	0.17
Al_2O_3	12.13	11.58	12.10	12.02	11.71	11.87	12.42	10.90	10.03	9.57	7.25	9.36
FeO*	2.02	1.88	1.69	2.11	1.95	0.88	1.67	0.41	1.63	0.99	0.20	0.23
MnO	0.04	0.03	0.02	0.02	0.03	0.00	0.02	0.00	0.01	0.01	0.01	0.00
MgO	0.15	n.d.	0.03	0.10	0.06	0.01	0.03	0.03	0.00	0.03	0.00	0.00
CaO	0.57	0.32	0.24	0.74	0.51	0.22	0.63	0.79	0.06	0.05	0.05	0.04
Na_2O	3.23	3.34	4.05	2.64	2.88	3.58	4.33	1.94	3.45	3.26	1.69	1.92
K_2O	4.45	5.51	5.03	3.77	5.48	5.18	3.90	5.49	4.10	3.89	3.36	5.32
P_2O_5	0.01	0.01	0.02	0.01	0.01	0.07	0.05	0.04	0.04	0.03	0.01	0.02
Total	100.00	100.00	100.00	100.00	100.00	100.00	100.00	100.00	100.00	100.00	100.00	100.00
XRF - ppm												
Ni	3.4	1.9	1	1	2.8	2.2	1	0.5	2.8	0	2.3	1.4
Cr	2.9	2.1	3.1	3.2	3.5	6.3	2	3.7	1.5	3	2.3	4.2
Sc	0.3	0	0.6	0.6	0.2	2	2.2	1.5	0.9	2	0.6	0.6
V	3.5	2.8	5.9	0	5	7.9	5.3	1.7	9.1	3	1.9	2.9
Ba	183	130.6	316.8	188.5	165.4	388.2	558.5	80.3	294.4	94	464.3	476.6
Rb	185.4	146.2	136.7	168.1	142.5	121	100.2	122.2	115.7	98	84.0	134.7
Sr	4.4	3	6.8	16.3	11.4	24.4	30.4	23.7	5.6	5	3.2	8.5
Zr	598.1	670.5	688	562.4	672.3	320.5	477.1	575.4	594.7	555	353.8	499.6
Y	126	121.6	130.9	92.8	113.2	69.4	92.5	105.8	98.4	102	83.6	91.8
Nb	46.9	47.1	48.4	44	47.2	33	28.8	42.6	42.9	42.3	26.9	36.1
Ga	27.1	26.1	26.6	25.8	26.2	24.5	23.4	26.7	24.2	28	20.8	18.0
Cu	6.1	5.2	3.6	5.1	6.7	4.6	4.5	1.6	2.8	3	1.0	1.0
Zn	193	193.1	258.2	171.4	191.5	31.7	74.5	17.9	103	50	32.9	11.0
Pb	30.5	27.7	23.2	21.6	26.3	16	17.7	53.4	18.9	11	3.4	6.4
La	81	73.4	99.5	68	69.4	50.6	88	69.9	67.2	37	33.1	40.4
Ce	159.1	153	173.7	146	143.8	105.5	174.4	122.2	140.8	87	65.5	72.9
Th	18.2	16.6	18.3	14.3	16.5	13.1	11.4	17.5	14.2	14	10.4	11.9
Nd	82.2	76.1	99.1	70.7	73.3	51.4	79.8	72.2	72.1	46	36.5	43.3
U	5.1	5	6.5	4	5.5	3.4	1.4	3.6	2.9	6	3.5	6.2
Cs			3.2					3.4	3.7	1186		0.9

Table 2 (continued): Geochemical data for major and trace elements of samples of this study.

	dense glass			porous glass		porous devitrified			dense devitrified		tuff. sed.	volc. ss
sample	TF-23B	TF-88A	TF-299	TF-32A	TF-157A	TF-127	TF-213	TF-331	TF-295	TRP-1	TF-46	TF-407
ICP-MS - ppm												
La	87.7	76.3	99.5	72.4	75.6	53.0	93.1	69.2	67.6		32.9	39.5
Ce	172.1	164.7	187.1	158.0	162.7	109.1	192.7	131.7	151.1		67.5	75.7
Pr	21.7	20.2	24.6	18.7	20.1	13.5	22.6	18.5	17.9		9.4	10.7
Nd	86.1	81.2	97.6	74.2	80.3	52.5	87.2	73.6	71.6		37.4	42.6
Sm	20.1	19.4	22.0	17.3	18.7	12.3	17.6	17.3	16.3		9.7	10.2
Eu	1.4	1.2	1.7	1.2	1.2	0.9	1.3	0.9	1.4		1.1	1.1
Gd	20.7	19.9	22.1	17.4	18.7	11.9	17.1	16.9	15.9		11.1	10.8
Tb	3.6	3.6	3.8	3.1	3.3	2.1	2.9	3.1	2.8		2.1	2.1
Dy	23.2	22.9	24.2	19.1	21.1	13.7	18.1	19.8	17.5		13.8	14.2
Ho	4.8	4.8	5.0	3.8	4.4	2.9	3.6	4.2	3.6		3.0	3.2
Er	13.5	13.4	13.7	10.5	12.5	8.2	8.9	11.6	10.1		8.6	9.2
Tm	2.0	2.0	2.0	1.5	1.9	1.3	1.2	1.7	1.5		1.3	1.4
Yb	12.3	12.5	12.4	10.1	11.7	8.1	6.8	10.9	9.6		7.9	8.7
Lu	1.9	1.9	1.9	1.5	1.8	1.3	1.0	1.6	1.4		1.2	1.3
Ba	186.5	135.2	315.8	194.5	174.7	409.7	603.5	83.1	295.6		483.4	480.3
Th	17.9	17.3	17.5	16.1	17.3	13.4	12.2	17.3	14.4		10.6	12.3
Nb	48.2	47.6	47.9	44.7	48.6	33.4	29.4	42.8	42.9		27.6	36.0
Y	126.6	122.5	128.3	93.0	114.1	68.1	93.0	103.4	95.9		80.3	89.6
Hf	18.0	19.4	18.8	17.4	19.2	10.1	13.0	17.2	16.2		10.3	13.6
Ta	3.1	3.0	2.9	2.9	3.0	2.1	1.8	2.3	2.4		1.6	1.9
U	5.5	5.1	5.7	4.0	4.9	3.7	3.2	4.4	4.3		2.4	5.6
Pb	28.5	26.6	22.7	20.1	25.4	15.8	16.9	50.8	18.3		3.1	5.5
Rb	190.4	155.6	138.2	175.0	151.1	127.7	107.6	125.8	118.4		88.0	140.4
Cs	7.2	4.0	5.8	6.4	3.8	1.6	2.7	4.2	2.0		0.6	1.1
Sr	6.5	5.1	8.9	18.5	13.8	27.5	34.0	28.1	7.8		4.7	10.9
Sc	0.1	0.1	0.3	n.d.	0.4	1.8	1.9	0.2	0.2		0.5	0.6
Zr	637.7	714.4	697.9	608.3	715.4	326.7	507.7	610.0	613.8		380.7	526.4

1.3.3.3 – Trace elements

Intra-caldera rhyolites and other rhyolites of the Three Fingers/Mahogany Mountain area show similar compositions for the majority of incompatible trace elements with a few exceptions. This becomes evident in a mantle-normalized multi-element diagram (Figure 23). The considerable variation seen in Sr and P content may be explained by devitrification. Europium is also similar in both Spring Creek and Leslie Gulch ash flow tuffs, and substantially higher than in later erupted rhyolites, with tuff samples averaging 2.95 ppm, versus 1.22 ppm for later rhyolites.

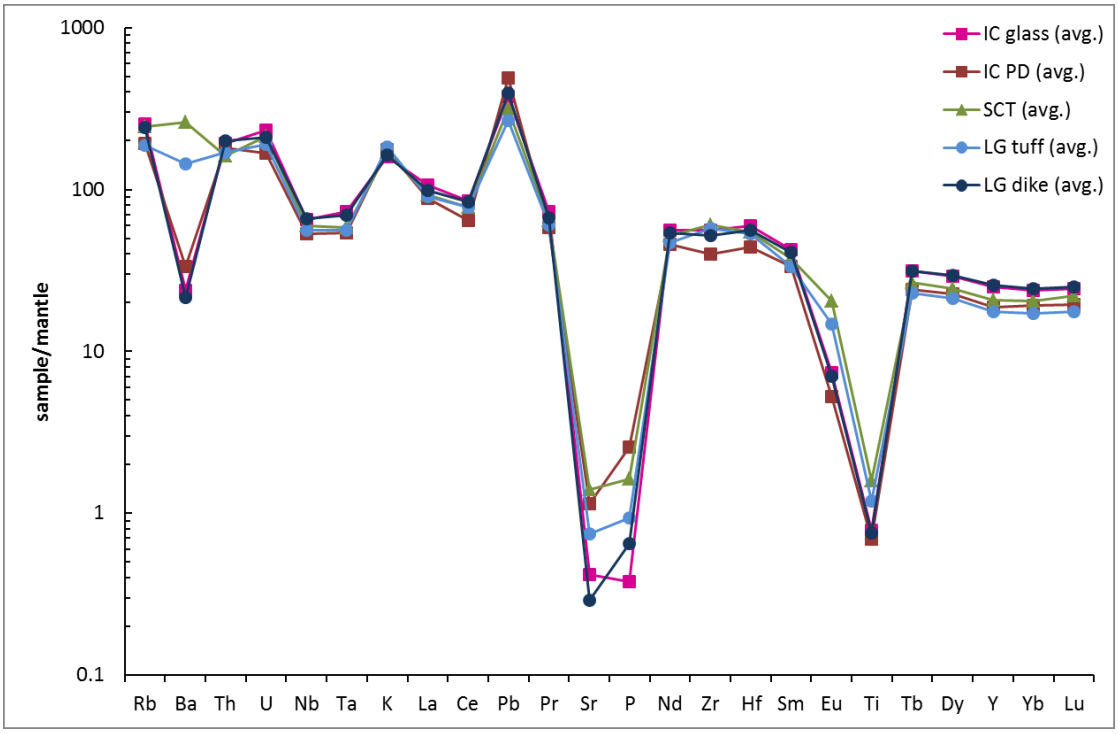

Figure 23: Significant variation is observed in Ba and Eu content between caldera forming ash flow tuffs and later erupted intra-caldera rhyolites. Variability in Sr and P between facies may be due to effects of devitrification and porosity.

A relative enrichment or depletion of barium compared to neighboring elements Rb and Th is a distinctive feature between the early erupted caldera-forming tuff of Spring Creek and the tuff of Leslie Gulch versus later erupted intra-caldera rhyolites of Three Fingers and Mahogany Mountain calderas. The highest Ba content observed in intra-caldera units is 559 ppm, in the porous devitrified facies. Five samples of the tuff of Spring Creek collected by Streck (unpublished data, 2012) all contain more than 1500 ppm Ba, clearly distinguishing them from intra-caldera rhyolites.

Intra-caldera rhyolite facies show similar Zr values to those of the tuff of Spring Creek (Figure 24) and older flows of McIntyre Ridge Rhyolite (~550-750 ppm). While younger McIntyre Ridge Rhyolites show similarly low Ba values to other intra-caldera units, they are here distinguished from intra-caldera rhyolites, containing much lower Zr, with both samples falling near 300 ppm. One sample of porous devitrified rhyolite plots close to the younger McIntyre samples for both elements, but only slightly higher in barium. Amongst the intra-caldera rhyolites, the porous devitrified rocks show substantial heterogeneity in the distribution of Zr, with dense and glassy facies falling in two distinct groups.

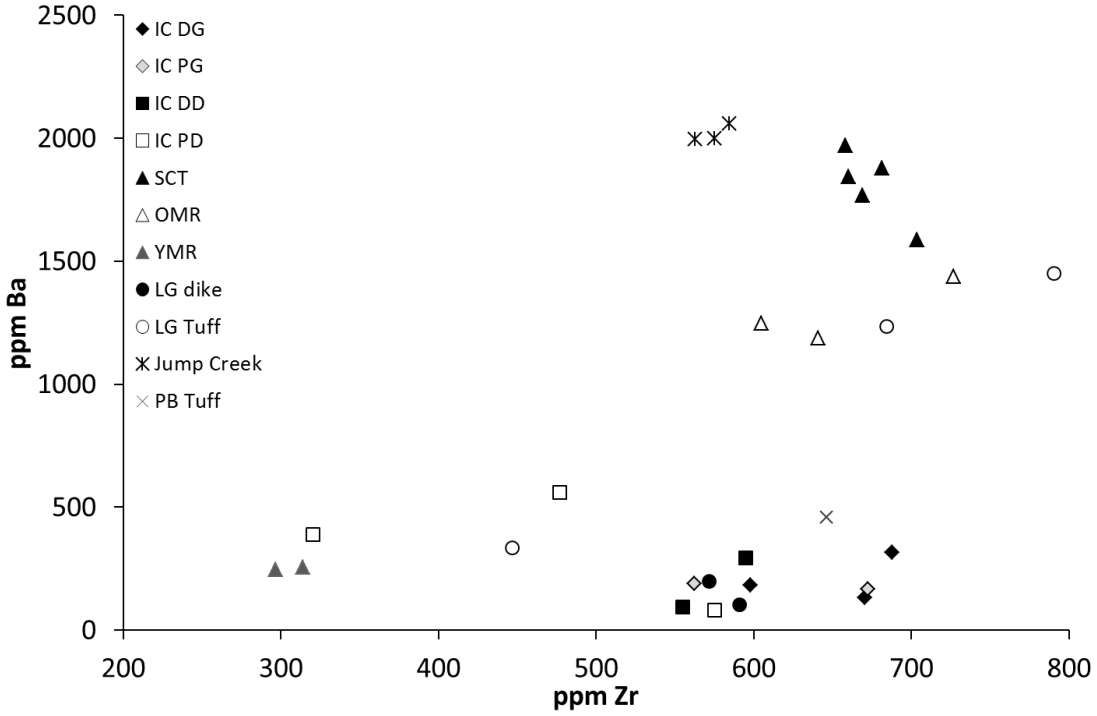

Figure 24: Tuff of Spring Creek contains considerably greater Ba than intra-caldera rhyolites, with nearly equivalent Zr. Younger McIntyre Ridge Rhyolites (YMR) are distinctly lower in Zr than intra-caldera rhyolites, with one Leslie Gulch Tuff sample plotting in the low-Ba field and the other two showing much higher Ba.

When comparing Ba to Sr, dense glassy and devitrified samples of intra-caldera rhyolite are comparatively depleted in both elements versus the tuff of Spring Creek. Porous samples become significantly more enriched in Sr, but do not show corresponding increases in Ba content. All three tuff of Leslie Gulch samples plot between values for dense intra-caldera rhyolites and the majority of the tuff of Spring Creek samples.

All rhyolites compared display relative depletions in Nb and Ta versus neighboring elements, with intra-caldera rhyolites of Three Fingers differentiated from

samples of Mahogany Mountain and outflow tuff of Spring Creek in relative abundances between the two. Intra-caldera rhyolites of Three Fingers show a slight increase in Ta versus Nb, while other units show no relative enrichment of Ta. Nb values for intra-caldera glass and Mahogany Mountain dikes are similar (46.3 and 45.6 ppm, respectively).

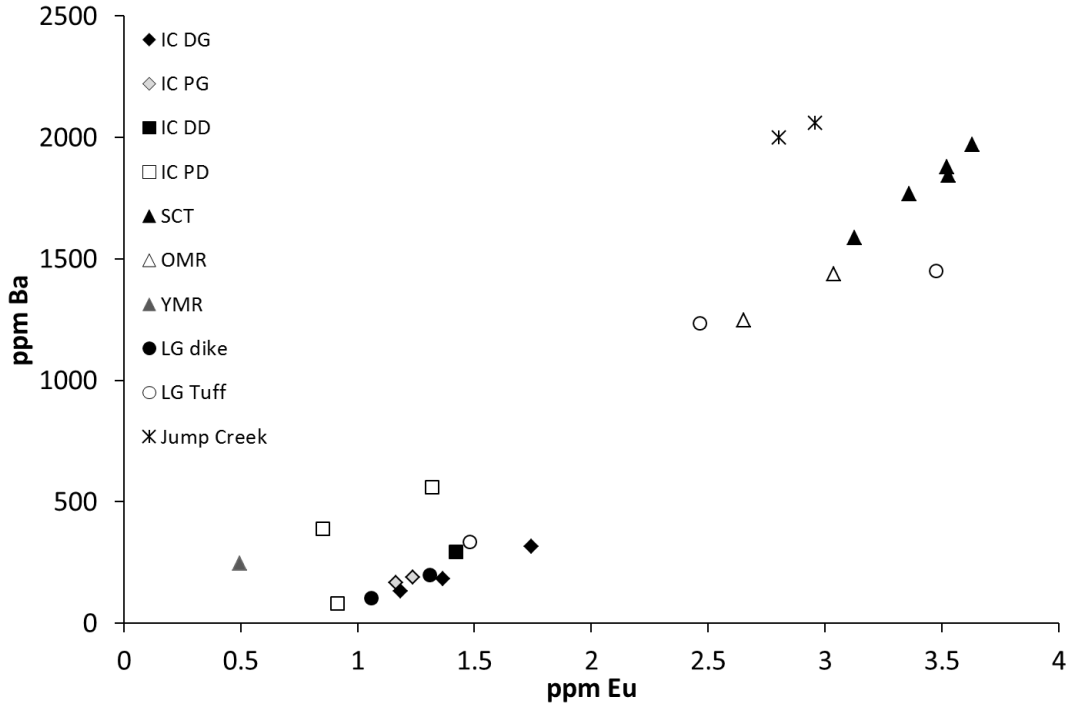

Figure 25: Concentrations of barium and europium display strong correlation, ranging from high values for both elements in slightly older tuff of Spring Creek to much lower for later intra-caldera rhyolites.

Relative abundances of Eu and Ba show strong correlations between units of the Three Fingers/Mahogany Mountain area (Figure 25). Glassy samples of both the tuff of Spring Creek and intra-caldera rhyolites fall in distinct fields, with porous devitrified rhyolites showing slight enrichment in Ba compared to other intra-caldera rhyolite

samples. Intra-caldera rhyolites contain very low Eu and Ba, with dense glassy rhyolite averaging only 1.34 ppm Eu, and 201 ppm Ba, compared to values of the tuff of Spring Creek (3.43 and 1908 ppm, respectively). Also notable are similarities of the Mahogany Mountain dikes to intra-caldera glassy rhyolites with respect to these two elements (1.19 ppm Eu, 149 ppm Ba).

Trace element patterns for caldera-forming ash-flow tuffs are distinctly different than intra-caldera rhyolites in terms of Ba, Eu, and Ti concentrations (Figure 26). A very similar pattern is seen for older McIntyre Ridge Rhyolite flows, with values nearly identical to tuffs of Spring Creek and Leslie Gulch. Average values for intra-caldera dikes of Mahogany Mountain once again show distinct similarities in terms of their overall trace element content, represented as a nearly flat line at a value of 1.0. Perhaps the most diagnostic feature of this normalization are the correspondence between Leslie Gulch dikes and intra-caldera glassy rhyolites for Ba, Eu, and Ti.

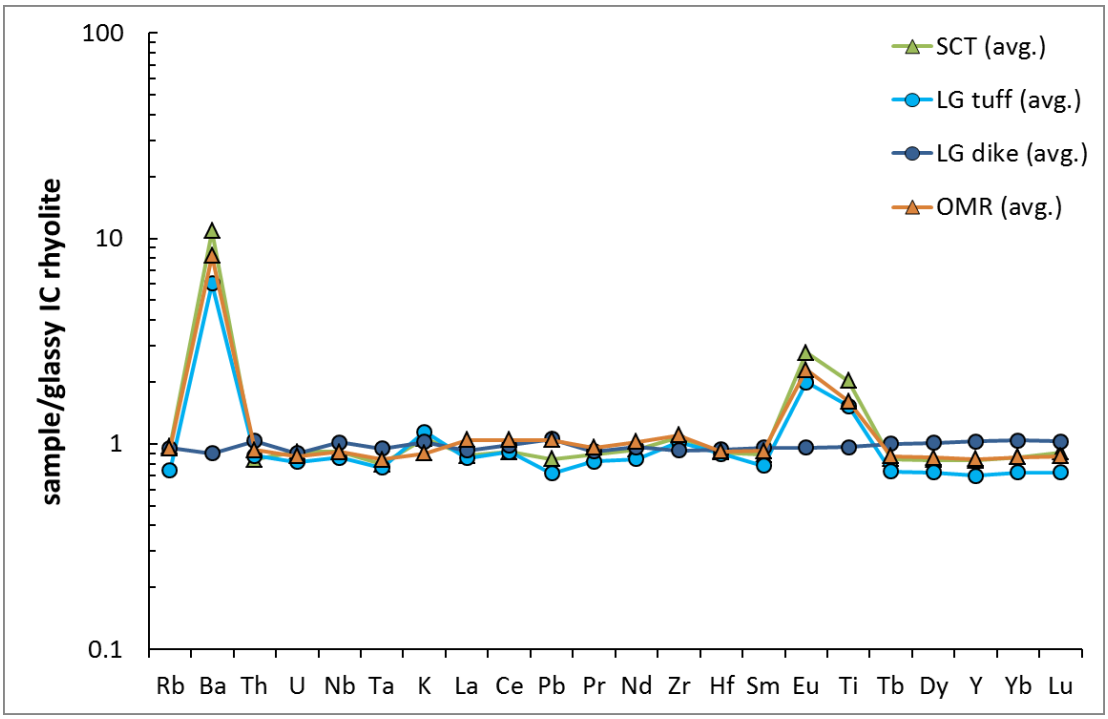

Figure 26: Average trace element content for rhyolites of Three Fingers/Mahogany Mountain area, normalized to dense glassy intra-caldera rhyolite. Ba, Eu, and Ti vary between older McIntyre Ridge Rhyolites (OMR) and early erupted ash-flow tuffs versus later intra-caldera rhyolites in both calderas. Dikes within Leslie Gulch (LG Dike) show nearly identical values to intra-caldera rhyolites of Three Fingers caldera, as evidenced by the flat line.

1.3.3.4 – Geochemistry – Tuffaceous sediment

When compared to likely source rhyolites, tuffaceous sediments have higher silica contents (average of 87.3 wt.% SiO_2), and very low wt.% FeO (average of 0.199). While most major elements show depletion from values of nearby primary rhyolite units, K_2O remains at 3.36 wt.%. Trace element composition shows relative depletions in nearly all trace metals except barium (483.39 ppm), which is more than double the value of dense intracaldera glassy rhyolite (avg. 172.73 ppm), and more comparable to values of porous devitrified rhyolite, which contains an average of 342.33 ppm Ba.

Light rare earth elements (LREE) are consistently depleted in these sediments as well, with total LREE (La, Ce, Pr, Nd, Sm, Eu, Gd) less than half of intracaldera rhyolite glass (169 vs. 382 ppm), and just over half of the value for the tuff of Spring Creek (332 ppm).

1.3.3.5 - Geochemistry – Mineral Phases

Electron microprobe data was acquired from the work of Elizabeth Brown and Brian Webb (Appendix 1B) during the summer of 2012. Analysis of alkali feldspars from the tuff of Spring Creek and intra-caldera rhyolites show these have distinctly different compositions (Figure 27, top). Intra-caldera rhyolite feldspars are more potassium-rich, and calcium-poor, averaging 0.8% of the $CaAl_2Si_2O_8$ component (An), 45.1% $NaAlSi_3O_8$ (Ab), and 54.1% $KAlSi_3O_8$ (Or), compared to 5.8% An, 52.1% Ab, and 42.1% Or for the tuff of Spring Creek feldspars. All but one alkali feldspar are categorized as sanidine, with one analysis of the tuff of Spring Creek plotting within the anorthoclase field.

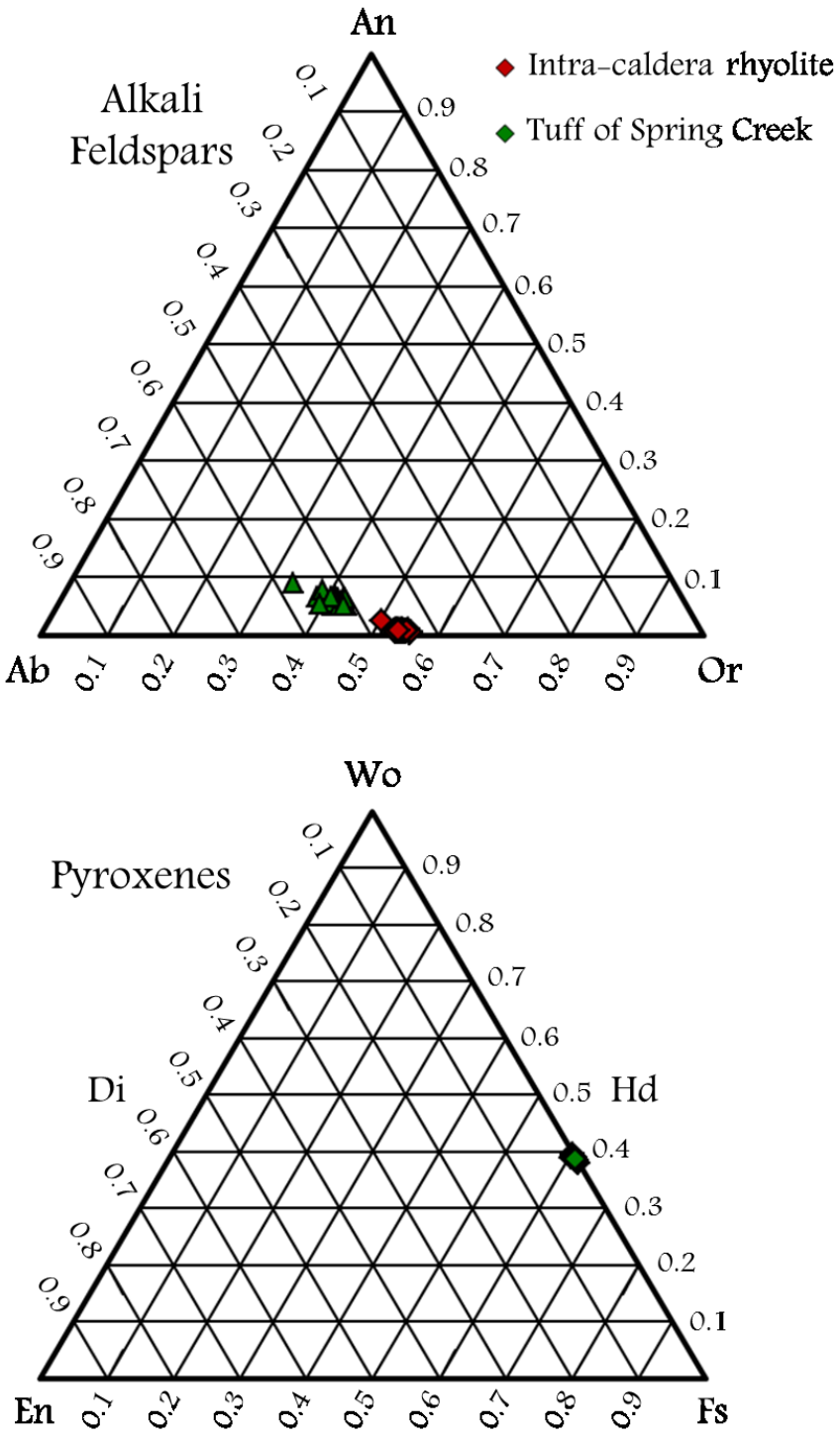

Figure 27: Pyroxenes (bottom) in tuff of Spring Creek and intra-caldera rhyolite show identical compositions, but alkali feldspar compositions (top) are significantly different, containing greater sodium and calcium in tuff of Spring Creek.

In addition to lower potassium, feldspars from the tuff of Spring Creek show considerably higher barium content (Figure 28). A wide range of values are displayed for BaO in both units, from 0.91–1.7 in feldspars of the tuff of Spring Creek, to 0.11–0.99 for those of intra-caldera rhyolites, with little overlap. Potassium values are also variable in Spring Creek Tuff, ranging from 4.2–5.5 wt.% K_2O in a pattern that does not correlate with Ba fluctuations. In contrast, potassium values show little scatter for intra-caldera rhyolites, falling between ~7.2–7.6 wt.% K_2O, except for one analysis at 6.6 wt.% K_2O.

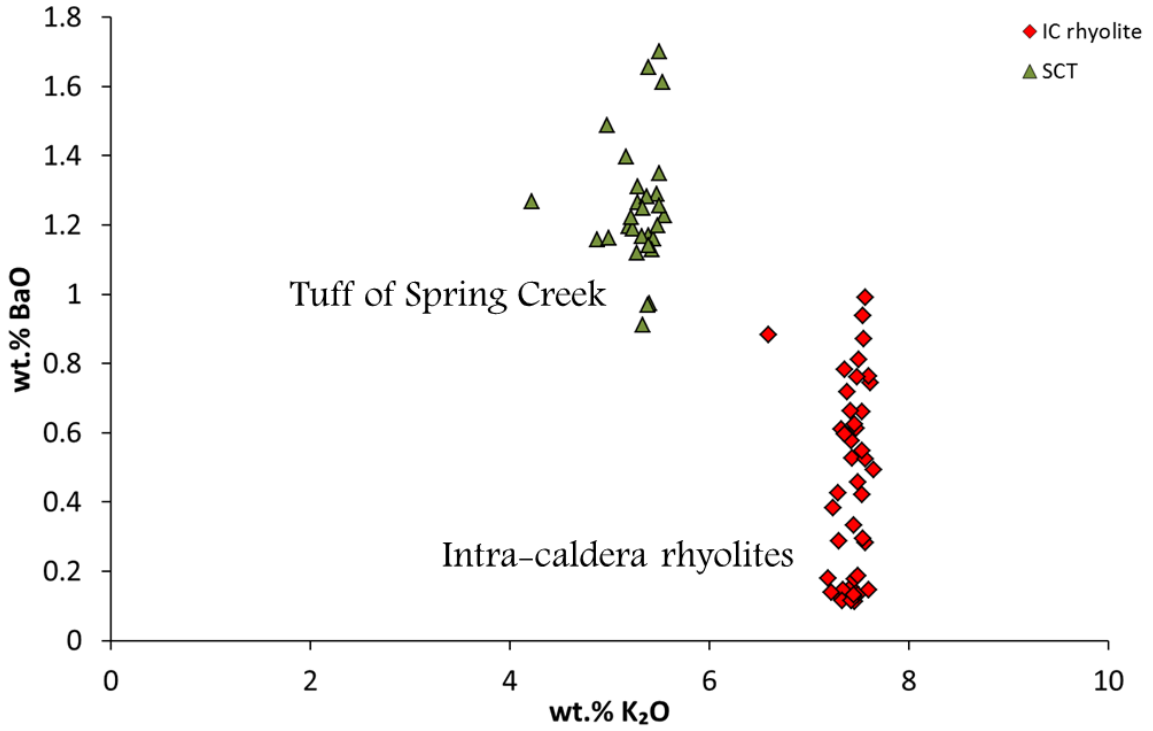

Figure 28: Alkali feldspar analyses display two distinct compositional groups for the tuff of Spring Creek and intra-caldera rhyolites, with intra-caldera feldspars containing more potassium. Both groups display a wide range of barium content, but this range is much higher for feldspar of the tuff of Spring Creek.

Geochemical analysis of pyroxenes of the tuff of Spring Creek and the intra-caldera rhyolite show that the pyroxenes in both units are similar in terms of MgO, FeO, and CaO (Figure 27, bottom), plotting as Fe-rich augites close to values for hedenbergite (Morimoto, 1988). Normalized values for the tuff of Spring Creek pyroxenes average 38.7% $Ca_2Si_2O_6$ (Wo), 61.0% $Fe_2Si_2O_6$ (Fs), and 0.3% $Mg_2Si_2O_6$ (En), and those of intra-caldera rhyolites averaging 38.9% Wo, 60.9% Fs, and 0.2% En. Distinct differences exist in Na_2O and TiO_2 content however (Figure 29), with pyroxenes of intra-caldera rhyolites containing more sodium and less titanium than those of the tuff of Spring

Creek, falling in two distinct fields. Sodium values show greater variability in intra-caldera rhyolites versus titanium, with greater variability shown by titanium in the tuff of Spring Creek.

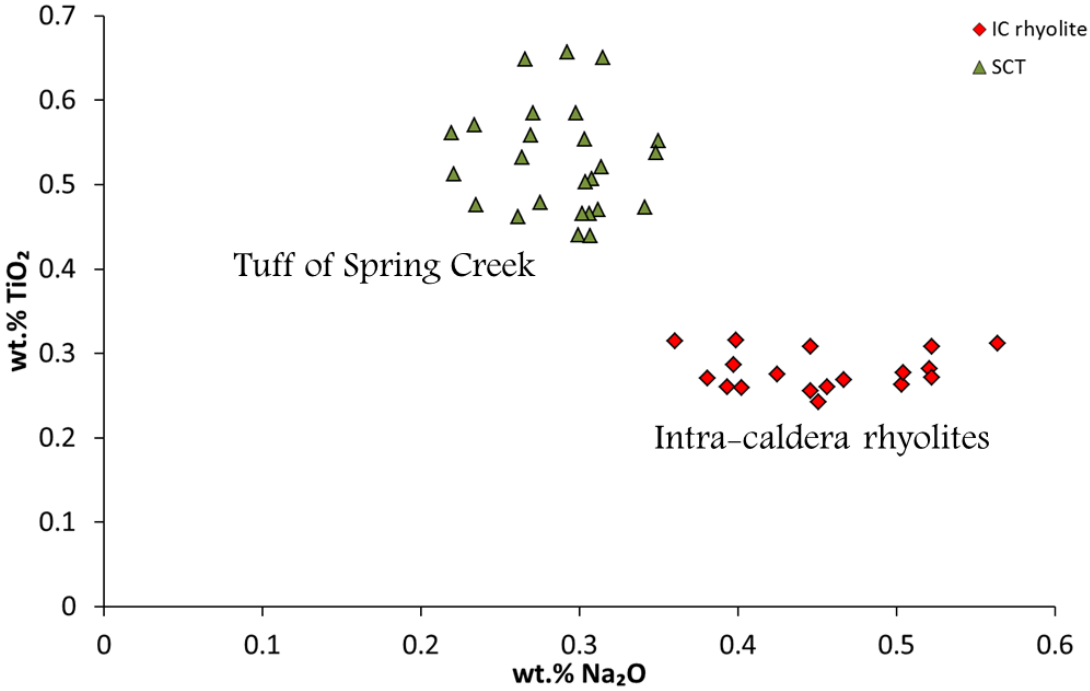

Figure 29: Pyroxenes of intra-caldera rhyolite contain more sodium and less titanium than those of Spring Creek Tuff. Intra-caldera pyroxenes vary considerably in sodium, but show a more limited range of titanium values.

1.3.4 – Age dating of rhyolites of Three Fingers caldera

Age dates obtained by $^{40}Ar/^{39}Ar$ method at OSU (Figure 30) show equivalent ages for the outflow tuff of Spring Creek (15.64 ± 0.09 Ma) and intra-caldera rhyolite (15.64 ± 0.08 Ma). These ages are slightly older than those previously reported for the tuff of Spring Creek (15.4 Ma) and the intra-caldera rhyolite (15.2 ± 0.5 Ma to

14.9±0.4 Ma) by Rytuba and VanderMeulen (1991) and Rytuba et al. (1989, 1991), using the K/Ar dating method. With the small margin of error observed, the maximum time permissible between eruption of the caldera forming tuff of Spring Creek and later intra-caldera rhyolites is about 0.17 million years, or 170 ky.

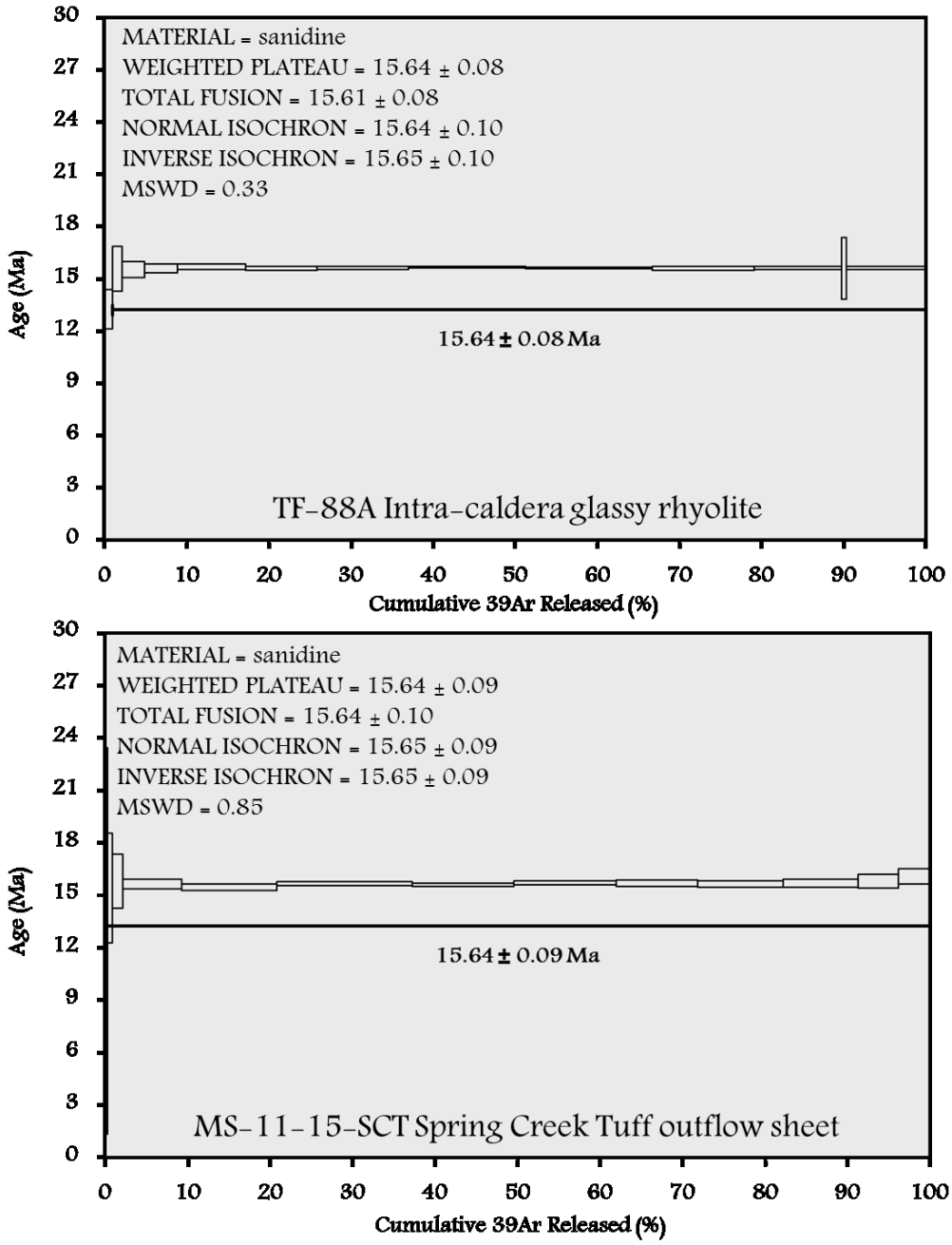

Figure 30: Age dates for outflow tuff of Spring Creek and intra-caldera rhyolites using $^{40}Ar/^{39}Ar$ dating method at the geochronology lab at Oregon State University.

1.4 - Discussion

1.4.1 - Discussion – Geochemistry

1.4.1.1 – The tuff of Spring Creek and intra-caldera rhyolite

Geochemical differences between the tuff of Spring Creek and intra-caldera rhyolites clearly exist. In terms of major elements, the intra-caldera units are high silica rhyolites, containing ~77 wt.% SiO_2 in glassy samples, compared to ~74 wt.% in dense glass of the outflow tuff of Spring Creek. In addition, the outflow sheets contain substantially more iron than intra-caldera units, ranging from ~3.0-3.6 wt.% FeO*, compared to ~0.4-2.0 wt.% FeO* for later erupted rhyolites. Corresponding depletions are observed in Ca, Al, and Ti in intra-caldera rhyolites in relation to the tuff of Spring Creek, providing abundant evidence to distinguish these units in terms of major elements. In addition, trace element evidence shows substantial differences between the two units in terms of barium and europium, and microprobe data shows consistent chemical differences between feldspars and pyroxenes within the tuff of Spring Creek, versus those of intra-caldera rhyolites. Taken together, these lines of evidence suggest the tuff of Spring Creek and later erupted rhyolites were produced from magmas with distinctly different compositions on the same line of descent.

The correlation between depletions in Ba and Eu (Figure 25) suggests a similar process may be responsible for the loss of these two trace elements in evolution from the tuff of Spring Creek composition to that of intra-caldera rhyolites. Outflow sheet samples show a slight enrichment in Ba relative to neighboring elements Rb and Th and a much less substantial negative peak for Eu than the intra-caldera rhyolites, whose average values for Eu/Eu* (0.208) are less than one third of those for the tuff of Spring Creek (0.632).

This distinctly different compositional range for Ba and Eu may be explained by removal of alkali feldspar. Few minerals present in rhyolitic magmas can readily incorporate both elements into their lattice structure as easily as alkali feldspar, with K_D values of 22.0 for Ba and 9.06 for Eu (Leeman and Phelps, 1981). Models show results of removal of alkali feldspar in 1% increments (Figure 31, shown by dots) during fractional crystallization from average values for the tuff of Spring Creek. The trend line clearly indicates loss of alkali feldspar from a magma similar to the source of the tuff of Spring Creek could result in Ba and Eu compositions similar to those of intra-caldera glasses, with 11-12% removal of alkali feldspar falling within the observed field for Eu and Ba concentrations.

Two key concerns with this model, however, are that the abundance of alkali feldspar in intra-caldera rhyolites is actually quite high, and that the composition of these feldspars is quite different. The Ba content of alkali feldspars in intra-caldera rhyolites is much lower than those of the tuff of Spring Creek, however, and indicate that the conditions of their formation were quite different. For the very crystal-rich porous devitrified sample TF-127, Ba values are considerably higher (388 ppm) than the average for glassy intra-caldera rhyolites (197 ppm), but much less than that of the tuff of Spring Creek (1810 ppm). With much lower Ba content of intra-caldera rhyolite feldspars, much higher rates of removal from a melt with the composition of bulk tuff of Spring Creek would be required to result in observed whole rock values.

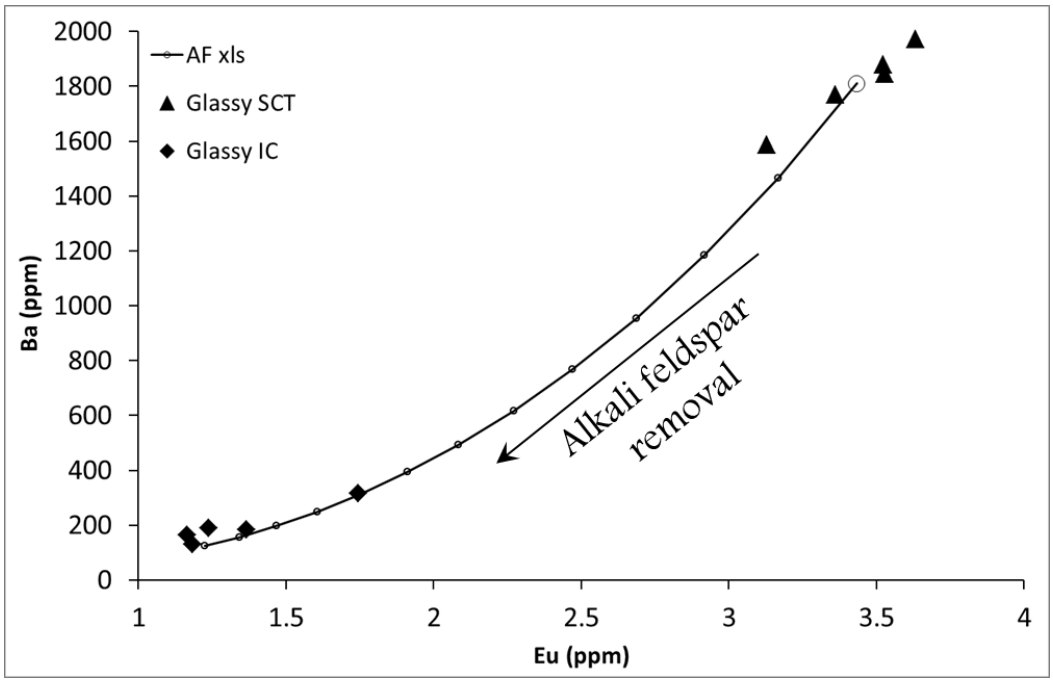

Figure 31: Removal of alkali feldspar from a magma reservoir producing Spring Creek tuff may result in depletions observed in Eu and Ba in erupted intra-caldera rhyolites. Each dot on the curve represents 1% removal of alkali feldspar via fractional crystallization, starting from average values for Spring Creek Tuff. Partition coefficients of Leeman and Phelps (1981).

EMP data shows alkali feldspar within the tuff of Spring Creek averages 1.25 wt.% BaO, compared to only 0.45 wt.% BaO in those of intra-caldera rhyolites. Partition coefficients for feldspars in silicic melts determined by Ren (2004) indicate that compatibility of Ba and Eu increase in sanidine with higher Ca and lower K content. This is the case with alkali feldspar of the tuff of Spring Creek being closer to albite in composition compared to those of later intra-caldera rhyolites, as shown in Figure 28. Whether the differences in Ba and Eu compositions can be attributed to removal by alkali feldspar or a combination of alkali and plagioclase feldspar is unclear, but

incorporation of significant Ba into early formed feldspars would likely lead to a depletion of source magmas for later eruptions of intra-caldera rhyolite, leaving later formed feldspar much less enriched.

1.4.1.2 – Mahogany Mountain caldera dikes and tuff of Leslie Gulch

Across the suite of elements for which we have geochemical data, rhyolite dikes within Mahogany Mountain caldera display a strong geochemical affinity with intra-caldera rhyolites of Three Fingers caldera. Meanwhile, tuff of Leslie Gulch shows a much stronger correlation to the tuff of Spring Creek, especially regarding the elements Ba and Eu. Europium anomalies for outflow tuff of Leslie Gulch plot in the same range as those of the tuff of Spring Creek, with two samples showing Eu/Eu* values of 0.617 and 0.573, compared to a range of 0.572-0.683 for the tuff of Spring Creek. One sample of intra-caldera Leslie Gulch Tuff (unpublished data, Streck 2012) displays a much lower Eu/Eu* value, at only 0.366, but this is still higher than later erupted intra-caldera rhyolites of Three Fingers and Mahogany Mountain calderas at Eu/Eu* of 0.199 and 0.197, respectively.

In terms of major elements, similarities between intra-caldera rhyolites and rhyolite dikes within Mahogany Mountain caldera are most apparent in SiO_2, FeO*, and

TiO_2. Trace element behavior in these units shows considerable correlation, as does the behavior of earlier erupted caldera forming tuffs and older McIntyre Ridge Rhyolite flows. When normalized against the composition of glassy intra-caldera rhyolite, these distinctions become even more obvious (Figure 32), with average values of Mahogany Mountain dikes producing a nearly flat pattern. Meanwhile, this comparison clearly reveals affinities between the tuff of Spring Creek, tuff of Leslie Gulch, and older McIntyre Ridge Rhyolites most noticeable in Ba, Eu, and Ti.

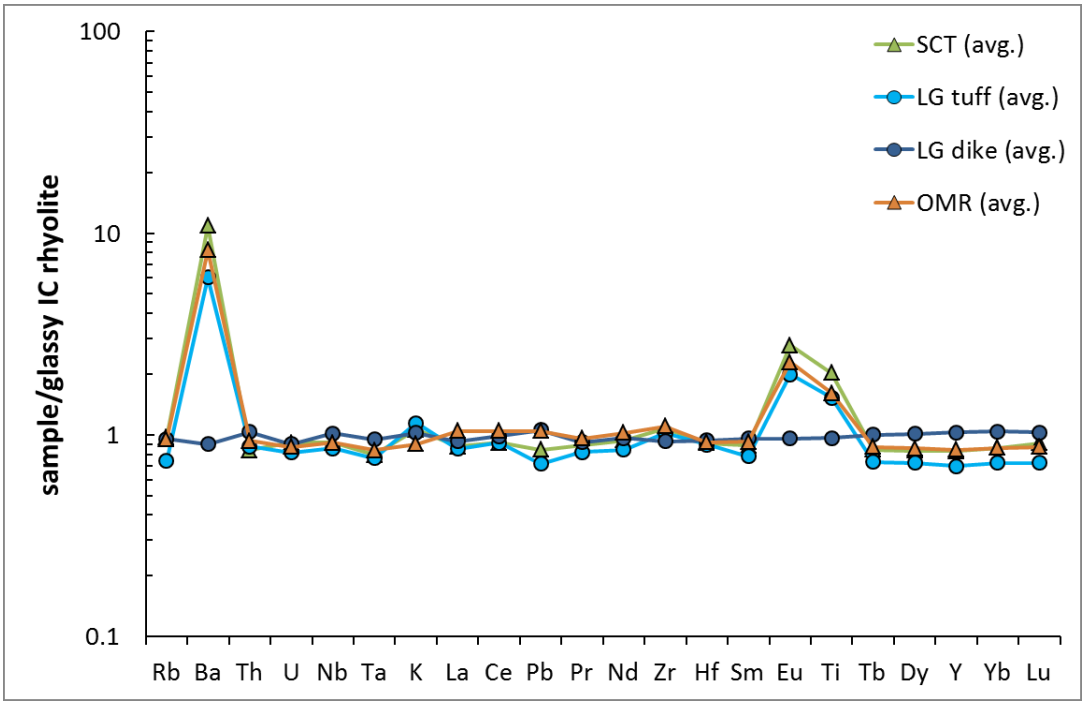

Figure 32: Trace elements normalized to average values for intra-caldera glass show striking similarity of dikes within Mahogany Mountain Caldera. Older McIntyre Ridge flows appear nearly identical to trace element compositions of Leslie Gulch and Spring Creek Tuff units.

The geochemical signatures of units related to the Three Fingers and Mahogany Mountain calderas appear to be linked temporally, and suggest a similar magma source for eruptions of both systems. Older eruptions of McIntyre Ridge Rhyolites appear to share geochemical affinities with the early erupted tuff of Spring Creek and the tuff of Leslie Gulch (Figure 32), while younger McIntyre Rhyolites are more similar to later erupted intra-caldera rhyolites of both Mahogany Mountain and Three Fingers calderas. When normalized to glassy intra-caldera rhyolites of Three Fingers caldera, early erupted units display elevated contents of Ba, Eu, and Ti. In comparison, the later

erupted rhyolite dikes intruding through tuff of Leslie Gulch do not show these differences, and appear nearly identical to later erupted rhyolites within Three Fingers caldera. Thus, the two caldera systems appear to have shared a common magma source which underwent compositional changes between eruptive periods.

1.4.1.3 – Devitrification and porosity

The effects of devitrification have been demonstrated by comparisons within compositional groups, and appear to be most apparent in differences in concentrations of P, Mn, Mg, and Zn. Major elements Na and Mg are immobile during the crystallization of high-silica melts, but may be mobilized by later alteration. In addition, Cl, F, Sr, Y, and the REE. Mg and Sr are also shown to be mobilized and redistributed by groundwater (Weaver et al., 1990). Increasing porosity appears to correlate with enrichments in Sr, possibly due to increased weathering induced by larger surface area for diffusion and accumulation. Dramatic increases (up to 80%) in Sr content have been cited for pumiceous rocks related to leaching of trachytic glass in the near surface environment (Mungall and Martin, 1993). Results from the same study indicate losses of 15-50% of Fe, Ca, Na, Mn, and Eu, with highly variable depletions or enrichments in Mg and P. Clearly, water has played an important role in the resulting textural and

geochemical makeup of intra-caldera rhyolites, as the intrusion of superheated water aided diffusion of elements and may explain the variability observed between facies.

1.4.2 – Field Relationships within Three Fingers Caldera

1.4.2.1 – Geologic History - Timeline

Eruption of the outflow tuff of Spring Creek resulted in subsidence of fault blocks within Three Fingers caldera at 15.64 ± 0.08 Ma. The majority of local normal faults fall in accord with regional scale faulting within the Oregon-Idaho graben, with few large offset faults and a greater number of small offset faults striking N to NNW through the study area. Many of these fractures served as magmatic conduits for eruption of intra-caldera rhyolites as extension continued throughout the region following voluminous caldera-forming eruptions at Three Fingers and Mahogany Mountain calderas. Age date analyses for dense glassy intra-caldera rhyolite gave an equivalent age of 15.64 ± 0.08 Ma, but field relationships indicate these units were not coeval, and were tapped by different magma reservoirs.

Exposures of tuffaceous sediments up to ~20 meters thick in some locations within the study area indicate a period of lacustrine sedimentation within the caldera moat after the collapse of several fault blocks. Erosional products of loosely consolidated

outflow tuff of Leslie Gulch and intra-caldera tuff of Spring Creek settled to the caldera lake bottom, forming finely laminated deposits of fine ashy material. At this point it is unclear whether this took place in a well formed, circular basin as idealized in caldera settings, or rather as a series of distinct sub-basins in a horst and graben extensional regime.

Fine-grained tuffaceous sediments most commonly occur directly beneath intra-caldera rhyolites, but are also witnessed above. Sediments exposed beneath intra-caldera rhyolites, and as clasts within Polymict breccias serve as excellent markers, signifying a period of erosion between caldera collapse and eruption of later rhyolites. Based on the equivalent age dates for the tuff of Spring Creek and intra-caldera rhyolites, this period of sedimentation could have lasted no more than ~0.17 My, and likely considerably less before these sediments were covered by rhyolite domes, flows, and polymict breccias produced from intra-caldera vents.

Laminated sediments also record angular displacements due to later faulting and intrusive volcanic activity. The two forces acting to modify the original horizontality of these beds during the middle-Miocene were likely: 1) continued normal faulting and rotation of slump blocks, which is largely down to the west within the study area, and

2) emergence of domes and plugs from beneath, pushing overlying units upward and outward as dome growth proceeded.

1.4.2.2 – Intra-caldera rhyolites

In the previous mapping of the Three Fingers caldera (Vander Meulen et al., 1989), the porous and all glassy intra-caldera rhyolites were interpreted as an intra-caldera facies of the tuff of Spring Creek, and subdivided into two groups: the 'intracaldera member' (Ttsi) and the "basalt bomb member" (Ttsb), containing clusters of mafic "bombs". Detailed examination of these rocks reveals an absence of vitroclastic textures indicative of a pyroclastic origin, indicating these are actually porous rhyolite lavas. In addition, the mapping of intra-caldera rhyolite (Trp) was typically limited to dense devitrified facies forming high standing features, but no connection was made to porous devitrified rhyolites. These porous rhyolites make up the majority of the geographic distribution of intra-caldera rhyolites, thus the distribution of intra-caldera tuff of Spring Creek appears nonexistent, though mapped extensively by Vander Meulen et al. (1989).

The distribution of dense devitrified rhyolite in the study area agrees with the development of magmatic conduits with E-W extension along normal faults. These

dense devitrified units are interpreted as either upheaved plugs or the interior of volcanic domes that maintained high temperature for an extended time, compared to other rhyolite facies. Flow banding is common in these high-standing features, concordant with their vertical foliation, and in some locations contacts banded glassy rhyolites, cooled quickly against the country rock at the margins of the conduit. This situation occurs at the base of Three Fingers Rock, where ~3 meters of dense glass adjacent to the devitrified plug shows variable degrees of devitrification, illustrating cooling of rising magma against the walls of the eruptive conduit. Other locations, including downslope to the southwest of Three Fingers Rock, dense glass sheets cover the land surface at low angles from horizontal, suggesting they are likely basal vitrophyre of lava flows following the paleo-land surface.

Flows of dense devitrified rhyolite are also abundant within the caldera, but are relatively discontinuous. Outcrops of parallel banded rhyolites generally form high standing ridges or circular plateaus above banded, glassy contacts. Erosional remnants of these flows are widespread as extended talus slopes of platy resistant rhyolite filling small gullies and stream channels. The dissection of rhyolite lava flows likely occurred as less resistant underlying units were eroded from beneath by fluvial processes. The

position of these flows in the present day landscape is typically limited to locations where underlying rocks are also fairly resistant, likely above feeder dikes and dense, lithified sediments and clastic debris.

Perhaps the key reinterpretation of this mapping effort is the much larger aerial extent of intra-caldera rhyolites compared to previous field studies within Three Fingers Caldera. This interpretation is based upon recognition of porous devitrified rhyolite that was mapped previously as intra-caldera tuff of Spring Creek. The appearance of porous devitrified rhyolite in the field is strikingly different to that of dense and glassy facies of the same unit. Under magnification, the texture is very finely vesiculated, giving a bright white color to unweathered surfaces, comparable to the effect of porosity in ash tuff.

Degassing of volatiles leads to high porosity of lavas approaching the surface as pressure is reduced. Continued oversteepening of dome structures and unloading of carapace material would induce sudden changes in pressure within the growing dome, inducing fine vesiculation of highly viscous rhyolite magmas. Gonde et al. (2011) state that a higher bubble number density in rhyolites results from more rapid decompression, but that very rapid (<10 min) decompression times result in higher

bubble coalescence and fragmentation. In some cases, porous intra-caldera rhyolites exhibit bubble coalescence and elongation, but the majority of samples contain unconnected, round vesicles, suggesting high viscosity and/or rapid decompression.

1.4.2.3 – Emplacement model for intra-caldera rhyolites

Most likely, a combination of coulees, low-lying cryptodomes, and peleean dome structures were erupted after the period of sedimentation within the caldera. The relationship between high standing, devitrified central columns and associated porous and vitric rhyolites suggests emergence of lavas into dome structures that often overrode the land surface for considerable distances.

The lithology and thickness of monomict rhyolite breccias suggest that several domes or coulees became oversteepened at their margins, resulting in the collapse of the brittle, glassy carapace (Branney et al., 2008). In the resulting clastic debris flow, materials of differing porosities intermixed to produce glassy rhyolite autobreccias near the margins of growing domes. The heat retained within these deposits resulted in partial fusion of vitric debris and vitric blocks, with variable porosity of entrained blocks likely dependent on their stratigraphic position within the dome exterior. The

banded appearance of many breccia deposits suggests episodic unloading of dome carapace glass with continued dome growth.

Episodic behavior has been recognized in the growth of modern and historic lava domes (Barmin et al.,2002; Hale, 2008). This behavior is thought to be governed by magma chamber dynamics, such as volume of the chamber, viscosity, and proportion of dissolved volatiles within the magma. Barmin et al. (2002) argue that magmas within a growing dome system can exist in one of two states, either ascending quickly enough to prevent the growth of crystals, or slowly enough for significant crystallization during ascent and degassing. Exposures of banded glassy rhyolites at the contact with dense devitrified rhyolites may represent further evidence of this episodic behavior, with microlite-rich, lighter colored bands alternating with darker, microlite-poor bands.

The eruption of low-lying domes in the shallow subsurface may be expressed in the modern topography as low, rounded hills, whose exterior is nearly entirely composed of dense glass. These broad features lack a central devitrified spine feature, since their inner structures have not yet been exposed. These features are observed at lower elevations than rhyolite lava flows that generally form topographic highs in the area. The upheaval of overlying units, such as the tuffaceous siltstone and intracaldera

ash-flow of Spring Creek may indicate intrusion of cryptodomes or peleean domes, with eventual surface expression of the plutonic structure as erosion of overlying units . In the case of cryptodomes, interaction of rhyolite lavas with overlying wet sediments likely resulted in explosion breccias, peperites, and lithification of sediments.

1.5 - Conclusions

Eruption of the tuff of Spring Creek at 15.64±0.08 Ma, in addition to extensional tectonics within the Oregon-Idaho graben resulted in collapse of Three Fingers caldera along ring fractures. This resulted in a complex intra-caldera topography of horst and graben features, generally oriented N-S, creating distinct sub-basins within the caldera. Volcaniclastic sediments from the tuff of Spring Creek, tuff of Leslie Gulch, and other nearby volcanic centers were reworked through fluviatile and lacustrine processes within these basins, creating up to 40 meter thick sequences of coarse and fine tuffaceous sediments. Magmatism was renewed shortly thereafter with continued extension in the region, resulting in eruption along several N-S trending fault structures within the study area and within the core of the Mahogany Mountain caldera complex.

Later erupted intra-caldera rhyolites were largely emplaced as domes, coulees, and rhyolite flows of variable thickness and volume, resulting in several distinct facies. Many exposures of glassy rhyolite breccias likely represent collapse of domes, oversteepened by continued growth, resulting in an avalanche of dense glass blocks from the quenched dome exterior and clastic debris plucked from the ground surface, entrained in a matrix of fractured glass. Thicker deposits were most likely emplaced within graben structures adjacent to fractures serving as magmatic conduits for these eruptions.

Outcrops of glassy intra-caldera rhyolite resembling breccia deposits, here termed 'pseudo-breccias', result from later alteration of volcanic glass by intrusion of fluids. The branching pattern observed within pseudo-breccia outcrops results in a wide variety of appearances, dependent on the proliferation of fine veinlets. Larger vein structures near the bottom of intra-caldera glass deposits continue to branch upsection, dissecting the originally dense glassy rhyolite, leading to nearly complete alteration of the glass within these rocks.

Clastic debris, including mafic clasts and fragments of tuffaceous siltstone were likely entrained during magma ascent through narrow conduits along fault zones, in

addition to those plucked from the land surface during overland transport. The variability in chemistry and physical appearance of mafic clasts entrained suggests that these were not the product of one distinct lava flow, but likely represent distinct source materials, possibly resulting from a stratified magma chamber beneath the caldera or from extra-basinal sources.

Hydrothermal alteration is evident in nearly all intra-caldera units, but varies widely by location, with evidence of secondary mineralization along fractures through tuffaceous sediments, porous devitrified rhyolite, glassy rhyolites, and basaltic andesite lava flows. These fractures are often filled with quartz or calcite, and create resistant ledges within outcrops. In addition, devitrified veinlets in pseudo-breccias of intra-caldera rhyolite indicate intrusion and brecciation of volcanic glass by superheated fluids. Circulation of hydrothermal fluids within fractures in mafic to intermediate lava flows is most likely responsible for the variable degree of weathering and oxidized rind formation observed in entrained mafic clasts within intra-caldera rhyolite units.

References

Barmin, A., Melnik, O., Sparks, R.S.J., 2002, Periodic behavior in lava dome eruptions: Earth and Planetary Science Letters, v. 199, p. 173–184.

Boler, P.M., 1979, Aeromagnetic measurements, magnetic source depths, and the Curie point isotherm in the Vale–Owyhee, Oregon, geothermal area: Corvallis, Oregon, Oregon State University, M.S. thesis, 104 p.

Branney, M.J., Bonnichsen, B., Andrews, G.D.M., Ellis, B., Barry, T.L., McCurry, M., 2008, 'Snake River (SR)–type' volcanism at the Yellowstone hotspot track: distinctive products from unusual, high–temperature silicic super–eruptions: Bulletin of Volcanology, v.70, p. 293–314.

Brueseke, M.E., Heizler, M.T., Hart, W.K., and Mertzman, S.A., 2007, Distribution and geochronology of the Oregon Plateau (U.S.A.) flood basalt volcanism: The Steens Basalt revisited: Journal of Volcanology and Geothermal Research, v. 161, p. 187–214.

Camp, V.E., 1995, Mid–Miocene propagation of the Yellowstone mantle plume head beneath the Columbia River basalt source region: Geology, v.23, no. 5, p. 15,255–15,271.

Camp, V.E., Ross, M.E., and Hanson, W.E., 2003, Genesis of flood basalts and Basin and Range volcanic rocks from Steens Mountain to the Malheur River Gorge, Oregon: Geological Society of America Bulletin, v. 115, n. 1, p. 105–128.

Camp, V.E., Ross, M.E., 2004, Mantle dynamics and genesis of mafic magmatism in the intermontane Pacific Northwest: Journal of Geophysical Research, v.109, n.B8.

Carlson, R.W., and Hart,W.K., 1987, Crustal genesis on the Oregon Plateau: Journal of Geophysical Research, v. 92, p. 6191–6206.

Cummings, M.L., Evans, J.G., Ferns, M.L., and Lees, K.R., 2000, Stratigraphic and structural evolution of the middle Miocene synvolcanic Oregon–Idaho graben: GSA Bulletin, v.112, p. 668–682.

Erickson, M.S., Malcolm, J.D., Hoffman, J.D., and King, H.D., 1986, Analytical results and sample locality maps of stream–sediment and heavy–mineral–concentrate samples from the Honeycombs and the Owyhee Canyon: Bureau of Land Management Wilderness Study Areas open file report 86–628.

Evans, J.G., 1992, Geologic map of the Dooley Mountain Quadrangle, Baker County,Oregon: U.S. Geological Survey GQ–1694, scale 1:24000.

Ferns, M.L., and Cummings, M.L., 1992, Geology and mineral resources map of The Elbow Quadrangle, Malheur County, Oregon: Oregon Department of Geology and Mineral Industries Geological Map Series GMS–74, scale1:24 000.

Ferns, M.L., and Cummings, M.L., 1996, Geologic Resources of the Vale and Mahogany Mountain 30X60 Minute Quadrangles: State of Oregon Department of Geologic and Mineral Industries open file report 0–94–10.

Ferns, M.L., 1997, Field trip guide to the eastern margin of the Oregon–Idaho graben and the middle Miocene calderas of the Lake Owyhee volcanic field: Oregon Geology, v.59, no.1, p. 9–19.

Fisher, R.V., and Schminke, H.U., 1984, *Pyroclastic Rocks*: Springer–Verlag, 472 p.

Gonde, C., Martel, C., Pichavant, M., and Bureau, H., 2011, In situ bubble vesiculation in silicic magmas: American Mineralogist, v. 96, p. 111–124.

Hale, A.J., 2008, Lava dome growth and evolution with an independently deformable talus: Geophysical Journal International, v. 174, p. 391–417.

Henry, C.D., Castor, S.B., McIntosh, W.C., Heizler, M.T., Cuney, M., and Chemillac, R., 2006, Timing of oldest Steens basalt magmatism from precise dating of silicic volcanic rocks, McDermitt Caldera and northwest Nevada Volcanic Field: Eos Trans. AGU, v. 87, Fall meeting supplementary abstract V43D-12.

Hooper, P.R., Binger, G.B., and Lees, K.R., 2002, Ages of the Steens and Columbia River flood basalts and their relationship to extension-related calc-alkalic volcanism in eastern Oregon: Geological Society of America Bulletin, v. 114, n. 1, p. 43-50.

Johnson, D.M., Hooper, P.R., and Conrey, R.M., 1999, XRF Analysis of Rocks and Minerals for Major and Trace Elements on a Single Low Dilution Li-tetraborate Fused Bead: Advances in X-ray Analysis, v. 41, p. 843-867.

Jordan, B.T., Grunder, A.L., Duncan, R.A., and Deino, A.L., 2004, Geochronology of age-progressive volcanism of the High Lava Plains: Implications for the plume interpretation of Yellowstone: Journal of Geophysical Research, v.109, n. B10.

Kittleman, L.R., Green, A.R., Hagood, A.R., Johnson, A.M., McMurray, J.M., Russel, R.A., and Weeden, D.A., 1965, Cenozoic stratigraphy of the Owyhee Region, southeastern Oregon: University of Oregon Museum of Natural History Bulletin 1, 45 p.

Kittleman, L.R., Green, A.R., Hagood, A.R., Johnson, A.M., McMurray, J.M., Russel, R.A., and Weeden, D.A., 1967, Geologic map of the Owyhee Region, Malheur County, Oregon: University of Oregon Museum of Natural History Bulletin 8, scale 1:250,000.

Leeman, W. and Phelps, D., 1981, Partitioning of rare earths and other trace elements between sanidine and coexisting volcanic glass: Journal of Geophysical Research, v.86, n.B11.

Leeman,W.P., Oldow, J.S., and Hart,W.K., 1992, Lithosphere scale thrusting in the western U.S. Cordillera as constrained by Sr and Nd isotopic transitions in Neogene volcanic rocks: Geology, v. 20, p. 63–66.

Lees, K.R., 1994, Magmatic and tectonic changes through time in the Neogene volcanic rocks of the Vale area, Oregon, northwestern USA [Ph.D. dissert.]: Milton Keynes, UK, Open University, 284 p.

Macdonald, Ray, 1974, Nomenclature and petrochemistry of the peralkaline over saturated extrusive rocks: Bulletin of Volcanology, v. 38, p. 498-516.

Mahood, G.A., 1981, A summary of the geology and petrology of the Sierra La Primavera, Jalisco, Mexico: Journal of Geophysical Research, v. 86, no. fill, p. 10,137-10,152.

Mahood, G.A., and Hildreth, Wes, 1983, Large partition coefficients for trace elements in high-silica rhyolites: Geochimica Cosmochimca Acta, v. 47, p. 11-30.

Mungall, J.E., and Martin, R.F., Severe leaching of trachytic glass without devitrification, Terceira, Azores: Geochimica et Cosmochimica Acta, v.58, p. 75-83.

Peccerillo, A., Barberio, M.R., Yirgu, G., Ayalew, D., Barbieri, M., Wu, T.W., 2003, Relationships between Mafic and Peralkaline Silicic Magmatism in Continental Rift Settings: a Petrological, Geochemical and Isotopic Study of the Gedemsa Volcano, Central Ethiopian Rift: Journal of Petrology, v. 44, no. 11, p. 2003-2032.

Ren, M., 2004, Partitioning of Sr, Ba, Rb, Y, and LREE between alkali feldspar and peraluminous silicic magma: American Mineralogist, v. 89, p. 1290-1303.

Rytuba, J.J. and McKee, E.H., 1984, Peralkaline ash flow tuffs and calderas of the McDermitt Volcanic Field; southeast Oregon and north central Nevada: Journal of Geophysical Research, v. 89, no. B10, p. 8616-8628.

Rytuba, J.J., Vander Meulen, D.B., Plouff, D., and Minor, S.A.,1985, Geology of the Mahogany Mountain caldera, Oregon [abs.]: Geological Society of America Abstracts with Programs, v. 17, no. 4, p. 70.

Rytuba, J.J., 1989, Volcanism, extensional tectonics, and epithermal mineralization in the northern Basin and Range province, California, Nevada, Oregon, and Idaho, *in* Schindler, K.S., ed., USGS research on mineral resources – program and abstracts: Fifth Annual V.E. McKelvey Forum on Mineral and Energy Resources, U.S. Geological Survey Circular 1035, p. 59–61.

Rytuba, J.J., Vander Meulen, D.B., and Barlock, V.E., 1991, Tectonic and stratigraphic controls on epithermal precious metal mineralization in the northern part of the Basin and Range, Oregon, Idaho, and Nevada, *in* Buffa, R.H., and Coyner, A.R., eds., Geology and ore deposits of the Great Basin field trip guidebook compendium: Geological Society of Nevada, v. 2, p. 633–644.

Shoemaker, K.A., The Tectomagmatic Evolution of the Late Cenozoic Owyhee Plateau, Northwestern United States [Ph.D. dissertation]: Oxford, Ohio, Miami University, 276 p.

Sun, S.S., and McDonough, W.F., 1989, Chemical and isotopic systematics of oceanic basalts: implications for mantle composition and processes: Geological Society Special Publication, n. 42, p. 313–345.

Vander Meulen, D.B., Rytuba, J.J., Minor, S.A., and Harwood, C.S., 1989, Preliminary Geologic map of the Three Fingers Rock quadrangle, Malheur County, Oregon: U.S. Geological Survey Open-File Report 89-344.

Vander Meulen, D.B., Rytuba, JJ. Vercoutere, T.L., and Minor, S.A., 1987d, Geologic map of the Rooster Comb 7.5' quadrangle, Malheur County, Oregon: U.S. Geological Survey Miscellaneous Field Studies Map MF-1902D, scale 1:24,000.

Watkins, N.D., and Baksi, A.K., 1974, Magnetostratigraphy and oroclinal folding of the Columbia River, Steens, and Owyhee basalts in Oregon, Washington, and Idaho: American Journal of Science, v. 274, p. 148–189.

Weaver, S.D., Gibson, I.L., Houghton, B.F., and Wilson, C.J.N., Mobility of rare earth and other elements during crystallization of peralkaline silicic lavas: Journal of Volcanology, v. 43, p, 57–70.

Appendix 1A – Geologic Maps

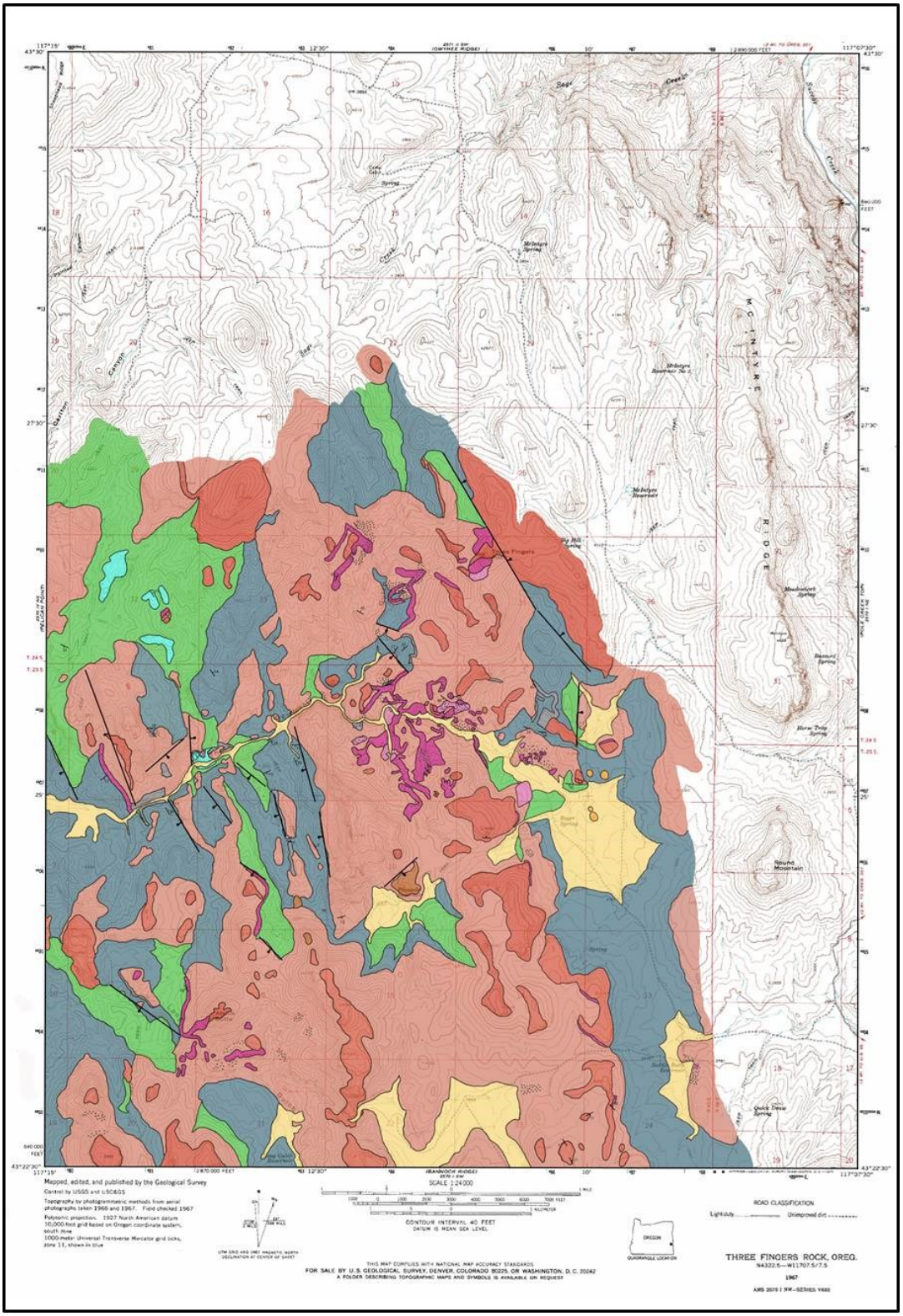

Geologic map based on field evidence during this study.

Map key for units of Three Fingers Caldera

Quaternary colluvium– Sedimentary deposits composed primarily of ash, mud, and fine glass. Poorly sorted, with clasts of devitrified rhyolite, dense glass, and mafic clasts in steep topography, grading to well sorted fine ash and muds where topography is muted.

DD PD DG PG **Intra–caldera rhyolite**– Rhyolite domes, plugs, and flows erupted within Three Fingers Caldera, subsequent to collapse. Occurs in four distinct facies, including dense devitrified, porous devitrified, dense glass, and porous glass. Contains 10–25% blocky sanidine up to 8 mm in diameter, 5–10 %quartz of 1–2 mm, and minor clinopyroxene. Commonly hosts mafic clasts of 2–30 cm in diameter.

Polymict Breccia– Matrix supported breccias incorporating underlying tuffaceous sediments and occasional mafic clasts within porous devitrified rhyolite. Typically weak lithology and thickness of only 1–4 feet limits exposures to locations where protected by overlying rhyolite. Clast size ranges from less than 1 cm to greater than 25 cm.

Tuffaceous sediments– Planar bedded lacustrine deposits white , pink, or green in color composed of fine ash and typically aphyric. Forms outcrops up to ~40 feet high in the central portion of the study area, and is quite resistant where silicified. Laminations range from millimeter scale to 2 cm, with occasional bands of fine crystalline deposits and discoloration.

Volcaniclastic sandstone– Limited exposures in the western part of the study area show white to pink rocks as solitary outcrops of no more than 10 feet in height. Groundmass composed of fine ash and lithic fragments lacking primary texture, and 30–35% sub–millimeter sized fractured crystals of quartz and feldspar that are typically sub–angular to rounded.

Pumice–bearing ash flow tuff– Tan to light green ash flow tuff, with round to slightly oblate pumice generally less than 1 cm. Often contains void spaces up to 40 cm due to differential weathering. Contains minor amounts of sub–millimeter grey to red lithic fragments. Less than 15% phenocrysts, with 1–2 mm sanidine and quartz.

Basalt flow– Dark grey on fresh surfaces, forming well–defined columns 7–10 cm in diameter. Top of exposure shows crude flow banding of 1–2 mm in thickness. Typically aphyric, with groundmass dominated by sub–millimeter plagioclase, oxides, and minor olivine.

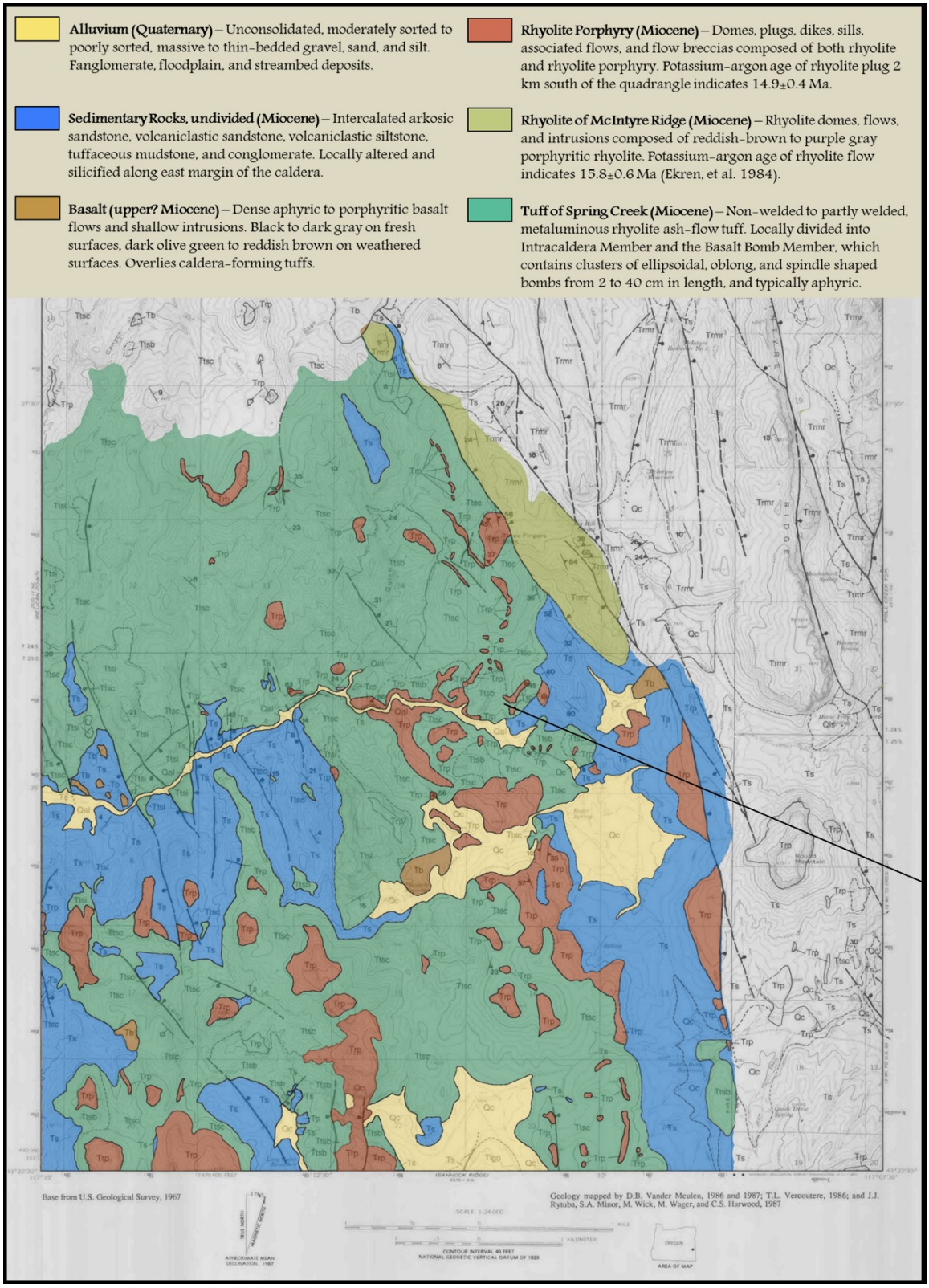

Geologic map of Vander Meulen , et al. (1989).

Appendix 1B – Electron Microprobe (EMP) data

Sample	TF-153H	TF-153H	TF-153H	TF-153H	TF-153H	TF-153H	TF-153H	TF-153H	TF-157A
Phenocryst	Alkali Feldspar								
Dataset/Point	1 / 1 .	1 / 2 .	1 / 3 .	2 / 1 .	2 / 2 .	3 / 1 .	3 / 2 .	3 / 3 .	1 / 4 .
X	3002	3296	2918	12258	11893	23154	22488	23570	-19425
Y	-35244	-35513	-35254	-40088	-40030	-10250	-10863	-11535	-33306
SiO_2	67.088	66.762	67.011	67.114	67.141	66.741	65.482	66.918	66.407
TiO_2	0.009	n.d.	0.035	0.024	0.057	0.035	0.033	0.023	n.d.
Al_2O_3	19.425	19.344	19.519	19.692	19.677	19.753	20.149	19.774	19.385
FeO	0.162	0.202	0.215	0.202	0.196	0.194	0.200	0.159	0.166
MnO	0.042	0.041	n.d.	0.037	0.009	n.d.	n.d.	n.d.	0.059
MgO	n.d.	n.d.	n.d.	0.001	n.d.	n.d.	n.d.	n.d.	n.d.
CaO	0.070	0.067	0.090	0.097	0.084	0.129	0.335	0.149	0.085
Na_2O	6.025	6.310	6.176	6.138	6.096	6.210	6.229	6.120	6.249
K_2O	7.560	7.421	7.601	7.377	7.351	7.187	6.594	7.210	7.242
P_2O_5	n.d.	n.d.	0.031	0.017	0.002	n.d.	n.d.	n.d.	0.003
BaO	0.028	0.015	0.074	0.072	0.078	0.179	0.882	0.287	0.038
Total	100.409	100.162	100.753	100.770	100.691	100.429	99.904	100.640	99.634

Sample	TF-157A	TF-157A	TF-157A	TF-157A	TF-157A	TF-157A	TF-157A	TF-157A	TF-157A
Phenocryst	Alkali Feldspar								
Dataset/Point	2 / 1 .	2 / 2 .	2 / 3 .	2 / 6 .	3 / 1 .	3 / 2 .	3 / 3 .	3 / 4 .	3 / 5 .
X	-18907	-19062	-19352	-17945	-11810	-12117	-12484	-11541	-11727
Y	-33433	-33150	-33201	-34364	-34024	-34165	-33228	-33943	-33712
SiO_2	65.774	65.625	66.750	66.676	66.671	66.971	65.758	66.650	66.095
TiO_2	0.024	0.039	0.020	0.006	n.d.	0.016	n.d.	0.008	0.030
Al_2O_3	19.160	19.200	19.361	19.313	19.309	19.456	19.498	19.366	19.575
FeO	0.172	0.212	0.212	0.214	0.193	0.262	0.171	0.206	0.136
MnO	n.d.	n.d.	0.005	0.008	0.065	0.036	n.d.	n.d.	n.d.
MgO	n.d.	n.d.	n.d.	0.008	n.d.	0.003	n.d.	n.d.	0.004
CaO	0.080	0.088	0.052	0.090	0.111	0.082	0.116	0.089	0.086
Na_2O	6.147	6.199	5.982	6.284	6.097	6.019	6.082	5.976	6.360
K_2O	7.452	7.421	7.560	7.536	7.470	7.422	7.530	7.605	7.457
P_2O_5	n.d.	0.007	n.d.	n.d.	n.d.	0.006	0.007	n.d.	0.011
BaO	0.112	0.053	0.052	0.030	0.061	0.058	0.061	0.049	0.063
Total	98.920	98.845	99.993	100.163	99.977	100.329	99.222	99.948	99.816

Sample	TF-157A	TF-157A	TF-157A	TF-157A	TF-157A	TF-157A	TF-157A	TF-157A	TF-152EH
Phenocryst	Alkali Feldspar								
Dataset/Point	5 / 1 .	5 / 2 .	5 / 3 .	5 / 4 .	6 / 1 .	6 / 2 .	6 / 3 .	6 / 5 .	1 / 1 .
X	-10355	-11097	-12778	-13158	-15785	-15635	-15807	-16572	9068
Y	-25151	-25482	-26392	-25976	-24288	-22315	-22155	-20763	-17437
SiO_2	66.859	65.861	66.559	66.401	65.867	66.779	66.659	65.813	66.591
TiO_2	0.041	n.d.	0.042	0.039	0.042	0.044	0.019	0.032	n.d.
Al_2O_3	19.687	19.488	19.670	19.940	19.665	19.463	19.631	19.360	19.620
FeO	0.178	0.244	0.218	0.187	0.191	0.207	0.200	0.202	0.203
MnO	0.048	n.d.	n.d.	0.016	0.012	0.033	0.031	0.018	0.024
MgO	0.004	n.d.	n.d.	0.002	n.d.	n.d.	n.d.	n.d.	n.d.
CaO	0.109	0.086	0.088	0.111	0.110	0.093	0.123	0.129	0.107
Na_2O	6.159	6.251	6.190	6.372	6.179	6.097	6.216	6.160	6.345
K_2O	7.322	7.290	7.416	7.325	7.453	7.558	7.483	7.357	7.490
P_2O_5	0.000	n.d.	n.d.	n.d.	0.014	n.d.	0.013	0.032	0.013
BaO	0.061	0.043	0.066	0.122	0.178	0.099	0.133	0.060	0.081
Total	100.467	99.263	100.249	100.515	99.712	100.373	100.509	99.161	100.474

Sample	TF-152EH	TF-152EH	TF-152EH	TF-152EH	TF-152EH	TF-152EH	TF-152EH	TF-152EH	TF-152EH
Phenocryst	Alkali Feldspar								
Dataset/Point	1 / 2 .	1 / 3 .	1 / 6 .	1 / 7 .	2 / 7 .	2 / 8 .	2 / 9 .	2 / 10 .	3 / 1 .
X	10129	11417	9039	9001	19568	19726	19853	19537	22395
Y	-16847	-17212	-17793	-17913	-11597	-11560	-11503	-11398	-16247
SiO_2	67.082	67.346	66.022	66.250	67.232	66.789	67.418	66.958	67.171
TiO_2	0.015	0.000	0.022	0.011	0.018	0.010	0.004	0.022	0.019
Al_2O_3	19.437	19.598	19.743	19.844	19.739	19.630	19.634	19.590	19.615
FeO	0.175	0.197	0.205	0.190	0.124	0.143	0.230	0.173	0.180
MnO	0.021	n.d.	0.038	0.010	0.046	0.038	0.012	0.021	0.022
MgO	n.d.	n.d.	n.d.	n.d.	n.d.	n.d.	n.d	n.d	0.003
CaO	0.096	0.117	0.128	0.077	0.105	0.104	0.106	0.094	0.134
Na_2O	6.095	6.202	6.088	6.230	6.196	6.206	6.376	6.049	6.092
K_2O	7.484	7.527	7.337	7.444	7.504	7.449	7.329	7.486	7.592
P_2O_5	n.d.	n.d.	n.d.	0.013	0.035	0.008	n.d.	n.d.	0.031
BaO	0.046	0.055	0.145	0.128	0.087	0.033	0.115	0.187	0.145
Total	100.450	101.042	99.729	100.196	101.087	100.410	101.223	100.579	101.004

Sample	TF-152EH	TF-152EH	TF-152EH	TF-152EH	TF-152EH	TF-152EH	TF-152EH	MS-11-17SCT	MS-11-17SCT
Phenocryst	Alkali Feldspar								
Dataset/Point	3 / 2 .	3 / 3 .	3 / 6 .	3 / 7 .	3 / 8 .	4 / 1 .	4 / 2 .	1 / 4 .	1 / 5 .
X	22921	21569	18774	18716	18745	7237	6580	-6195	-6129
Y	-16196	-16581	-19332	-18881	-19913	-31527	-31916	17530	17145
SiO_2	67.464	66.637	66.355	66.962	66.694	65.716	66.247	65.010	64.850
TiO_2	0.000	0.008	0.007	0.011	0.051	n.d.	0.006	n.d.	n.d.
Al_2O_3	19.617	19.975	19.645	19.721	19.408	19.383	19.269	19.811	19.971
FeO	0.179	0.186	0.186	0.184	0.199	0.209	0.181	0.167	0.200
MnO	0.019	n.d.	n.d.	n.d.	n.d.	n.d.	n.d.	n.d.	n.d.
MgO	0.000	n.d.	n.d.	n.d.	n.d.	0.002	n.d.	n.d.	n.d.
CaO	0.104	0.110	0.134	0.095	0.122	0.103	0.095	0.654	0.734
Na_2O	6.206	6.183	6.362	6.196	6.085	6.091	6.122	6.556	6.517
K_2O	7.510	7.526	7.418	7.446	7.479	7.534	7.219	5.473	5.383
P_2O_5	0.000	0.032	0.011	0.011	n.d.	0.001	0.010	0.011	0.012
BaO	0.076	0.042	0.116	0.103	0.076	0.094	0.138	1.209	1.161
Total	101.175	100.699	100.233	100.729	100.113	99.131	99.287	98.890	98.828

Sample	MS-11-17SCT	MS-11-17SCT	MS-11-17SCT	MS-11-17SCT	MS-11-17SCT	MS-11-17SCT	MS-11-17SCT	MS-11-17SCT	MS-11-17SCT
Phenocryst	Alkali Feldspar								
Dataset/Point	1 / 6 .	1 / 7 .	1 / 8 .	1 / 9 .	2 / 1 .	2 / 2 .	2 / 3 .	2 / 4 .	2 / 5 .
X	-6994	-7466	-7445	-8147	-8752	-9394	-8970	-8305	-7902
Y	17588	17953	18690	18729	34571	34639	35157	35588	35135
SiO_2	64.819	65.385	64.815	65.063	64.841	65.253	65.177	65.107	65.626
TiO_2	0.000	0.012	0.022	0.019	0.002	0.018	0.025	n.d.	0.035
Al_2O_3	20.447	20.432	20.104	19.919	20.278	19.926	20.190	20.085	19.842
FeO	0.167	0.170	0.241	0.185	0.177	0.184	0.195	0.197	0.173
MnO	n.d.	n.d	0.037	0.030	0.016	0.029	n.d.	0.012	0.026
MgO	n.d.	n.d.	n.d.	n.d.	n.d.	n.d.	0.003	0.002	n.d.
CaO	0.802	0.870	0.791	0.697	0.764	0.749	0.804	0.722	0.664
Na_2O	6.582	6.678	6.683	6.599	6.722	6.778	6.493	6.438	6.477
K_2O	5.278	5.280	5.184	5.434	5.232	5.317	5.164	5.393	5.520
P_2O_5	0.021	n.d.	0.001	n.d.	n.d.	n.d.	n.d.	n.d.	0.040
BaO	1.266	1.312	1.196	1.160	1.181	1.167	1.398	0.974	1.061
Total	99.380	100.139	99.075	99.105	99.211	99.421	99.449	98.931	99.465

Sample	MS-11-17SCT	MS-11-17SCT	MS-11-17SCT	MS-11-17SCT	MS-11-17SCT	MS-11-17SCT	MS-11-17SCT	MS-11-17SCT	MS-11-15SCT
Phenocryst	Alkali Feldspar								
Dataset/Point	3 / 10 .	3 / 11 .	4 / 1 .	4 / 2 .	4 / 3 .	4 / 7 .	4 / 8 .	4 / 9 .	1 / 1 .
X	-22824	-22402	-19459	-19332	-18900	-20441	-20597	-20263	17904
Y	36192	36320	31895	31996	32184	29952	29914	29498	37268
SiO_2	65.407	65.649	65.625	64.914	64.679	65.610	65.336	66.803	65.141
TiO_2	0.000	0.000	0.025	0.038	0.012	0.025	0.031	0.010	0.001
Al_2O_3	20.061	20.205	20.094	20.342	20.327	20.393	20.139	20.449	20.348
FeO	0.134	0.223	0.187	0.140	0.181	0.164	0.162	0.196	0.269
MnO	n.d	0.020	n.d.	0.015	n.d.	0.002	0.010	0.028	n.d
MgO	n.d.	n.d.	n.d.	n.d.	n.d.	n.d.	0.007	n.d.	0.003
CaO	0.659	0.780	0.656	0.672	0.708	0.779	0.813	0.659	0.701
Na_2O	6.571	6.720	6.538	6.821	6.777	6.639	6.444	6.858	6.605
K_2O	5.492	5.420	5.543	5.476	5.372	5.270	5.389	5.321	5.329
P_2O_5	n.d.	n.d.	n.d.	n.d.	n.d.	n.d.	0.009	n.d.	n.d
BaO	1.007	1.128	1.221	1.199	1.208	1.120	1.142	0.910	1.249
Total	99.331	100.146	99.887	99.618	99.265	100.002	99.482	101.233	99.644

Sample	MS-11-15SCT	MS-11-15SCT	MS-11-15SCT	MS-11-15SCT	MS-11-15SCT	MS-11-15SCT	MS-11-15SCT	MS-11-15SCT	MS-11-15SCT
Phenocryst	Alkali Feldspar								
Dataset/Point	1 / 2 .	1 / 3 .	3 / 1 .	3 / 2 .	3 / 3 .	6 / 1 .	6 / 2 .	6 / 6 .	8 / 1 .
X	18399	18167	9826	9119	8849	8948	9489	9791	11279
Y	37466	37108	32103	31727	31730	12233	11930	11206	6354
SiO_2	65.606	66.090	65.034	65.033	64.400	65.217	65.473	65.605	66.178
TiO_2	n.d.	n.d.	0.006	0.022	n.d.	0.041	0.012	0.013	0.014
Al_2O_3	20.598	20.550	20.929	20.275	20.828	20.462	20.851	20.744	20.306
FeO	0.197	0.232	0.256	0.199	0.241	0.182	0.263	0.215	0.247
MnO	n.d.	0.033	0.003	n.d	n.d.	0.025	n.d	n.d.	0.014
MgO	n.d.	n.d.	n.d.	n.d.	n.d.	n.d.	n.d.	n.d.	n.d.
CaO	0.825	0.744	0.998	0.659	1.116	0.801	0.831	0.664	0.667
Na_2O	6.966	6.917	6.866	6.781	7.164	6.409	6.802	6.961	6.573
K_2O	4.873	5.383	4.975	5.497	4.217	5.383	5.201	4.989	5.493
P_2O_5	n.d.	n.d.	n.d.	0.027	0.026	0.005	0.012	n.d.	0.036
BaO	1.016	0.961	1.488	1.256	1.268	1.656	1.221	1.163	1.305
Total	100.079	100.910	100.555	99.750	99.259	100.179	100.666	100.354	100.832

Sample	MS-11-15SCT	MS-11-15SCT	MS-11-15SCT	TF-153H	TF-153H	TF-153H	TF-157A	TF-157A	TF-157A
Phenocryst	Plagioclase			Hedenbergite					
DataSet/Point	4 / 1 .	4 / 2 .	4 / 3 .	1 / 1 .	1 / 3 .	6 / 2 .	4 / 1 .	4 / 2 .	8 / 1 .
X	6074	6009	5867	22073	21505	10491	-14119	-14057	-20155
Y	27567	27584	28013	-32234	-32536	-17866	-30288	-30325	-33081
SiO2	54.782	55.618	54.064	47.357	46.895	47.306	47.560	47.142	47.340
TiO2	0.063	0.130	0.094	0.255	0.316	0.315	0.308	0.275	0.282
Al2O3	27.828	27.608	28.526	0.163	0.223	0.202	0.186	0.217	0.200
FeO	1.108	0.982	0.991	29.958	30.281	29.982	29.864	29.915	30.695
MnO	n.d.	n.d.	0.009	0.768	0.890	0.829	0.781	0.860	0.860
MgO	0.063	0.037	0.058	0.127	0.074	0.127	0.373	0.134	0.103
CaO	10.670	9.894	11.224	19.495	19.285	18.552	19.221	19.383	19.105
Na2O	5.026	5.507	4.805	0.446	0.399	0.361	0.446	0.425	0.521
K2O	0.428	0.390	0.368	0.008	n.d.	0.002	n.d.	0.016	0.007
P2O5	0.035	0.001	0.049	0.014	n.d.	n.d.	0.029	n.d.	n.d.
BaO	0.073	0.065	0.027	0.009	n.d.	0.017	n.d.	0.003	0.021
Total	100.075	100.232	100.213	98.602	98.363	97.692	98.768	98.369	99.135

Sample	TF-157A	TF-157A	TF-157A	TF-152EH	TF-152EH	TF-152EH	TF-152EH	TF-152EH	TF-152EH
Phenocryst	Hedenbergite								
Dataset/Point	8 / 2 .	8 / 3 .	8 / 4 .	1 / 4 .	1 / 5 .	2 / 1 .	2 / 2 .	2 / 11 .	2 / 12 .
X	-20012	-20090	-20133	9379	9376	19384	19223	19626	19546
Y	-33037	-33200	-33232	-17723	-17792	-13048	-13005	-13359	-13477
SiO_2	47.085	47.235	47.400	47.397	47.721	47.543	47.265	47.619	47.392
TiO_2	0.242	0.312	0.271	0.269	0.271	0.287	0.260	0.260	0.263
Al_2O_3	0.141	0.170	0.193	0.234	0.222	0.200	0.227	0.210	0.190
FeO	30.761	30.134	29.894	29.565	29.969	30.599	30.488	30.126	30.071
MnO	0.751	0.833	0.774	0.765	0.815	0.860	0.773	0.715	0.775
MgO	0.098	0.095	0.147	0.122	0.135	0.122	0.092	0.099	0.110
CaO	19.029	19.291	19.570	19.194	19.261	19.734	19.459	19.681	19.702
Na_2O	0.451	0.564	0.523	0.467	0.381	0.398	0.394	0.403	0.503
K_2O	n.d.	n.d.	0.020	0.007	n.d.	n.d.	n.d.	0.004	n.d.
P_2O_5	0.006	0.012	0.017	n.d.	0.024	0.030	n.d.	n.d.	0.062
BaO	0.012	0.017	n.d.	0.009	n.d.	0.012	0.006	0.013	0.011
Total	98.575	98.662	98.809	98.029	98.799	99.785	98.963	99.128	99.079

Sample	TF-152EH	TF-152EH	TF-152EH	MS_11_17SCTa	MS-11-17SCT	MS-11-17SCT	MS-11-17SCT	MS-11-17SCT	MS-11-17SCT
Phenocryst	Hedenbergite								
Dataset/Point	4 / 3 .	4 / 4 .	4 / 5 .	1 / 1 .	1 / 2 .	1 / 3 .	2 / 6 .	2 / 7 .	2 / 8 .
X	7556	7785	7821	-6149	-6298	-6240	-9455	-9226	-9341
Y	-35785	-35554	-35655	17942	17830	17734	36418	36375	36177
SiO_2	47.112	47.570	47.050	46.851	47.054	47.226	47.325	46.800	46.945
TiO_2	0.260	0.277	0.308	0.585	0.470	0.466	0.552	0.476	0.538
Al_2O_3	0.247	0.166	0.233	0.388	0.366	0.399	0.334	0.376	0.391
FeO	30.572	30.575	30.256	29.981	30.061	30.370	30.121	30.233	30.177
MnO	0.767	0.974	0.871	1.017	0.850	0.970	0.867	0.777	0.940
MgO	0.076	0.103	0.079	0.150	0.156	0.164	0.138	0.121	0.130
CaO	18.814	19.079	19.210	19.260	19.315	19.206	19.026	19.429	19.211
Na_2O	0.456	0.505	0.522	0.298	0.312	0.306	0.350	0.235	0.348
K_2O	0.004	n.d.	0.012	0.002	0.005	0.003	n.d.	n.d.	0.007
P_2O_5	0.032	0.007	n.d.	0.017	n.d.	n.d.	n.d.	0.017	n.d.
BaO	n.d.	n.d.	0.021	0.042	0.013	n.d.	n.d.	n.d.	0.005
Total	98.340	99.255	98.563	98.591	98.601	99.110	98.713	98.465	98.692

Sample	MS-11-17SCT	MS-11-17SCT	MS-11-17SCT	MS-11-17SCT	MS-11-17SCT	MS-11-17SCT	MS-11-17SCT	MS-11-17SCT	MS-11-17SCT
Phenocryst	Hedenbergite								
Dataset/Point	2 / 9 .	2 / 10 .	3 / 1 .	3 / 2 .	3 / 3 .	3 / 4 .	3 / 5 .	3 / 6 .	3 / 8 .
X	-9588	-9346	-20321	-20431	-20334	-21381	-21145	-21248	-22931
Y	36381	36093	35209	35348	35448	35385	35253	35162	35075
SiO_2	46.935	46.891	47.215	46.857	47.001	46.791	46.741	47.008	47.337
TiO_2	0.521	0.559	0.562	0.532	0.513	0.649	0.657	0.585	0.466
Al_2O_3	0.347	0.393	0.434	0.414	0.473	0.488	0.549	0.497	0.365
FeO	29.915	30.205	31.167	30.836	30.561	30.374	30.627	29.872	30.429
MnO	0.992	0.924	0.960	0.904	0.928	1.025	1.004	1.137	0.962
MgO	0.129	0.143	0.145	0.144	0.153	0.118	0.118	0.120	0.115
CaO	19.114	19.279	19.263	19.324	19.278	19.339	19.192	19.319	19.320
Na_2O	0.314	0.270	0.220	0.264	0.221	0.266	0.292	0.271	0.302
K_2O	0.008	n.d.	n.d.	0.010	0.002	n.d.	n.d.	0.010	n.d.
P_2O_5	n.d.	0.033	n.d.	n.d.	0.049	0.047	n.d.	n.d.	0.010
BaO	0.023	n.d.	0.017	0.012	n.d.	n.d.	n.d.	0.034	0.024
Total	98.299	98.696	99.983	99.297	99.179	99.097	99.179	98.851	99.329

Electron microprobe data for phenocrysts within the tuff of Spring Creek and intra-caldera rhyolites.

Sample	MS-11-17SCT	MS-11-17SCT	MS-11-17SCT	MS-11-17SCT	MS-11-15SCT
Phenocryst	Hedenbergite				
Dataset/Point	3 / 9 .	3 / 12 .	4 / 4 .	4 / 5 .	2 / 1 .
X	-22866	-21005	-19386	-19386	12485
Y	35086	37567	32487	32487	34780
SiO_2	47.373	47.392	47.135	47.132	47.126
TiO_2	0.507	0.474	0.651	0.571	0.479
Al_2O_3	0.389	0.365	0.454	0.489	0.360
FeO	30.378	30.041	30.498	30.805	30.186
MnO	1.056	0.830	0.921	0.981	0.880
MgO	0.127	0.093	0.169	0.177	0.105
CaO	19.295	19.430	19.263	19.282	19.463
Na_2O	0.308	0.342	0.315	0.234	0.275
K_2O	0.021	n.d.	0.003	n.d.	n.d.
P_2O_5	0.007	0.003	0.023	0.039	0.020
BaO	0.011	n.d.	0.029	0.012	0.029
Total	99.470	98.970	99.461	99.720	98.925

Sample	MS-11-15SCT	MS-11-15SCT	MS-11-15SCT	MS-11-15SCT	MS-11-15SCT
Phenocryst	Hedenbergite				
Dataset/Point	2 / 2 .	2 / 3 .	6 / 3 .	8 / 2 .	8 / 3 .
X	12514	12616	10075	11701	11758
Y	34769	34793	12116	6054	6010
SiO_2	47.144	47.009	47.132	46.673	47.082
TiO_2	0.462	0.503	0.554	0.441	0.439
Al_2O_3	0.381	0.362	0.429	0.413	0.458
FeO	30.252	30.300	30.751	30.511	30.430
MnO	0.899	0.980	1.049	0.942	0.876
MgO	0.083	0.107	0.125	0.083	0.115
CaO	19.221	19.283	19.279	19.454	19.217
Na_2O	0.262	0.304	0.304	0.299	0.307
K_2O	n.d.	0.020	n.d.	n.d.	0.006
P_2O_5	0.016	0.037	0.019	0.043	0.005
BaO	0.035	n.d.	0.016	0.020	0.002
Total	98.755	98.906	99.658	98.879	98.936

Chapter 2 – Enrichment of REE in Mafic Clasts

2.1 - Introduction

The rare earth elements (REE) are a group of chemically similar elements also known as the lanthanides, and often include yttrium and scandium. For decades, these 17 elements were only of interest to scientists and engineers, but are steadily becoming more important in the manufacturing and design of high-tech devices. Many REE are crucial to emerging technologies such as renewable energy, high temperature semiconductors, and lasers (USGS, 2002). REE are found throughout continental crust, but commonly at concentrations less than 100 ppm for each element (Jackson, 1993) and ore-grade deposits are rare. Minable deposits of REE have only been discovered in a few geologic situations, one of which are peralkaline rhyolites.

For the last two decades, the increasing worldwide demand for REE has been met by a cheap supply of rare earths from China, which currently accounts for about 95 percent of the world's total production (USGS, 2010). Due to increasing development of high-tech industries within China, and concern over depleting their natural resources, the Chinese government has reduced export quotas on REE by 40 percent between 2009 and 2010 (Reuters, 2010). Traditional U.S. domestic reserves became less

economical beginning in the 1980's, leading to mine closure or decreased production (Figure 33). Mountain Pass, California, the last producing REE ore mine within the United States, ceased operation in 1998 but owner Molycorp has renewed operations as of August 2012 (Business Wire, 2012).

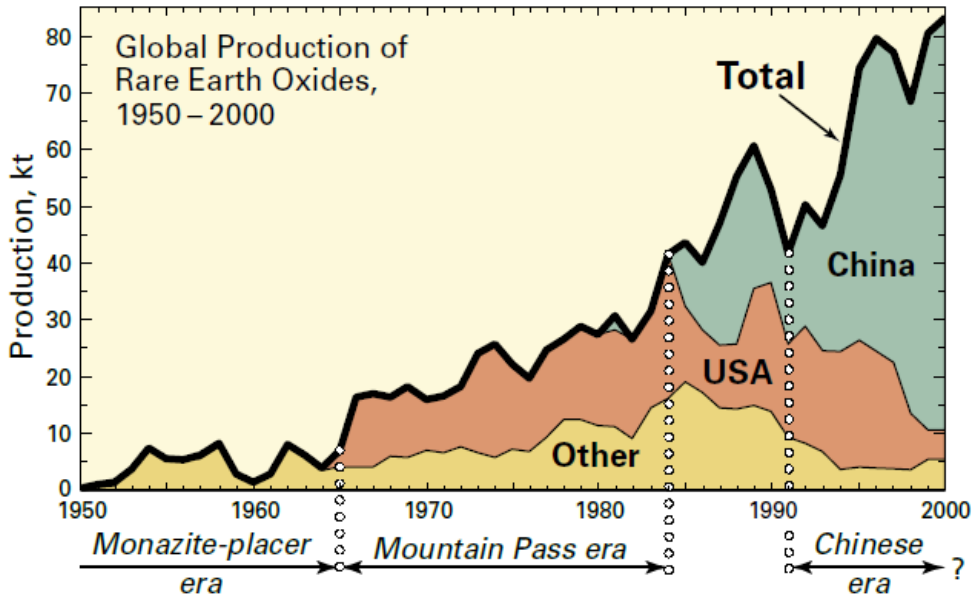

Figure 33: Production statistics of Rare Earth Oxides, showing dramatic rollback of domestic and worldwide production as compared to production by China. This relationship had been beneficial in the development of many REE-dependent technologies, but is now a liability as China moves to protect its reserves by limiting export (USGS, 2002).

With the continued demand for REE and few alternatives available, the export quotas imposed by China highlight the importance of investigating potential sources of REE and the processes by which they are concentrated. High concentrations of REE in preliminary studies indicate that Three Fingers caldera, Oregon may be a viable REE resource. Surveys by Ferns and Cummings (unpublished report, 1996) and Vander

Meulen et al. (1986,1989), showed concentrations as high as 1400 ppm yttrium, 1500 ppm lanthanum, and 1400 ppm cerium in 'mafic clots' within what was mapped as intra-caldera tuff of Spring Creek. Studies of stream sediments draining the caldera show abundances as high as 5000 ppm yttrium and 2000 ppm lanthanum in some samples (Erickson et al., 1986, Hageman et al., 1993). Such high concentrations are considered ore-grade deposits, and are the basis for further study to determine the distribution, abundance, and likely processes concentrating REE in rocks of the Three Fingers caldera.

This study provides evidence that mafic inclusions are clastic in origin, derived from earlier lava flows. Furthermore, their host unit is not the tuff of Spring Creek, but later erupted rhyolite lavas within Three Fingers caldera. New chemical analyses indicate that REE enrichment within mafic clasts is highly variable, but that many individual inclusions show highly anomalous REE concentrations of over 2400 ppm Nd, 1800 ppm Ce, and 1400 ppm La in the most enriched samples. The geographic extent of mafic clast-bearing units is quite limited, and their distribution within these units is typically volumetrically insignificant, limiting their economic potential. Mechanisms for enrichment of REE within these rocks is, however, significant to our understanding of a

yet unexplained phenomenon and may lead to further discoveries with greater economic potential.

2.2 – Background

2.2.1 – Rare Earth elements in petrology and ore grade enrichment

The behavior of REE in magmas has been used by petrologists for decades to constrain magma generation processes. The ionic radii of these elements are a predictable function of their atomic number (Figure 34A), and their mineral/melt partition coefficients vary systematically, while patterns of compatibility changes dramatically between minerals (Lipin and McKay, 1989). The crystallization of minerals therefore leaves geochemical signatures of REE enrichment or depletion in the remaining melt, and can be used to model processes within a magma chamber. More evolved magmas will be comparatively enriched in REE, especially the more incompatible LREE, versus more primitive melts (Figure 35). This is due to the more incompatible behavior of these elements in common rock-forming minerals.

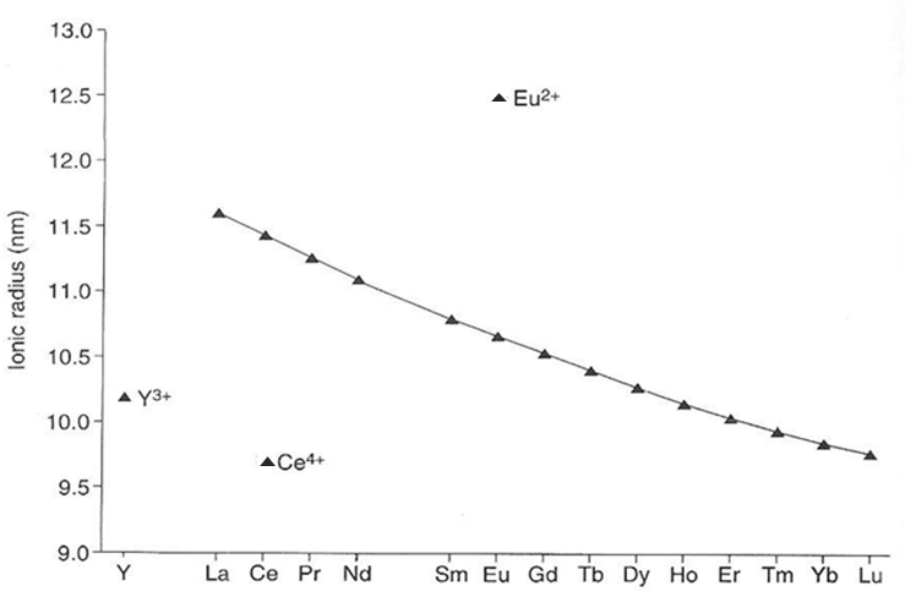

Figure 34: Known as the lanthanide contraction, rare earth elements show a systematic decrease in radius with increasing atomic number, but typically maintain the same charge. Ce^{4+} and Eu^{2+} also exist in varying oxidation states, and behave somewhat differently due to differences in ionic charge and radii. (from Shannon, 1976)

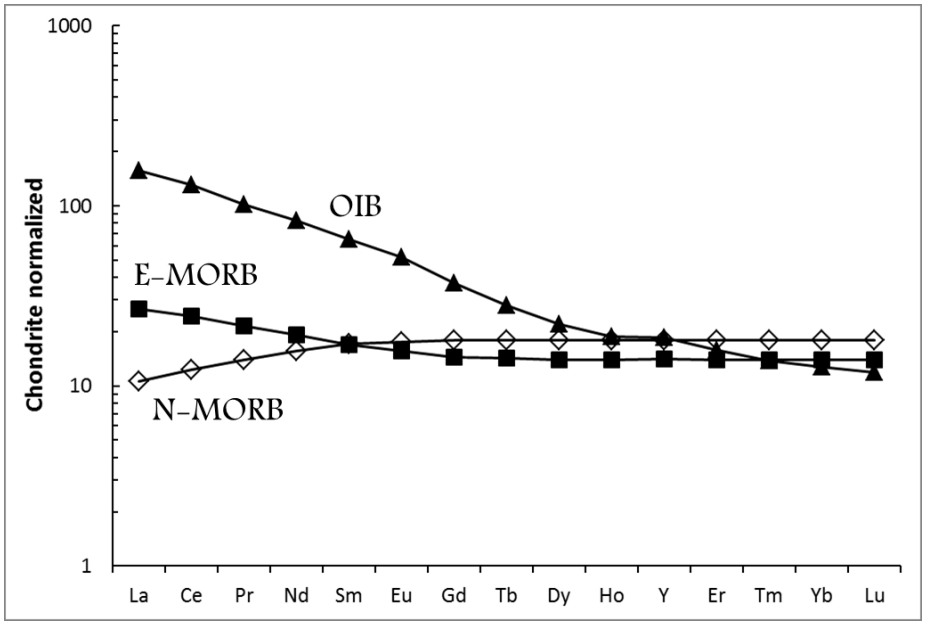

Figure 35: Behavior of the rare earth elements in magma evolution is highly predictable due to the effects of the lanthanide contraction, as displayed in a chondrite normalized rare earth diagram for typical concentrations in Oceanic Island Basalts (OIB), Normal Mid-Ocean Ridge Basalts (N-MORB), and Enriched Mid-Ocean Ridge Basalts (E-MORB). Trace element diagrams are arranged in order of general incompatibility within basalts, but may vary with inclusion of specific mineral phases (values from Sun and McDonough, 1989).

The degree of enrichment required to form REE ore grade resources is only attained within a few known geologic regimes. Carbonatites are igneous rocks composed of greater than 50 percent carbonate minerals, and are the most common host rock for REE ores. The world's largest REE reserve at Bayan Obo mine in Inner Mongolia, China and the largest within the United States, Mountain Pass mine in California, are both carbonatite hosted ores (Jackson, 1993). However Mountain Pass differs from other known carbonatites as the only known example of REE enrichment during primary crystallization, as opposed to hydrothermal enrichment of previously cystallized rocks (Wu, 2008), or supergene mineralization via weathering of carbonate minerals (Jones, 1996; Jackson, 1993).

Other environments well known for producing enrichment of REE are pegmatites and peralkaline rhyolites. Pegmatites are formed within granitic magma bodies as the crystallization of mineral phases concentrates volatiles and incompatable elements in the remaining melt (Evans, 1987). Pegmatites are characterized by unusually high concentrations of Be, Li, W, Rb, Nb, Ta, REE, and U, but with bulk chemistries very close to the host granite. Production grade REE pegmatites exist on the Kola Peninsula of Russia (Jones, 1996) and in the Naegi Granites of Japan (Ishihara,

2008). Peralkaline rhyolites in Egypt , Canada, and Greenland have shown economic potential for REE as well as other high field strength elements (HFSE) including Nb and Zr (Saleh, 2006; Salvi and Williams-Jones, 2006; Jones, 1985).

REE ores created in depositional environments by erosion of REE-bearing rocks are known as placer deposits. Due to the resistance of REE-bearing minerals to chemical weathering, zircon, fluorite, apatite, and xenotime often accumulate in depositional settings such as stream channels and deeply weathered soils (Murakami and Ishihara, 2008). Breakdown of granitic rocks produces saprolite, halloysite, and kaolinite, which have been shown to adsorb REE species in economic concentrations in southern China, the Sanyo Belt of Japan, and laterites of Brazil and Australia (Ishihara, et al., 2008; Morteani and Preinfalk, 1996).

2.2.2 – Aqueous mobility of REE

Despite the general assumption that REE are immobile, there are certain environments where REE may be transported by hydrothermal fluids or surface weathering processes. The existence of REE ore deposits at Bayan Obo and elsewhere that are indisputably of hydrothermal origin provide a clear cut example that REE may be transported in significant quantities (Chao et al., 1992), and within certain

environments can be very mobile (Williams-Jones et al., 2012). These findings have widespread implications for REE exploration, in addition to igneous, metamorphic, and sedimentary petrology.

Laboratory studies conducted to assess the stability of REE in aqueous complexes (Migdisov et al., 2009) have sought to improve on theoretical models proposed based on Pearson's rules (Haas et al., 1995) by simulating the behavior of REE in a hydrothermal environment. These experiments found that prior models greatly overestimated the solubility of HREE in fluoride and chloride solutions (Figure 36). Solubilities of LREE were overestimated for fluoride-rich solutions to a lesser degree, and significantly underestimated in chloride-rich brines, a difference that is amplified at higher temperatures (Williams-Jones et al., 2012).

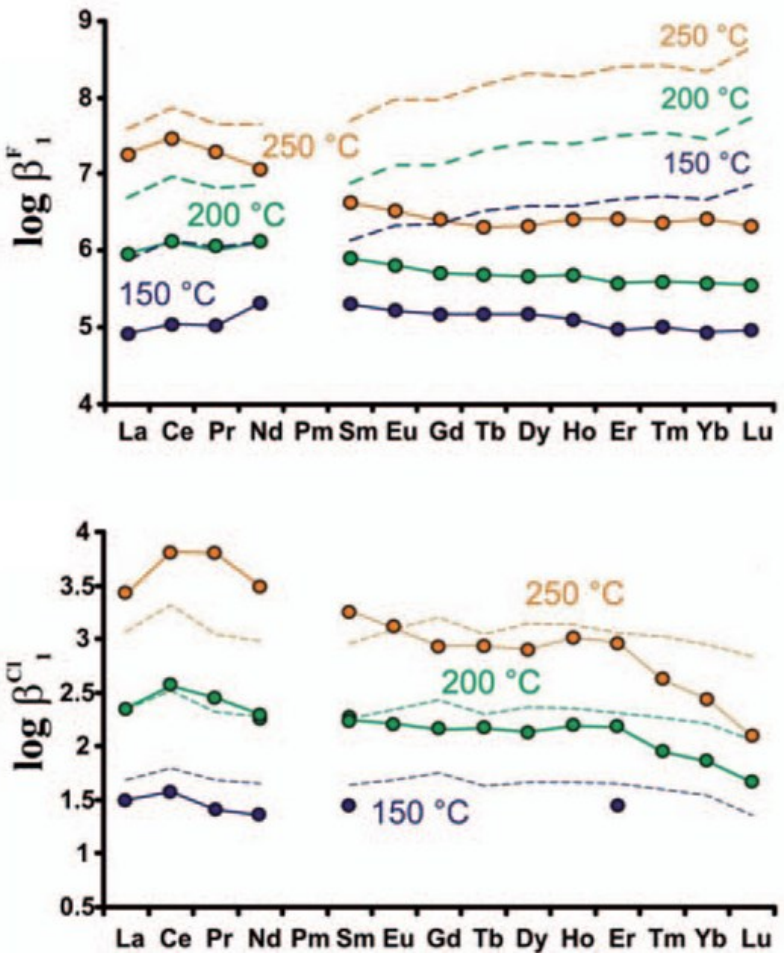

Figure 36: Log formation constants for REE fluoride complexes (top) and REE chloride complexes (bottom) at various temperatures, determined by the ratio of the activity of REE complexes to that of uncomplexed ions in solution. In chloride solutions, LREE are somewhat more stable than HREE, an effect that is heightened with increasing temperature. Solid lines represent experimental data from Migdisov et al. (2009); dashed lines are extrapolated model values of Haas, et al. (1995). Graph from Williams- Jones et al. (2012).

Many REE deposits are associated with fluorite mineralization, but chloride solutions may play a greater role in transport of REE species, with fluoride promoting the precipitation of REE minerals, such as bastnasite, the most widely exploited REE ore mineral. Studies by Migdisov et al. (2009), reveal that while REE chloride minerals are relatively soluble even at ambient temperatures, REE fluorides are extremely insoluble

even at high temperatures. Similar behavior can be cited in the formation of REE phosphates like monazite, where REE are preferentially removed from chloride solutions to precipitate as more insoluble species. (Williams-Jones et al., 2012).

Interaction with carbonate ions $(CO_3)^{2-}$ and increases in pH have also been cited in facilitating deposition of REE ore bodies, as in the case of Bayan Obo, where dolomite is the host rock (Williams-Jones, 2012). The buffering reaction with carbonates neutralizes acidic volcanic fluids through formation of bicarbonate and also liberates Ca^{2+}, which readily reacts with fluorine to deposit fluorite. Given the low solubility of REE-bearing fluorides, fluorocarbonates, and phosphate minerals that tend to act as binding ligands for the REE, chloride appears to have the greatest potential to act as a mobilizing agent.

Changes in pH and temperature also have significant impacts on the relative stability of aqueous REE complexes. Interaction of fluids with high calcium or low temperature rocks, or mixing with low temperature or neutralizing fluids may affect the proportionality of different REE species in solution. The higher stability of LREE versus HREE complexes, even at low temperatures, has been shown experimentally to aid their mobilization to greater distances from the REE source.

Models constructed by Williams-Jones, et al. (2012) to simulate the behavior of REE in a hydrothermal setting suggest that initially, REE are deposited in a pattern corresponding to their aqueous concentrations, but that this pattern changes with continued input of REE-laden fluids. The model uses aliquots with equivalent concentrations of all REE, and simulates the effects of diminished buffering capacity of host rocks, and lower temperatures with increasing distance from the source region. Results show that with continued circulation of acidic, REE-bearing solutions, the nearby rocks lose their ability to buffer these solutions and the REE migrate further from their source region over time. Furthermore, due to the higher stability of LREE than HREE complexes in both fluoride and chloride solutions, the LREE tend to concentrate in locations more distant from their source than HREE. According to this model, early LREE-rich monazite mineralization close to the source was subsequently replaced by more HREE-rich species as fluid circulation continued. As more aliquots of fluid containing equal proportions of REE were added to the system, LREE were preferentially remobilized to greater distances as nearby rocks lost their ability no neutralize pH and temperature.

2.2.3 – Mafic Clasts of Three Fingers Rhyolites

Previous research on mafic clasts of the Lake Owyhee volcanic field is sparse, and lacks an origin for their entrainment. Studies by Vander Meulen et al. (1989, 1991) describe mafic clasts as ellipsoidal, spindle-like "basalt bombs". Vander Meulen et al. (1991) limits the distribution of mafic clasts to the upper 10 to 15 m of what was mapped as intra-caldera tuff of Spring Creek (see Chapter 1).

Anomalous concentrations of REE in entrained mafic clasts were first reported by Ferns and Cummings (1996), from samples collected during thesis work of Brian Zimmerman (personal communication between Zimmerman and Ferns, 1990). These samples contained up to 1400 ppm yttrium, 1500 ppm lanthanum, and 1400 ppm cerium. In addition, stream sediment surveys of drainage basins feeding Lake Owyhee by Erickson and others (1986) show values greater than 2000 ppm for La and greater than 10000 ppm Y in the Honeycombs Wilderness Area. Later studies by Hageman and others (1993) of sediments in the drainages of Leslie Gulch to the south show concentrations of up to 1000 ppm La and greater than 5000 ppm Y in sediment concentrates. Rock samples from the same studies showed no anomalous concentrations of REE, and likely sources for their enrichment in sediment samples were not identified.

2.3 – Methods

Geochemical analyses of mafic clasts were performed at the GeoAnalytical Lab of Washington State University, utilizing X-ray fluorescence (XRF) and inductively coupled plasma mass spectrometry (ICP-MS), and the Trace Element Analytical Laboratory (TEAL) at Portland State University using inductively coupled plasma optical emission spectrometry (ICP-OES). In total, 9 mafic clasts were selected for XRF and ICP-MS analysis at WSU, in addition to basalt flow sample TF-330. Procedures for sample preparation and analytical techniques at WSU are listed in Chapter 1 of this volume. Forty-seven mafic clasts were dissolved using microwave-assisted acid dissolution for ICP-OES analysis in the TEAL laboratory at Portland State University to determine REE and other select elemental concentrations.

2.3.2 – Acid dissolution for ICP-OES analysis

Two trials were run on samples collected for this study on the ICP-OES, the first of which was performed in May of 2012, after trial digestions were performed on known standards using six different acid recipes (Table 3). Three reference standards were selected for digestion, coal fly ash 1633a, JG-2 granite from the Geological Survey of Japan, and Devine Canyon Tuff sample DC-01-09 from the collection of Dr. Martin

J. Streck. Each of the three standards was digested in each of the six recipes to assess the effectiveness of each recipe on different materials.

All digestion recipes maintained the same HNO_3 content, but ratios of HCl and HF were modified to bring the total volume of the three acids used in each trial to 9.0 ml. In addition, the last three trials contained 6 ml of saturated boric acid solution (~5%), bringing the total volume of the solution to 15 ml. This was done to reduce possible effects of any unused HF acid complexing with analytes to form precipitates, thus losing recovery of these species in solution. three ml of boric acid solution was added before microwave digestion in trial 5, with the additional 3 ml added during dilution once samples were cooled. The entire 6 ml of boric acid solution was added after microwave digestion for trials 4 and 6.

Table 3: Six recipes used for the digestion of three reference samples in an effort to define the best method for whole rock digestion of study samples. Total volume of strong acids remained equal, varying the ratio of HCl to HF, with addition of boric acid to the last three methods.

Method	HF (ml)	HNO_3 (ml)	HCl (ml)	Initial H_3BO_3 (ml)	Total H_3BO_3 (ml)
I	2	2	5	0	0
II	1	2	6	0	0
III	0.5	2	6.5	0	0
IV	1	2	6	0	6
V	1	2	6	3	6
VI	0.5	2	6.5	0	6

Approximately 0.20 grams of each reference material were dissolved during the trial runs, with exact masses recorded for calculation of solid concentrations. After microwave digestion in Teflon canisters, samples were then cooled overnight, and diluted to a total volume of 20 ml, using boric acid solution for methods 4-6, and ultrapure deionized water. This dilution factor made calculations relatively simple, resulting in a final concentration of 0.01 g sample per ml solution. For ICP-OES analysis, each sample was further diluted to the equivalent of 100 ml by adding 2 ml sample solution and 8 ml of ultrapure water to each replicate. This final dilution was performed to achieve the concentration range of selected elements for which the ICP-OES is most accurate, and to lower the concentration of strong acids, including HF. These acids are detrimental to the longevity of several components within the ICP-OES, and increase the likelihood that 'matrix effects' resulting from the high acid concentrations will affect results (Perkins, personal communication, 2012).

Results of these trials indicate that use of boric acid improved analyte recoveries, in addition to lowering the amount of hydrofluoric acid used (see Appendix B). Adding 3 ml boric acid solution during microwave digestion (method 5) resulted in reduced recoveries compared to addition of the entirety of boric acid after cooling (method 4),

but overall accuracy was improved over standards diluted with water only (Figure 37). Methods 4 and 6 provided the most consistent recoveries, with half as much HF used in method 6. For this reason, method 6 was selected as the best option for processing study samples, due to health risks associated with use and disposal of HF-containing solutions and contaminated solids.

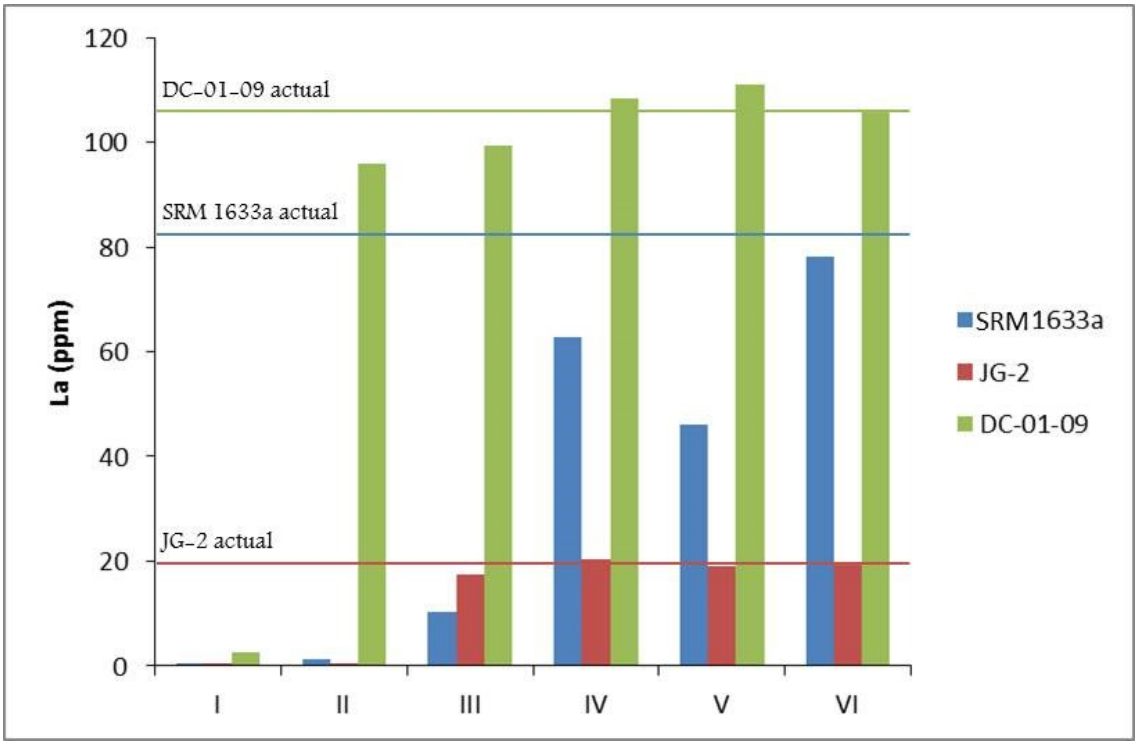

Figure 37: Standard abundances measured by ICP-OES for each of the six methods used for sample digestion (see Table 3) compared to known abundances for La. Three standards were used for comparison, coal fly ash (SRM 1633a), granite from the Japanese geological survey (JG-2), and Devine Canyon Tuff (DC-01-09) from the collection of Martin J. Streck. More consistent recoveries are demonstrated in methods IV-VI, which included the use of boric acid. Some improvement is observed in lowering HF from 2.0 ml to 0.5 ml in methods I-III.

2.3.3 – Calibration of OES data

Overall, eight external standards were used for the calibration of ICP-OES data prepared and analyzed in the TEAL lab, including the DC-01-09 Devine Canyon Tuff sample, and USGS standard BHVO-01 Hawaiian basalt. In addition, two study samples, TF-181 and TF-218 for which XRF and ICP-MS data existed were also used for calibration. Eight of the samples analyzed by ICP-OES were later analyzed at WSU, after being selected as representatives of high-REE or low-REE groups. This approach enabled

a further correction procedure for OES data, tuned to the specific compositions of rocks within this study.

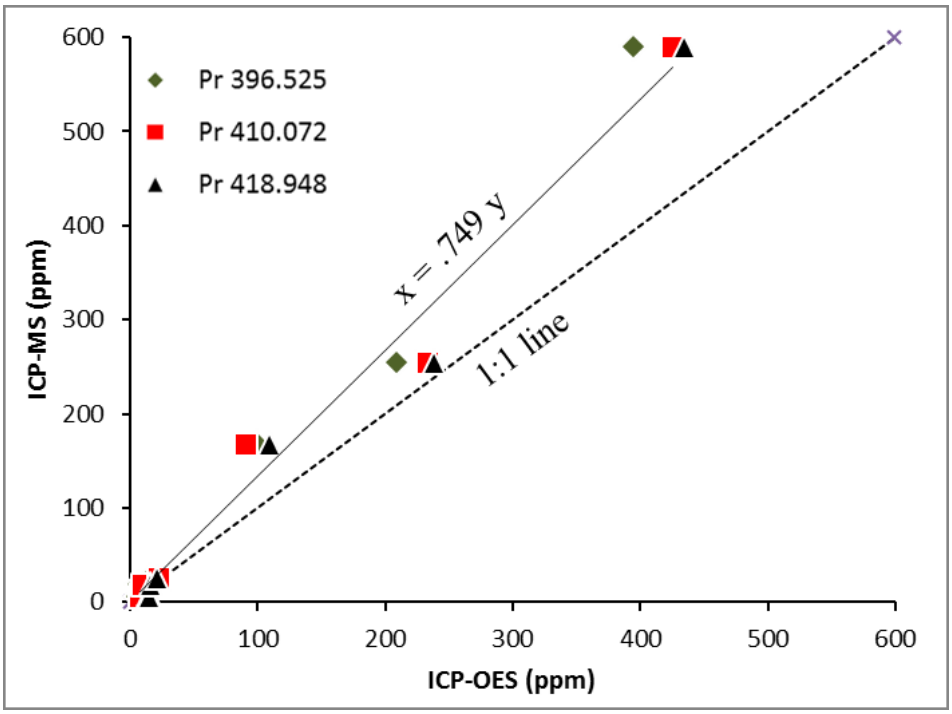

Figure 38: ICP-MS values versus those obtained via ICP-OES for three separate wavelengths: 396.525, 410.072, and 418.948. Final ICP-OES data used in this study were obtained from recalculation of original measurements using regression generated from this comparison for each element analyzed. As seen here, ICP-OES values are somewhat below standard values for praseodymium. Regression was fit to the wavelength showing best initial correlation to the 1:1 line.

Values recorded via ICP-OES were corrected by comparison of ICP-OES values with expected values in external standards (Figure 38). A linear regression of these data was performed for each element analyzed to determine the relationship between observed and expected values. The formula derived for the best fit line was then applied to raw ICP-OES data to correct analytical results of study samples. Goodness of fit was

assessed for each linear relationship by R-squared value, and only those elements with values above 0.85 were accepted for further interpretation. An example of the resulting precision is given by plotting ICP-OES values versus ICP-MS values for the elements La and Ce (Figure 39).

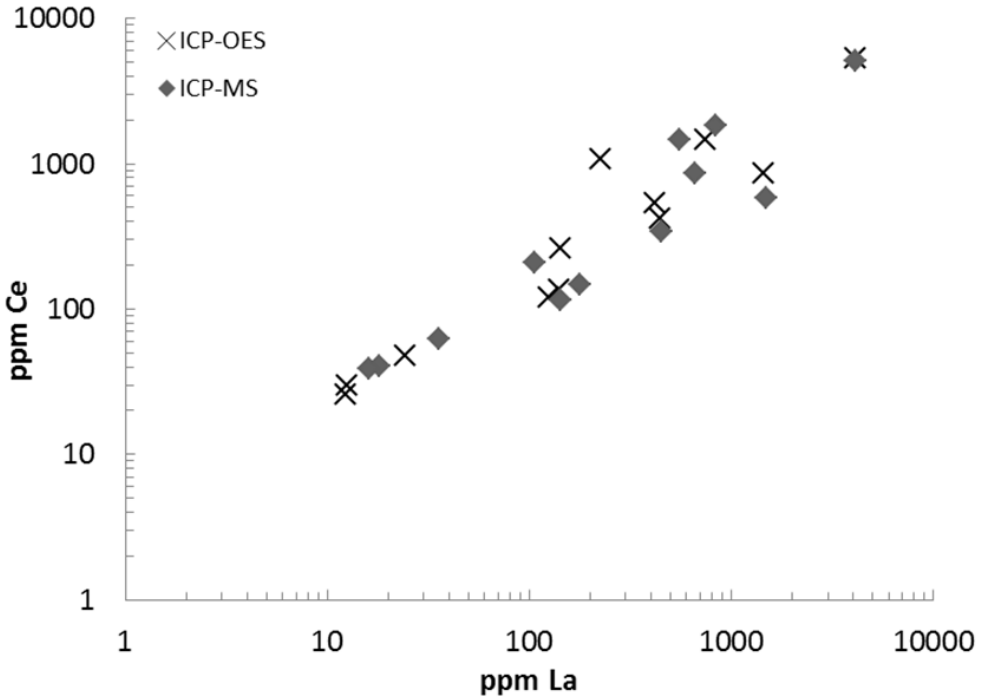

Figure 39: Example dataset comparing values for Ce vs. La in eight samples used as standards for ICP-OES calibration. While some degree of scatter exists between the two datasets, values are sufficient to illustrate the same trend of enrichment between the two elements.

2.4 – Results

2.4.1 – Mafic Clast Distribution

During mapping of rhyolites within Three Fingers caldera, mafic clasts were sampled from each outcrop in which they were found to assess variations in appearance, mineralogy, and geochemistry. Clast-bearing outcrops are largely concentrated in the central part of the study area (Figure 40) with clasts typically limited to the lower 5-10 meters of porous devitrified rhyolite exposures. While most outcrops sampled contain individual clasts large enough for geochemical and petrographic analysis, other outcrops contained only small clasts. In these locations, samples represent multiple clasts collected from the same host facies.

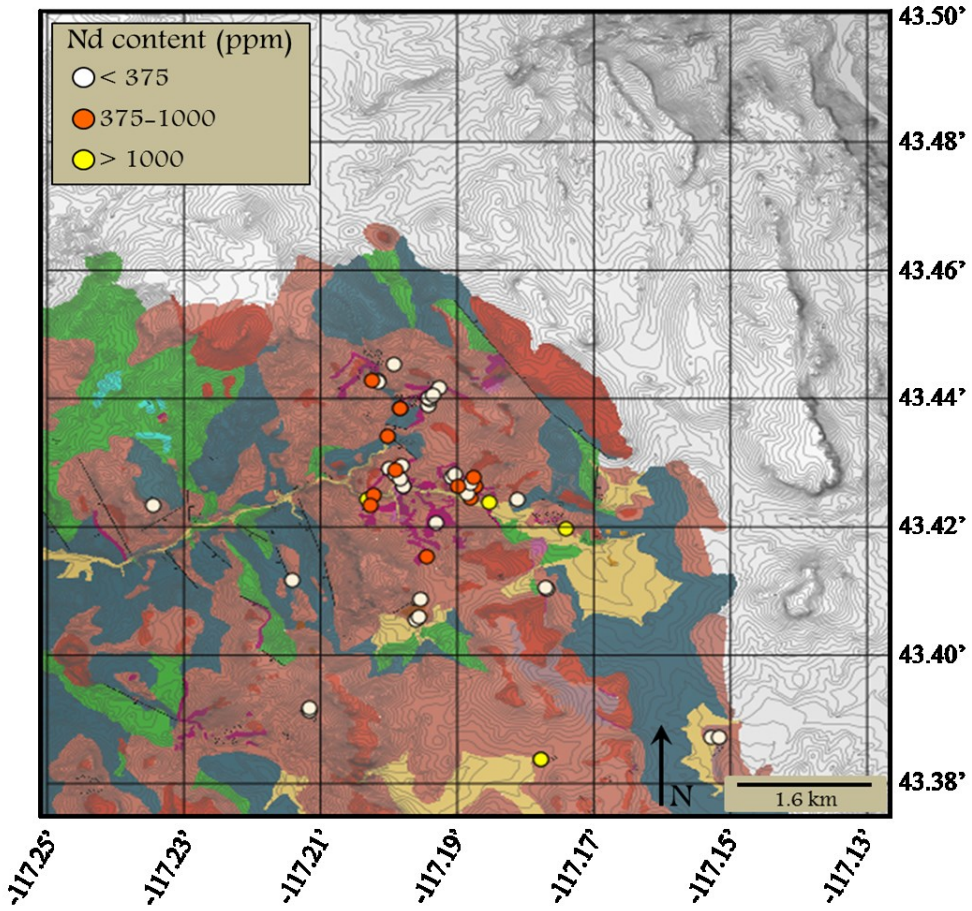

Figure 40: Sample location map for mafic clasts collected in this study. Note the high density of samples collected in the central portion of the study area. Yellow symbols indicate the highest abundance of Nd, at greater than 1000 ppm, orange = 375-1000 ppm, and white = less than 375 ppm.

2.4.2 – General appearance and field relations

Mafic inclusions hosted within intra-caldera rhyolites of Three Fingers caldera are most often found, and in the highest abundances, within the porous devitrified rhyolite facies. These rhyolites were erupted shortly after caldera collapse after a period of lacustrine and fluviatile sedimentation within the basin, in the form of domes, coulees, and associated central plugs. The porous facies likely represents lavas within

the outer glassy carapace of these domes, variably devitrified and often intermixed with glassy breccias resulting from dome collapse. Within breccias, small mafic clasts are often present alongside larger inclusions of underlying siltstone and other clastic debris. Smaller proportions of clasts are observed in dense glass, porous glass, and monomict glassy breccias within the study area. No mafic clasts were observed in central plugs or lava flows of the dense devitrified facies.

The previous description (Vander Meulen et al., 1989, 1991) of mafic clasts as 'basalt bombs' suggests that they are basaltic in composition and pyroclastic in nature. Chemical results of this study (Appendix A) reveal they range from basaltic andesite to dacite (54.5 to 65.5 wt.% SiO_2). Clasts are significantly more mafic in composition than the rhyolites that host them, and are therefore distinctly different in appearance. From here onward, I will call these inclusions 'mafic clasts' to avoid the implication that these are true basalts.

Outward appearance of hand samples ranges from very dark grey, resistant rocks that show little surface texture, to light grey friable rocks with a sandy texture. On the whole, mafic clasts are aphyric to very sparsely phyric, with some samples showing few visible phenocrysts of plagioclase, typically smaller than 1mm. Some

samples exhibit a distinct weathering rind of oxidized material from deep red to dark yellow in color, often staining the surrounding host rock within millimeters to several centimeters of contact (Figure 43), while others maintain a sharp boundary with the host rock and no discoloration (Figure 42).

Most commonly, mafic clasts are subrounded to angular, and are 5–10 cm in diameter. Some locations contain large clasts up to ~40 cm in diameter and clasts can also be very angular, but these instances are the exception. Mafic clasts make up no more than 10% of any outcrop observed, and most typically compose less than 2–3% of exposed outcrops. The greatest concentration of mafic clasts are found as float in small gullies, typically below exposures of clast-bearing rhyolite, but most often the source cannot be found upsection. Low-REE sample TF-181 was recovered from a streambed near Saddle Butte Reservoir in the SE corner of the study area, directly adjacent to an exposure of mafic clast-bearing porous devitrified rhyolite. These examples are noteworthy as they are glassy and aphyric. They make up more than half of colluvium filling the streambed (Figure 41).

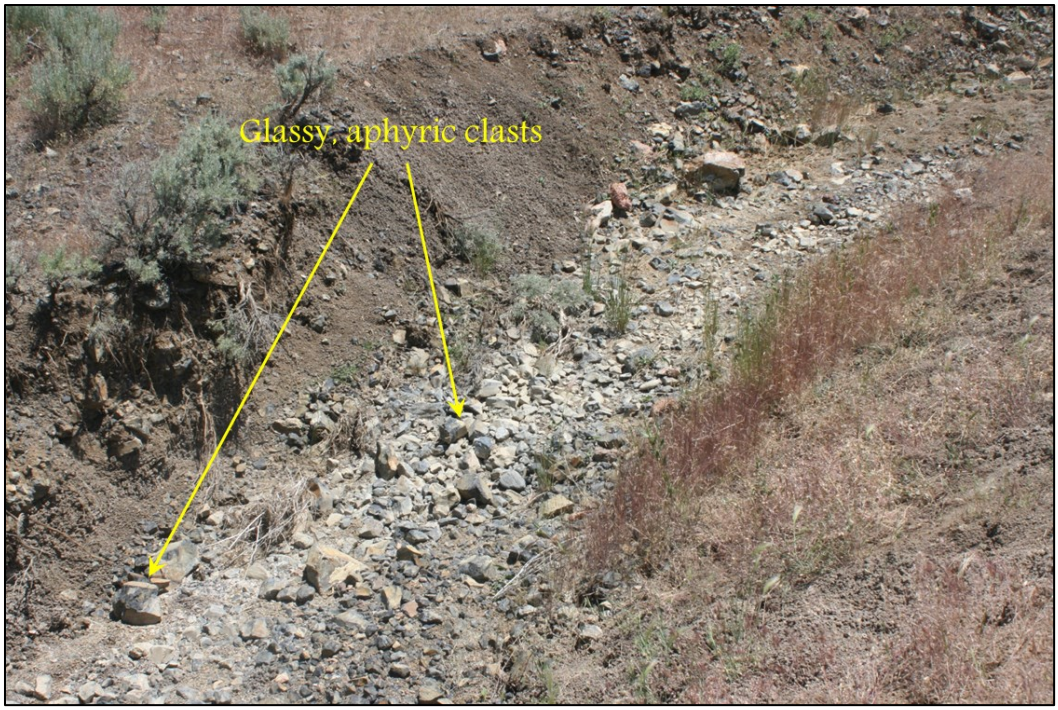

Figure 41: Sample TF-181 was collected from a streambed NW of Saddle Butte, where dense glassy, aphyric rocks make up the majority of colluvium. No other location within the study area contained similar specimens.

Mafic clasts housed in dense and porous glass, including glassy autobreccias typically show less weathering and are darker and more resistant, but are often broken into angular fragments (Figure 44A). Due to the similar color, and similar degree of resistance, mafic clasts are more difficult to discern within dense black glass, and most locations were devoid of clastic debris. Mafic clasts within highly resistant silicified porous rhyolites were targeted for sampling to assess possible effects of hydrothermal circulation. Where found, clasts were collected from within dense green areas or those directly exposed to precipitated quartz or calcite (Figure 44B).

Figure 42: Mafic clasts appear in most facies of intra-caldera rhyolites, typically angular in external form, and variably weathered. Clast in (A) shows flow banding, platy fracture, sandy texture, and is medium gray in color. Specimen in (B) is massive in appearance, with a waxy texture and dark gray, showing discoloration due to oxidation.

Figure 43: Mafic clasts entrained in porous devitrified rhyolite, exhibiting deep red staining due to oxidation. Host rock in (A) shows little weathering, and little staining beyond the margin of the entrained clast. Much of the oxidation rind appears to be 2-3 mm from the interface with the host rock. Host rock in (B) is extensively weathered, and nearby regions have been stained by oxidation of iron within the entrained clast.

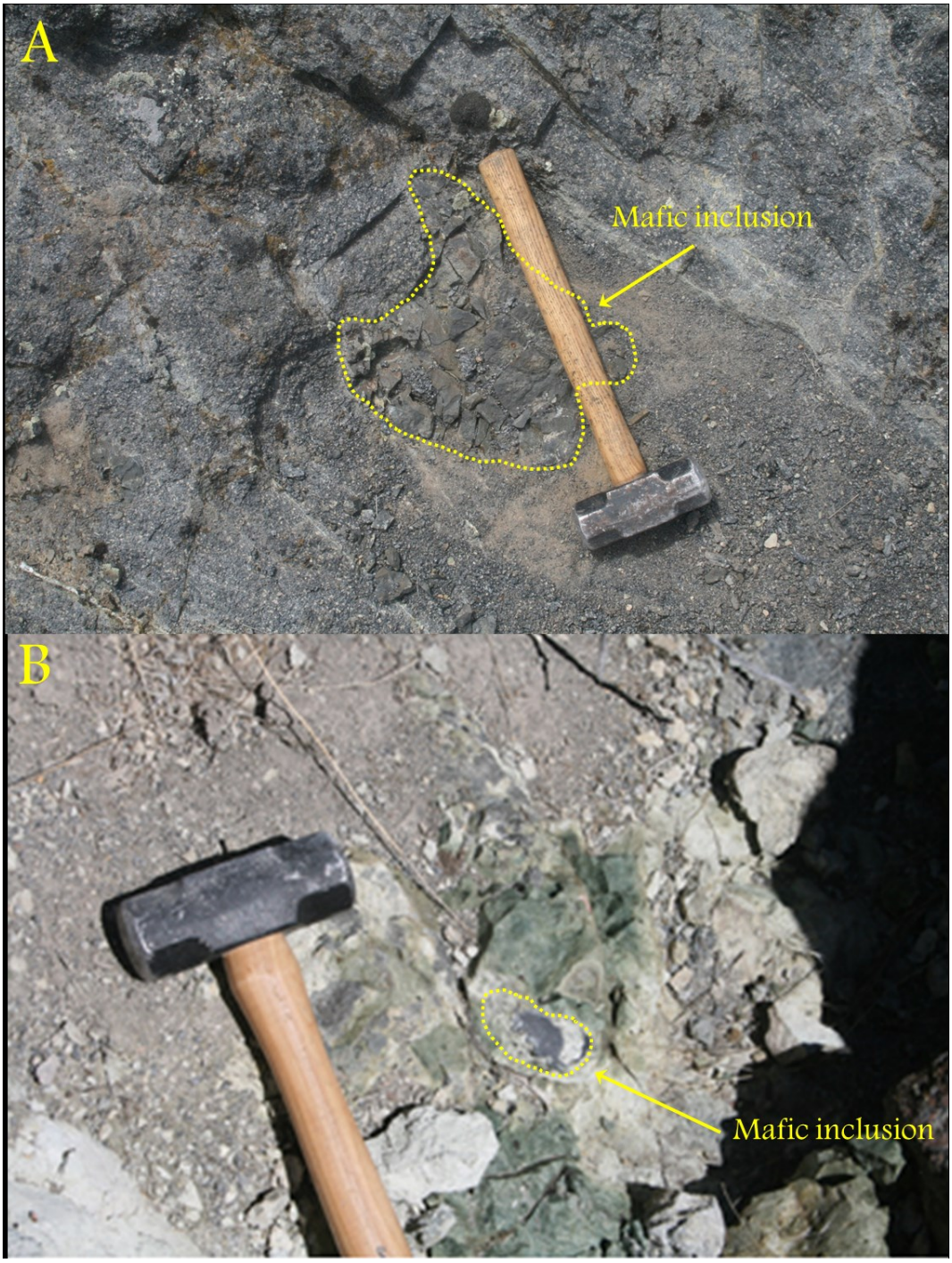

Figure 44: Less commonly, mafic clasts are found in the dense glassy facies of intra-caldera rhyolite (A), where they are difficult to extract. This example is ~25 cm, and is dark gray, waxy, and massive in form. Small mafic clast pictured in (B) is surrounded by altered porous devitrified rhyolite, which is commonly stained green and very resistant.

2.4.3 – Petrography of mafic clasts

Mafic clasts are typically aphyric, with few samples containing rare phenocrysts of partially resorbed plagioclase (<1%), with minor clinopyroxene and anhedral olivine. The groundmass is finely textured, and fibrous in appearance, composed of 50-60% plagioclase microlites and 15-20% oxides, with glass making up the remainder. Oxides are anhedral to euhedral, with external forms showing both cubic and needle-like habit common. Groundmass plagioclase sometimes displays penetration twinning at 60 degrees between three laths, resulting in a snowflake appearance. Some samples show evidence of flow banding, with jagged, sub-parallel cracks that are typically infilled by mineralization of tan to red cryptocrystalline material. This pattern is often distinguishable in hand sample and resembles the uppermost exposures of mafic lava flows found within the caldera (see Chapter 1). Variable formation of red to brown rinds of no more than 1mm occur at the contact between mafic clasts and surrounding host rock (Figure 45), and are comprised of a thread-like cryptocrystalline fabric.

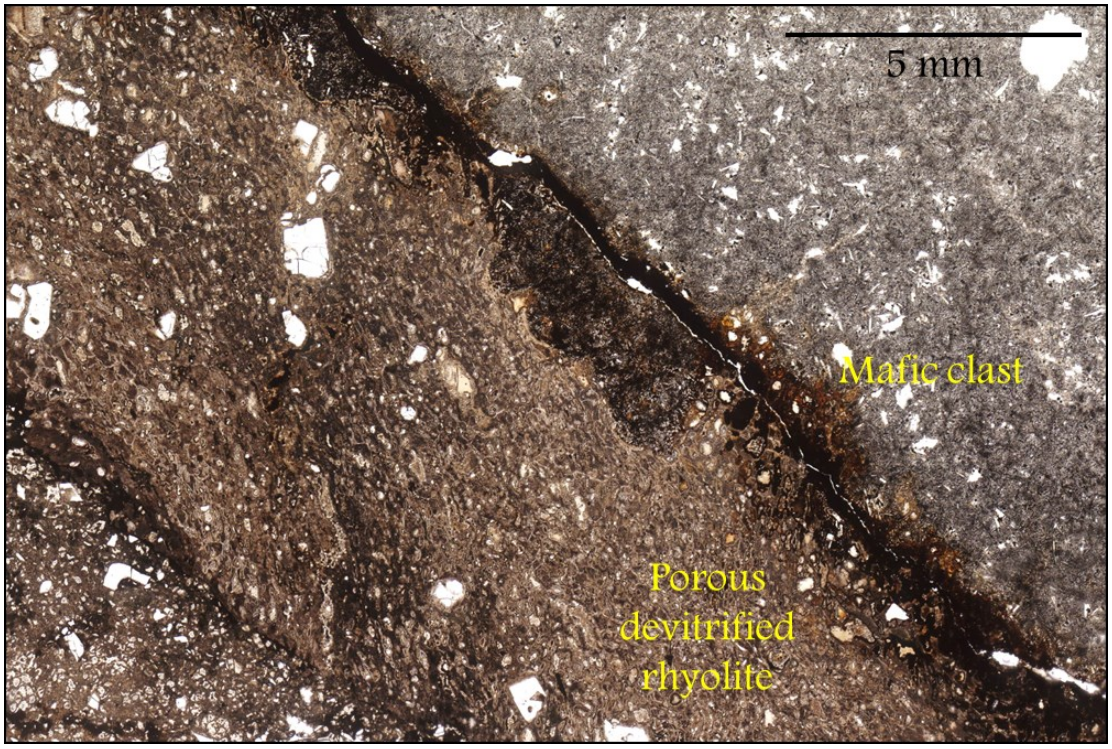

Figure 45: Sample TF-21c exhibits a dark rind in contact with host porous devitrified rhyolite. Groundmass texture is composed of very fine plagioclase and oxides, with rind composed of deep red cryptocrystalline material.

2.4.4 – Geochemical Results

In this section, XRF and ICP-MS data from nine study samples are compared, in addition to XRF data for three samples from the collection of Mark Ferns. Samples were divided into high REE and low REE groups in an attempt to highlight major element trends relating to REE enrichment. These groups were established based on La+Ce+Y/Zr ratios of greater or less than 10 to account for differences in relative enrichments in high-REE samples. Zirconium was chosen to differentiate enrichment of REE from petrogenetic processes that would have also enriched Zr. Lava flow sample TF-330 is

not regarded as a mafic clast, though its appearance closely resembles many mafic clasts, and provides a reference for a mafic lava flow within the caldera.

2.4.4.1 – Major element geochemistry of mafic clasts

Mafic clasts vary in silica content from 54.5 to 64.9 wt.% SiO_2. Lava flow TF-330 contains the lowest silica of all samples collected at 52.1 wt.% SiO_2. Comparisons of FeO* with SiO_2 (Figure 46, top) display expected magmatic depletions in iron content as silica increases, beginning at low-silica, high iron (52.1 wt.% SiO_2, 10.0 wt.% FeO*) TF-330. While both groups display a negative correlation between iron and silica content, high-REE samples contain less iron than low-REE samples having similar SiO_2 contents. Magnesium shows similar depletions with increasing silica content, but the most REE-enriched samples stand out (Figure 46, bottom). Three high-REE samples show very low MgO concentrations of less than 0.4 wt.%, while all low-REE clasts appear to fall along the negative trend, sloping away from TF-330.

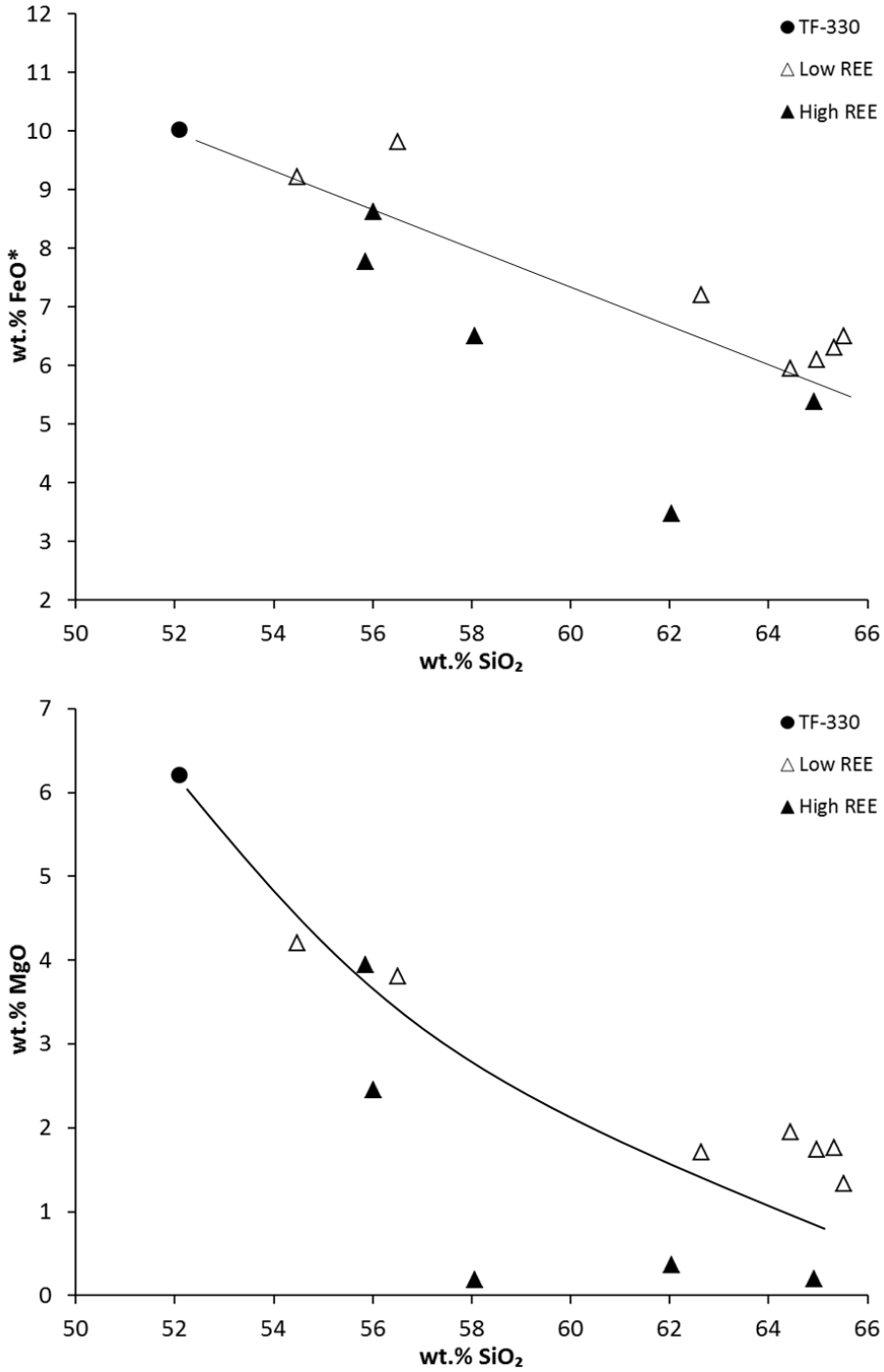

Figure 46: Harker diagrams of FeO and MgO versus SiO_2, using XRF totals from WSU. displaying sytematic depletion of these two elements with increasing silica. A distinct cluster of high FeO samples appears between 64-66 wt.% SiO_2, with similar placement for MgO. High REE samples are generally lower in FeO and MgO than their low-REE counterparts at similar silica content.

Aluminum contents show no distinctive pattern for the high-REE clasts, but abundances are generally elevated compared to the low-REE group. Average for the high-REE group is 18.6 wt.% Al_2O_3, compared to only 14.7 for the low-REE samples, with significantly higher variance (4.1 versus 2.5, respectively). A comparison of Al_2O_3 versus MgO (Figure 47) highlights divergent trends between the two groups with an apparent positive correlation observed between the two elements in low-REE clasts with a less consistent, but inferred negative correlation in the high-REE samples.

The same processes that enriched REE likely also caused changes in major element composition that vary widely, and inconsistently with magmatic trends. Thus, relatively unaffected rocks likely reveal their original magmatic composition, with mafic clasts originating from lavas of basaltic andesite to dacite in composition. The Al_2O_3 content of the high-REE group shows much greater variance than the low-REE group, with a standard deviation more than five times greater. Average MnO is slightly lower in the high-REE group (Figure 48), but the variance is again much higher, more than 5.5 times greater than for low-REE samples.

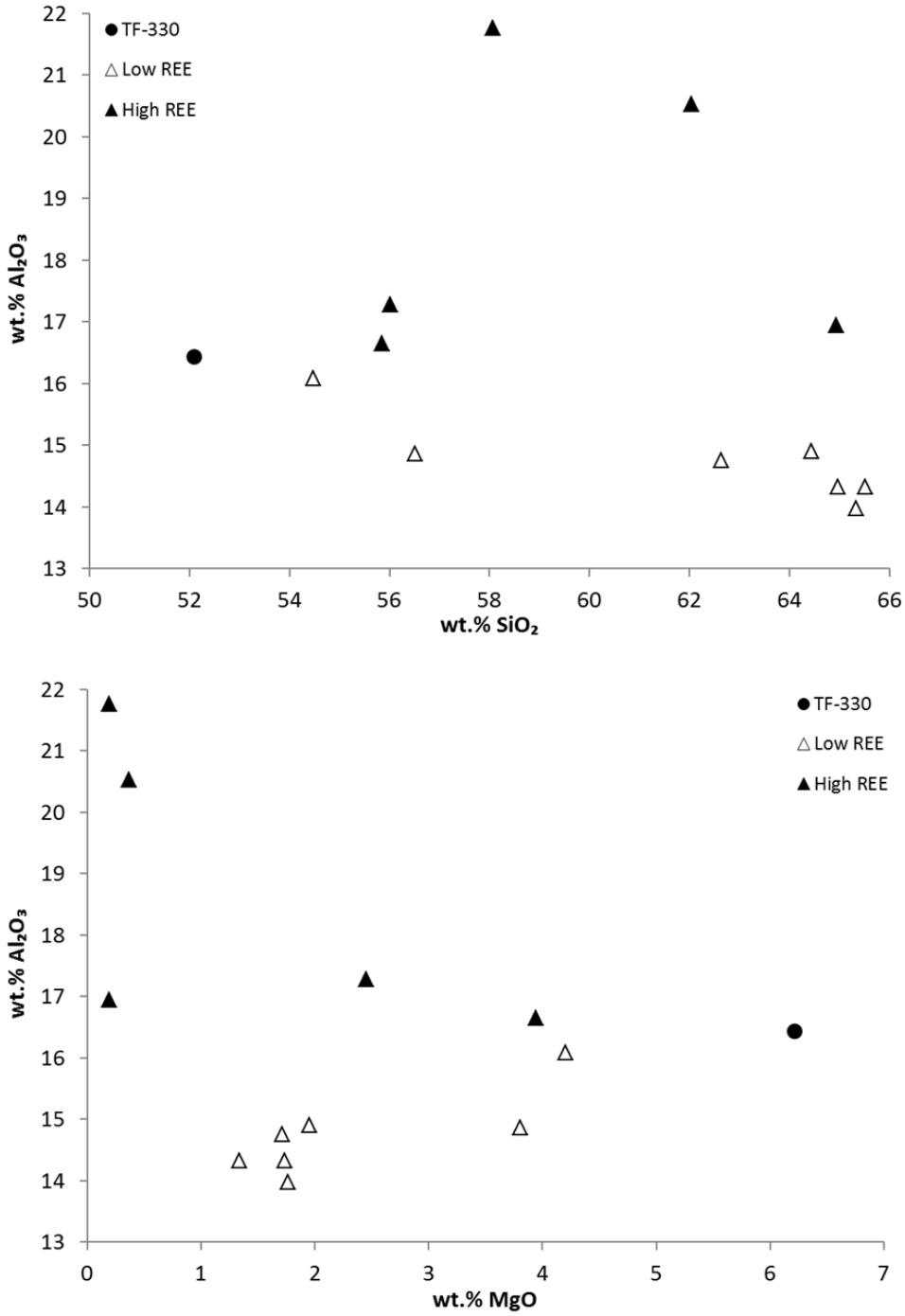

Figure 47: Patterns of aluminum enrichment differ significantly between high and low REE groups, with all but one high REE sample (BBM-04) having higher aluminum concentrations. Aluminum versus magnesium illustrates two fairly distinct patterns between the groups, tracking away from composition of basalt flow TF-330.

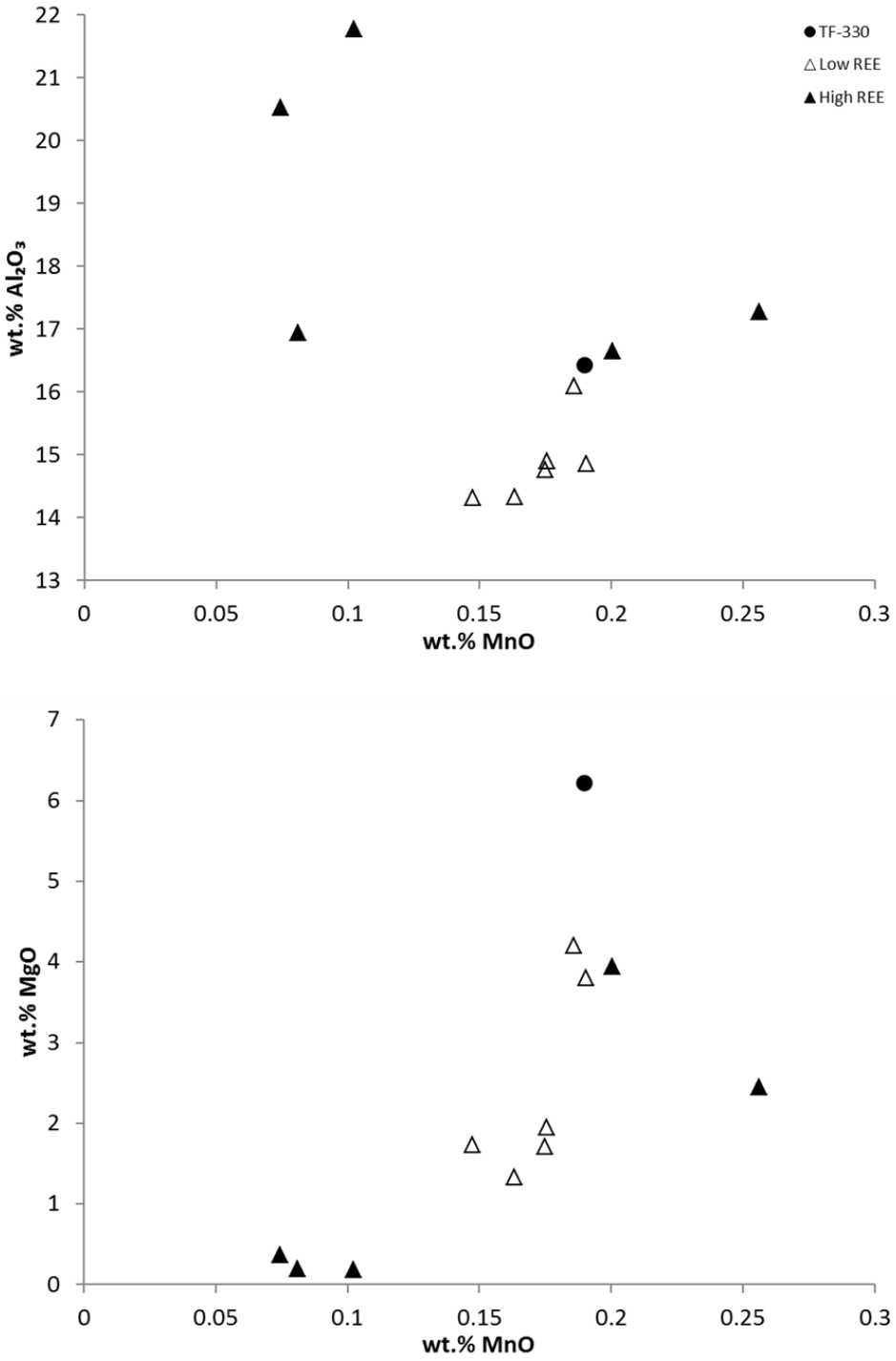

Figure 48: Significantly higher variance in MnO content among high-REE clasts differentiates them from the low-REE group, which forms a distinct cluster when plotted against aluminum (top). When MgO is plotted against MnO, however, three distinct groups appear, with corresponding loss of both elements from TF-330.

2.4.4.2 – Trace element geochemistry of mafic clasts

Comparison of analytical results for high and low-REE mafic clasts show significant differences in the concentrations of REE, as well as U and Pb (Figure 49). Average values for LREE (La-Sm) are 23.6-38.6 times greater for high-REE versus low-REE samples, with average Pb and U enrichments at 6.8 and 6.2 times the low-REE clasts, respectively. The scale of these enrichments is not observed for other incompatible elements, excepting Y, which generally behaves similarly to the lanthanides, and in further discussion will be grouped accordingly.

A common feature of both high and low-REE groups are anomalously high U and Pb values, as compared to other incompatible elements (Figure 49). The more enriched samples contain an average of 61 ppm lead, with less enriched clasts averaging only 23 ppm. Uranium is also elevated in the high-REE group, averaging 27 ppm as opposed to 9 ppm in the low-REE samples. This pattern does not hold for high-REE sample TF-218c, however, with only 4.4 ppm, the lowest overall total. A comparison of Pb versus Nd for all samples, including those processed on the OES show consistent correlation between LREE and Pb enrichment (Figure 50).

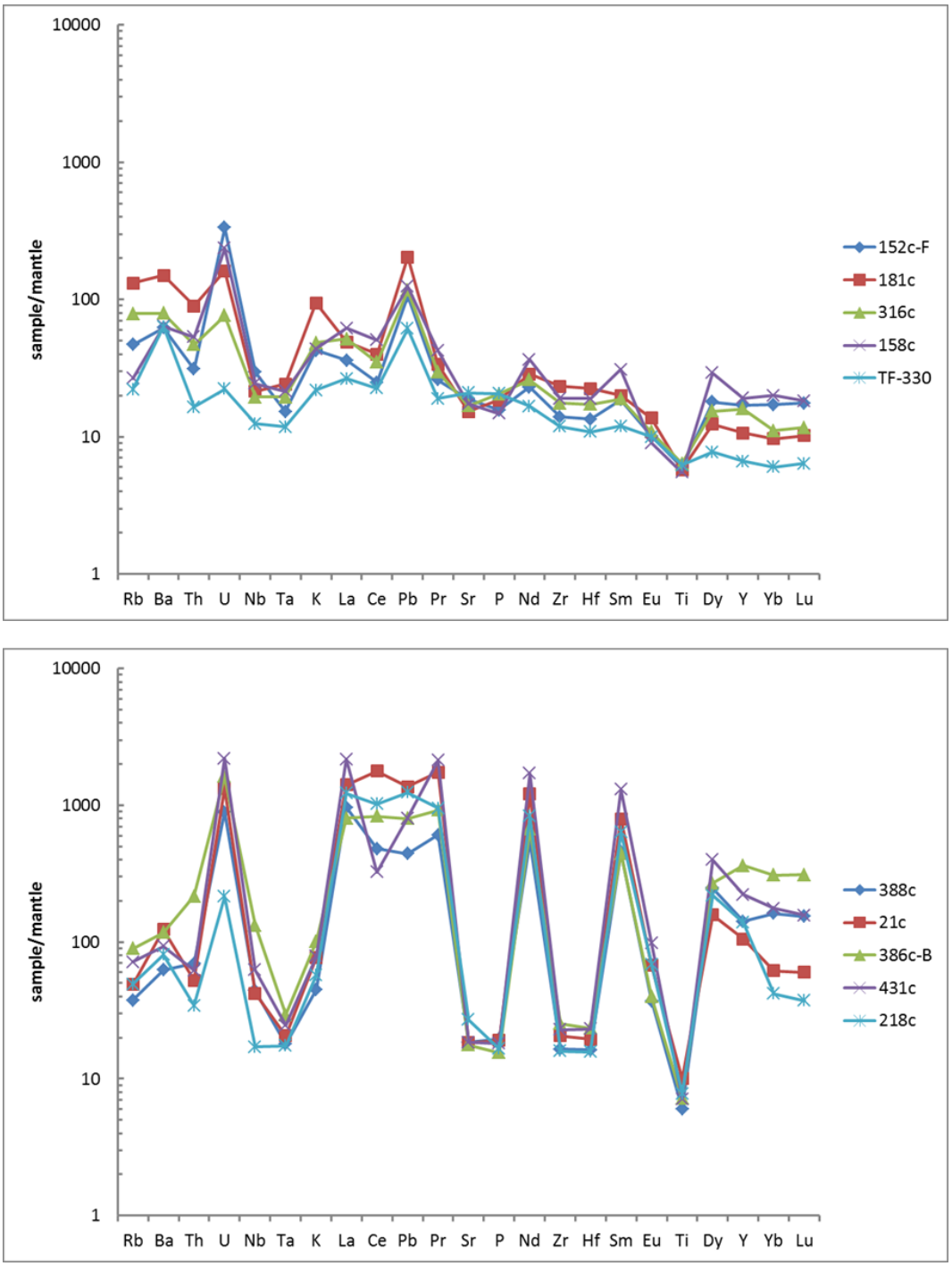

Figure 49: Multi-element normalization diagrams for low-REE (top) and high-REE mafic clasts (bottom), with abundances normalized to primitive mantle values of Sun and McDonough (1989). As expected, distinct enrichments are apparent in REE abundances between the two groups, in addition to Pb and U. Troughs formed by HSFE, most notably Ta, Zr, Hf, and Ti are similarly distinct, with slight relative increases in Nb.

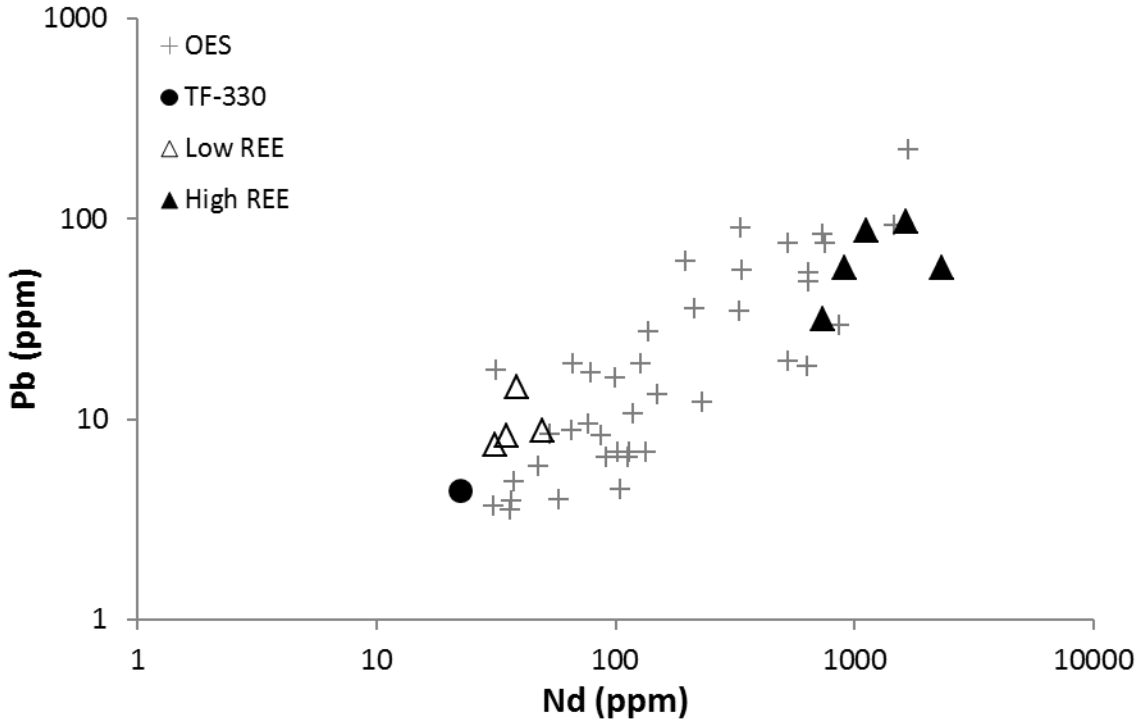

Figure 50: Pb versus Nd on a log plot illustrates general enrichment of both elements, albeit with some scatter. Note that basalt flow sample TF-330 places at the lower end for each element, though itself shows a positive anomaly for Pb.

High field strength elements (HFSE) Ta, Zr, and Hf show mild enrichments of 9-10% in the high-REE group, with Nb enriched by an average of ~250%. Zr/Hf ratios remain nearly constant, with values of high and low-REE groups ranging between 36.3-37.8 and 35.7-39.1, respectively. Sr and P do not show increases in high-REE samples, relative to low-REE mafic clasts. U and Pb show distinct positive anomalies in both groups, with further enrichment correlating to that of REE.

Nb is enriched relative to Ta within the high-REE group, except in sample TF-218c, which also shows the least enrichment in Th and U. Enrichment of Nb correlates

with enrichment of HREE, with sample 386c-B the most enriched in HREE and Nb (Figure 51). Low-REE samples show elevated levels of Nb compared to lava flow TF-330, which is likely due to magmatic processes.

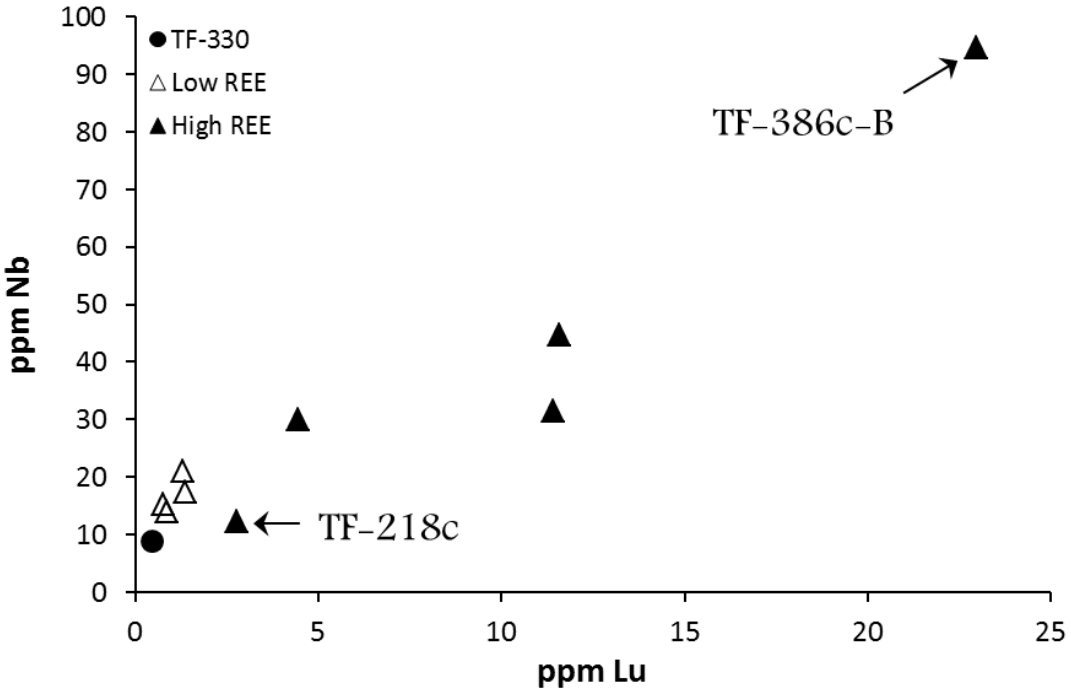

Figure 51: Variation diagram of Nb versus Lu, illustrating a positive correlation between Nb and HREE. Sample TF-218c contains only 12 ppm Nb, the least of any mafic clast, compared to 95 ppm Nb in TF-386c-B. Data from Mark Ferns does not include Lu values, so these are not plotted here.

2.4.4.3 – Patterns of REE enrichment

Enrichments across the suite of REE are quite different between mafic clasts sampled, with variability increasing as a function of REE enrichment. Chondrite normalized REE diagrams (Figure 52) show a strong Eu anomaly in high-REE samples that is not shared by low-REE clasts. No Eu anomaly occurs in lava flow sample TF-330, which also contains the lowest overall values for REE. Values for Eu/Eu* in low-REE

clasts range from 0.32 in TF-158c to 0.80 in TF-181, which then correspond with overall REE enrichment during magmatic evolution from andesitic to dacitic magmas. The high-REE samples consistently produce stronger anomalies, with Eu/Eu* values ranging from 0.10 in sample TF-388c to 0.14 in sample TF-21c. It is important to note that Eu is still relatively enriched in high versus low-REE samples, but show much less enrichment than other REE (Figure 53).

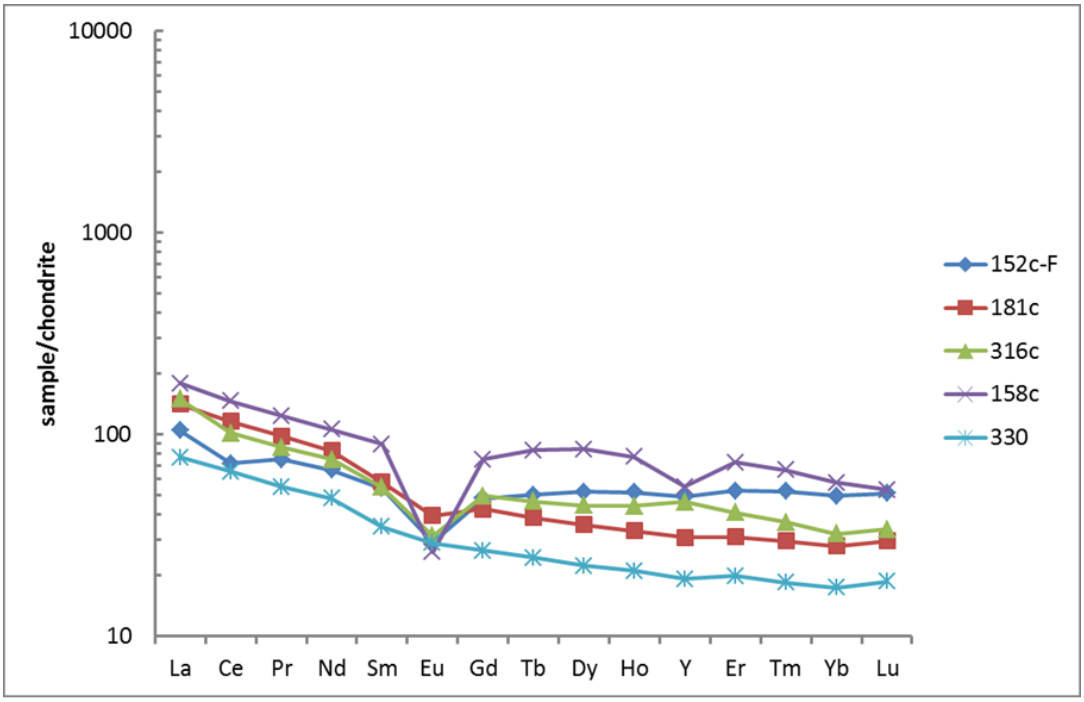

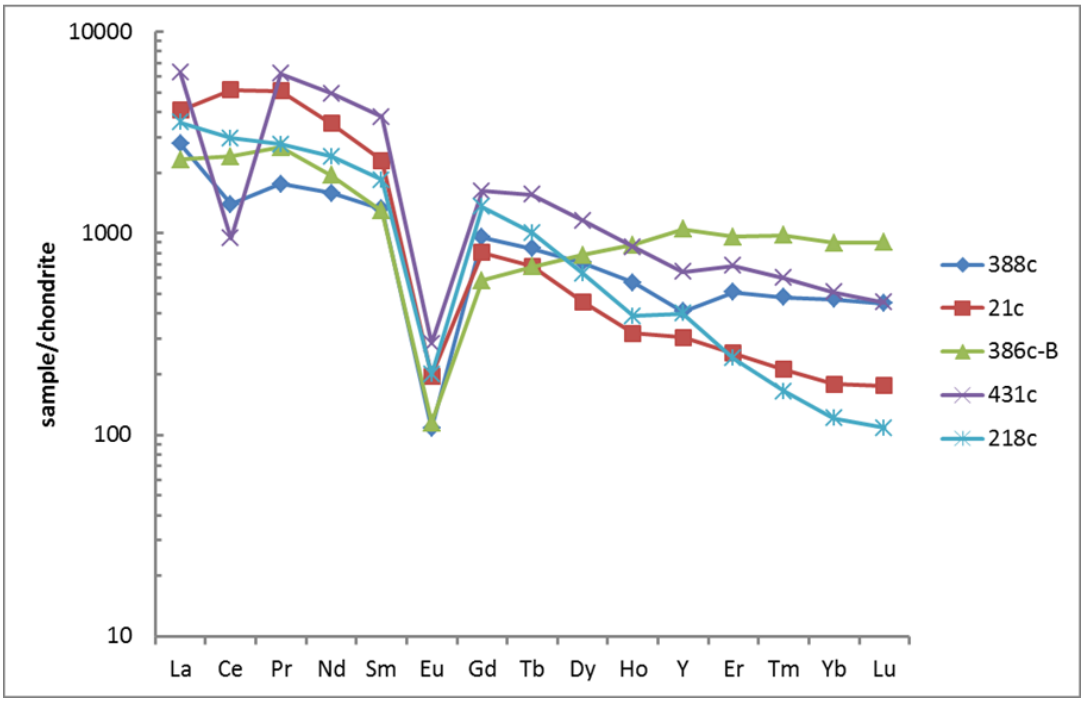

Figure 52: REE diagrams using ICP-MS data of WSU normalized to C1 chondrite values of Sun and McDonough (1989). Low-REE samples (top) begin to develop a Eu anomaly as REE are enriched. Eu anomalies are more pronounced in the high-REE group (bottom), with enrichment of Eu occurring at a much lower rate than for other REE.

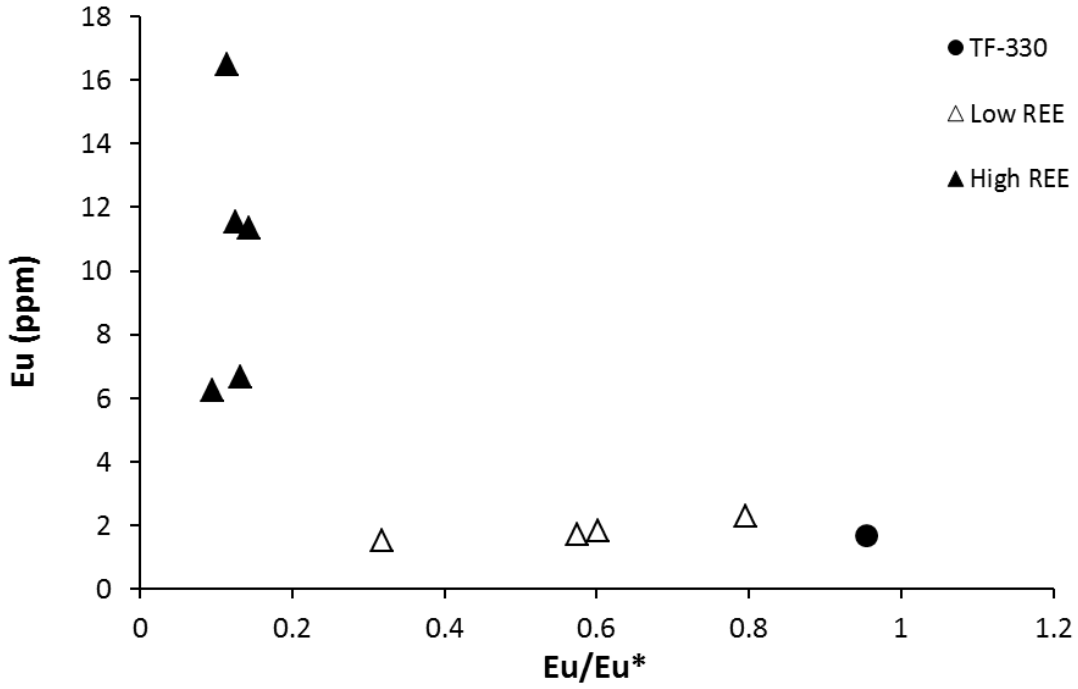

Figure 53: Europium plotted in ppm, versus the europium anomaly for each sample, using ICP-MS data. All high-REE samples show a significant anomaly, while the size of the anomaly in the low-REE group is quite variable.

Between low and high REE samples, the greatest difference in abundances is observed in the LREE, with La concentrations between 552-1491 ppm, compared to that of low REE samples, ranging from 25-42 ppm. In the HREE, the difference is not as great, with sample TF-218c containing only 2.75 ppm Lu, and low-REE clasts containing 0.75-1.35 ppm. Low-REE sample TF-152c-F shows barely a twofold enrichment of La/Lu (2.21), when normalized to C1 chondrite values, while high-REE sample TF-218c exhibits the greatest fractionation between REE (La/Lu (n)=29.98). Average chondrite normalized La/Lu for the low-REE group is ~3.7, compared to ~15.7 for the high-REE samples.

REE-enriched samples show the greatest variation in their relative proportions of HREE (Figure 52, bottom). Sample TF-386c-B exhibits a very flat enrichment trend across the HREE, increasing in chondrite normalized abundance from Gd to Y, with only slight decline from Er to Lu (Er/Lu = 1.06). A similar pattern is exhibited in TF-288c (Er/Lu = 1.14), but at much lower overall levels of enrichment. Samples TF-21c and TF-431c exhibit similar behavior between Er and Lu as well, with somewhat negative slopes (Er/Lu = 1.45 and 1.52, respectively). Sample TF-218c has the steepest slope amongst the HREE (Er/Lu = 2.21), with significantly less enrichment than observed in the LREE.

Relative enrichments in HREE appear to correlate with decreases in Ba/Th between high-REE samples (Figure 54). This phenomenon does not occur in low-REE samples, nor does the relationship exist between HREE and either Ba or Th when compared directly. Two separate trends appear to define the high and low-REE groups, with the most mafic sample, TF-330 showing the highest Ba/Th ratio. These trends may be unrelated, however, as differences in Ba/Th values may be due to magmatic evolution, while Lu is redistributed through hydrothermal processes.

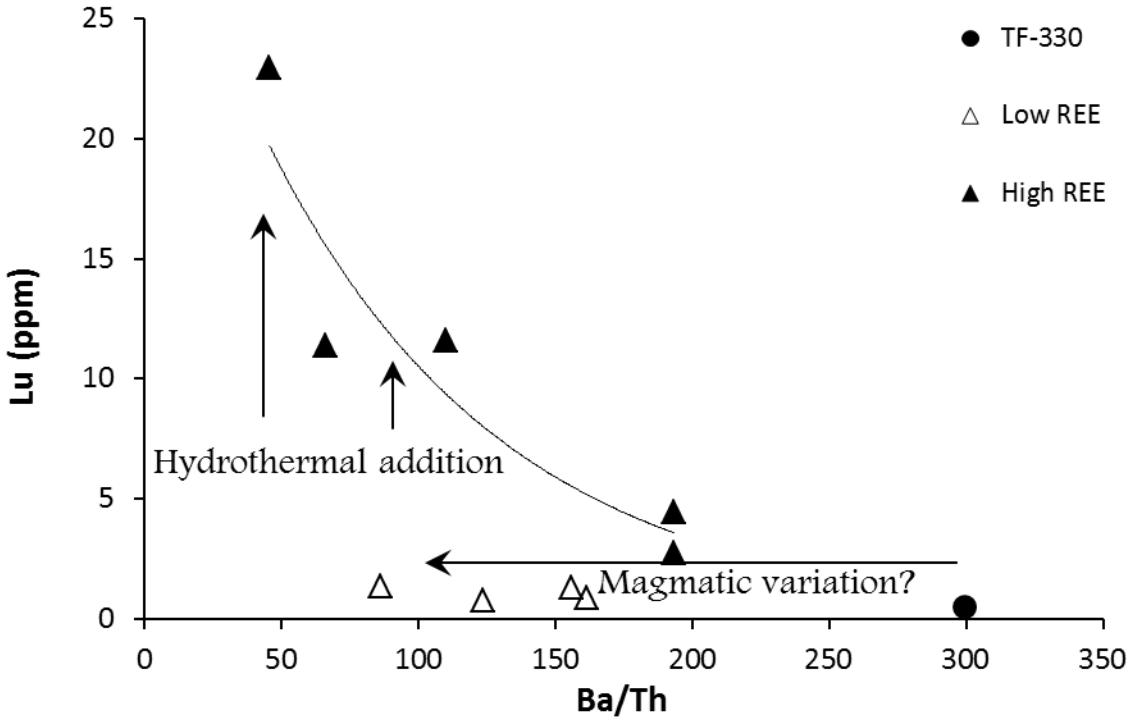

Figure 54: Relative enrichments of HREE display an inverse correlation with the Ba/Th ratio in high-REE mafic clasts. Two rather distinct trend lines can be inferred, each appearing to diverge from lava flow sample TF-330.

The relationship between LREE also differs from sample to sample, with TF-431c exhibiting much less enrichment of Ce than La, with a similar, but less pronounced relationship in TF-388c (Figure 55, top). The negative anomaly in TF-431c is especially notable, due to its greater enrichment in all other LREE, while containing the least Ce. Plots of Ce/La display a significant amount of scatter when viewing all samples, while much less variation is observed for Nd/La (Figure 55, bottom).

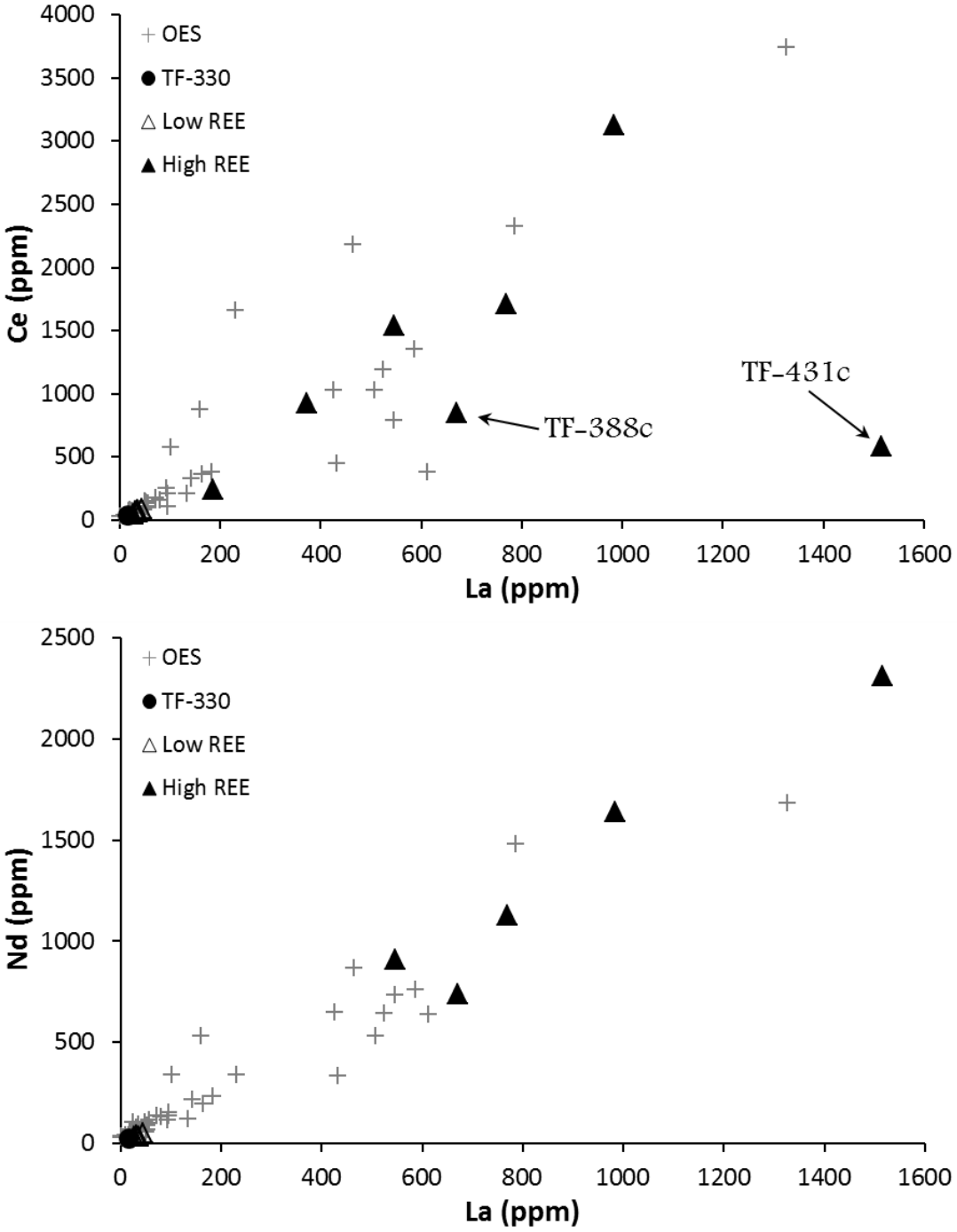

Figure 55: Ce plotted against La in ppm (top), showing significant scatter and one highly anomalous sample TF-431c, with much lower than expected Ce. Nd plotted versus La (bottom) displays a much more consistent relative enrichment., but is does not reach the values for Ce in some rocks. Nd values not available for Ferns data.

2.5 – Discussion

The substantial, but selective enrichment of REE in mafic clasts within Three Fingers caldera appears to be an undocumented phenomenon in the literature. A possible source of REE enrichment must be identified to understand the mechanics by which enrichment took place. In addition, the means of enrichment has implications for the extent of ore-grade REE deposition at this location, and determining the likelihood of similar deposits elsewhere.

2.5.1 – Geographic distribution of mafic clasts

Distribution of mafic clasts within dense glass, monomict glassy breccias, and porous devitrified rhyolites suggest more than one possible mechanism for their dispersal. In the first scenario, the basal vitrophyre may have entrained clastic debris at the land surface as broken fragments of prior lava flows disrupted by upheaval or clastic debris resulting from ring fractures during caldera collapse. The second, more likely scenario is that mafic clasts were plucked from wall rock during ascent of later erupted intra-caldera rhyolites, as fracture zones became active magmatic conduits. In either case, mafic clasts would be abundant in the earliest erupted products, and become nonexistent upsection. Indeed, mafic clasts are typically found in the lower

several meters of intra-caldera rhyolite deposits, and never witnessed in dense devitrified plugs, which are the last erupted lavas. On the other hand, some locations show abundant mafic clasts entrained alongside tuffaceous siltstone in pyroclastic flow deposits, illustrating the possibility that these remnants of previous lava flows were available at the surface during eruptions of intra-caldera rhyolite.

The presence of both siltstone and mafic igneous clasts together is limited to pyroclastic deposits, most commonly overlying beds of tuffaceous siltstone. Several instances of vitric sheets and lenses containing mafic clasts were observed near inferred dome margins, but tuffaceous siltstone is conspicuously absent from these facies. Additional evidence of mafic clasts within vitric autobreccias illustrates the likelihood that these rocks were entrained in the upper reaches of domes and coulees, in some of the earliest erupted lavas. The complete absence of mafic clasts within dense devitrified rhyolite dome cores and overland flows further supports that these clasts do not have a primary magmatic origin within intra-caldera rhyolites. Additional evidence for a clastic origin is the angularity and often flow-banded appearance of these rocks, in contrast to their description as spindle-shaped "basalt bombs", given by Vander Meulen et al. (1989).

Evidence for mafic fault breccias exists adjacent to a basaltic andesite flow in the south central part of the study area. Sitting just below the contact with porous devitrified rhyolite, a 3-4 meter swath of basaltic gravel is exposed at the surface, cross-cut by exposed veins of calcite. The size of these gravels ranges from sub-millimeter to greater than 1 cm in diameter, and suggests that this may have been a source region for the distribution of mafic clasts. The paucity of mafic lavas observed in the study area may reflect that these flows were volumetrically insignificant, limited in aerial extent by paleo-topography, or that current exposures simply reside within fault blocks that are comparatively uplifted compared to general subsidence within the caldera.

2.5.1 - Enrichment of REE due to magmatic evolution

Variation of REE amongst low-REE mafic clasts is taken to be the result of magmatic evolution. Within the low-REE group, including mafic lava flow TF-330, increases in REE correspond with increasing silica content (Figure 56), in addition to decreasing iron, magnesium, titanium, and manganese. The behavior of europium in low-REE clasts likely reflects fractionation into feldspar, as the rest of the REE are enriched during magmatic differentiation (Figure 53). This results in a wide range of values for Eu/Eu* for the low-REE group, while the high-REE samples show very

negative anomalies for Eu with little variance. This most likely represents an overprinting of the original REE signal by a source with an even greater anomaly, obscuring the original variation in enriched clasts.

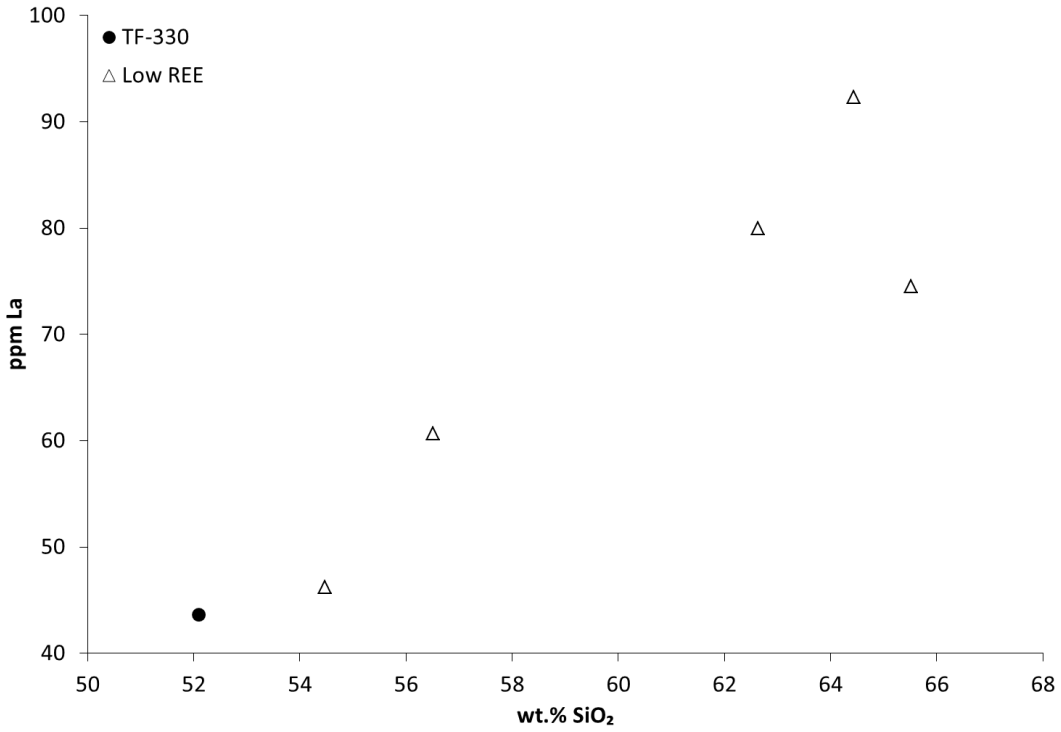

Figure 56: Lanthanum within low-REE mafic clasts increases corresponding to greater silica content, while the high-REE group shows no such relationship. This provides evidence that high REE content within the enriched samples is likely not magmatic in origin.

The high level of variability observed between REE and other trace elements and element ratios, in addition to variations of major elements such as Mn, Al, and Fe argue against a partial melting or fractional crystallization model for extreme fractionation of REE, Pb, and U. Model results for extreme crystal fractionation in a basaltic source rock (in this case, TF-330) are displayed below (Figure 57). To achieve enrichment of REE

observed in high-REE samples would require 98-99% removal of an assemblage of 60% plagioclase, 20% olivine, and 20% clinopyroxene.

At this extent of crystallization, it is highly likely that these magmas would retain similar major element chemistry to their parent magmas. In fact, removal of any significant amount of plagioclase from a parent magma similar to TF-330 would result in the complete depletion of calcium before 10% removal is achieved. In addition, these magmas would likely not reach the surface, due to rheologic lockup at such high proportions of crystallinity.

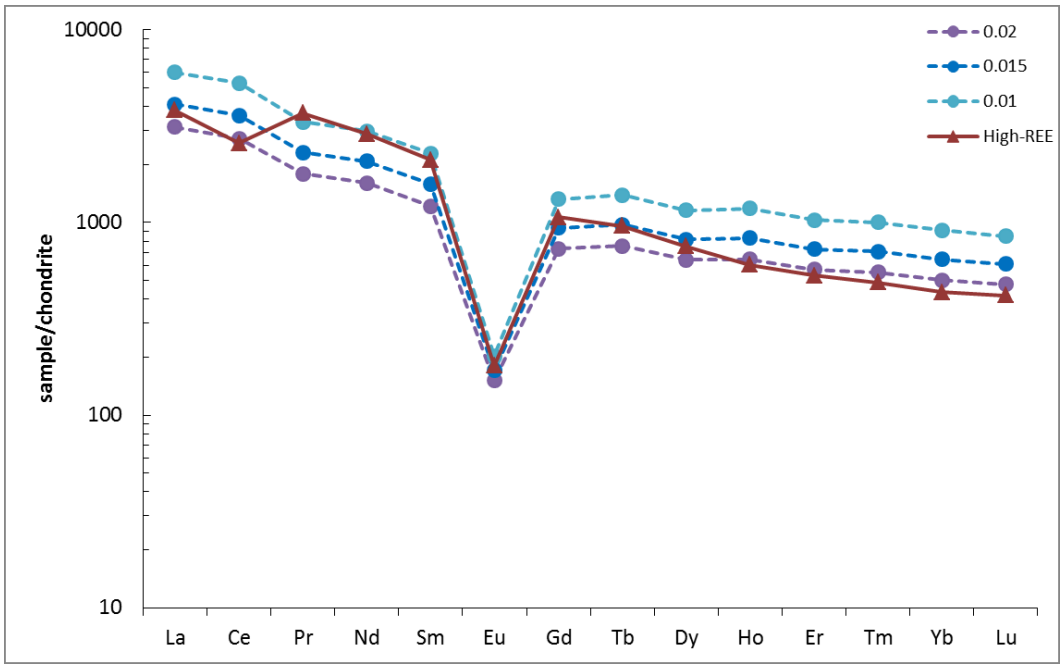

Figure 57: Chondrite normalized REE diagram of model results for fractional crystallization (at 0.01-0.02 remaining melt fraction) of a source containing the REE signature of TF-330. Enrichments of REE near levels observed by average high-REE mafic clasts in this study require very high levels of crystal fractionation, between 98 and 99%. Partition coefficients of McKenzie and O'Nions (1991), chondrite values of Sun and McDonough (1989).

2.5.2 – Enrichment of REE due to hydrothermal processes

Another possibility is that enrichment of REE was facilitated by hydrothermal mobilization of elements. Continued leaching of rocks already enriched in REE by magmatic processes may provide a source for REE inevitably deposited within mafic clasts. Recent studies (Migdisov et al., 2009; Williams-Jones et al., 2012) have confirmed that in acidic environments at elevated temperatures, fluoride and chloride ions readily complex with REE in an aqueous system.

Existence of these conditions within the newly formed intra-caldera setting are likely, as surface waters reacted with fluorine and chlorine gases released during magma ascent and crystallization. Elevated temperatures from high temperature rocks at shallow depths would create a steep temperature gradient, and drive hydrothermal circulation. Leaching would therefore take place in close proximity to vents and plutons, and largely deposition would occur at distal locations, closer to the surface but confined to the area within the caldera.

Under these conditions, circulation of acidic hydrothermal waters through glassy, non-cohesive material may have facilitated significant leaching of elements, including REE. A significant source of this type of material is abundant tuffaceous sediment within the caldera. Stratigraphic relations indicate these sediments were emplaced subsequent to the caldera-forming eruption of the tuff of Spring Creek, but preceding the eruption of clast-bearing intra-caldera rhyolites. The homogenous texture, distinct lack of mineral grains, and fine horizontal lamination of these sediments suggest these are lacustrine deposits of volcanic ash, derived from the tuff of Spring Creek. The lack of phenocrysts suggests that a significant degree of sorting took place, with crystals settling out earlier within a low energy, intra-caldera lake

environment.. Exposures of tuffaceous siltstone are typically silicified, indicating likely percolation of hydrothermal waters during the period of active magmatism within the caldera.

During the course of this study, two lithified sediment samples were processed for geochemical and petrographic analysis. TF-46 was collected from a highly resistant outcrop of tuffaceous siltstone, adjacent to an intra-caldera rhyolite dome structure in the central part of the study area, and is almost entirely devoid of sizeable crystals. TF-407 was collected in the western part of the study area, and contains ~30% rounded to subrounded phenocrysts. This may either represent the crystal-rich base of a well graded sedimentary deposit or deposition in a fluviatile environment where a greater proportion of mineral sands may have been deposited in slightly faster flowing water. If erosion started out with loose tuff of Spring Creek material, the graded lakebed deposit would be more likely.

ICP-MS data for TF-46 and TF-407 indicates relative depletions for the REE from values of the tuff of Spring Creek, most notably in the LREE (Figure 58). Based on the assumption that these sediments were derived from the tuff of Spring Creek, the difference in values between the protolith and the sediment could be taken to represent

leaching of certain elements by aqueous and/or hydrothermal processes. Despite the great difference in crystal content, TF-46 and TF-407 contain very similar proportions of REE.

Differences between the tuff of Spring Creek and tuffaceous sediments are proportionally much greater for LREE, requiring ~50% leaching of REE. To reach the HREE content of tuffaceous sediments, however, requires only ~20% leaching of the tuff of Spring Creek (Figure 58). This difference between the two groups of elements may be due to either differential rates of leaching, or that possibly these sediments were derived from material with a much flatter REE trend. Even at 50% leaching, the very low Eu content of sediments is not approximated, requiring ~70% leaching. This relatively greater removal of Eu may be due to physical sorting processes, in which Eu-rich feldspar was separated from interstitial material relatively enriched in other REE.

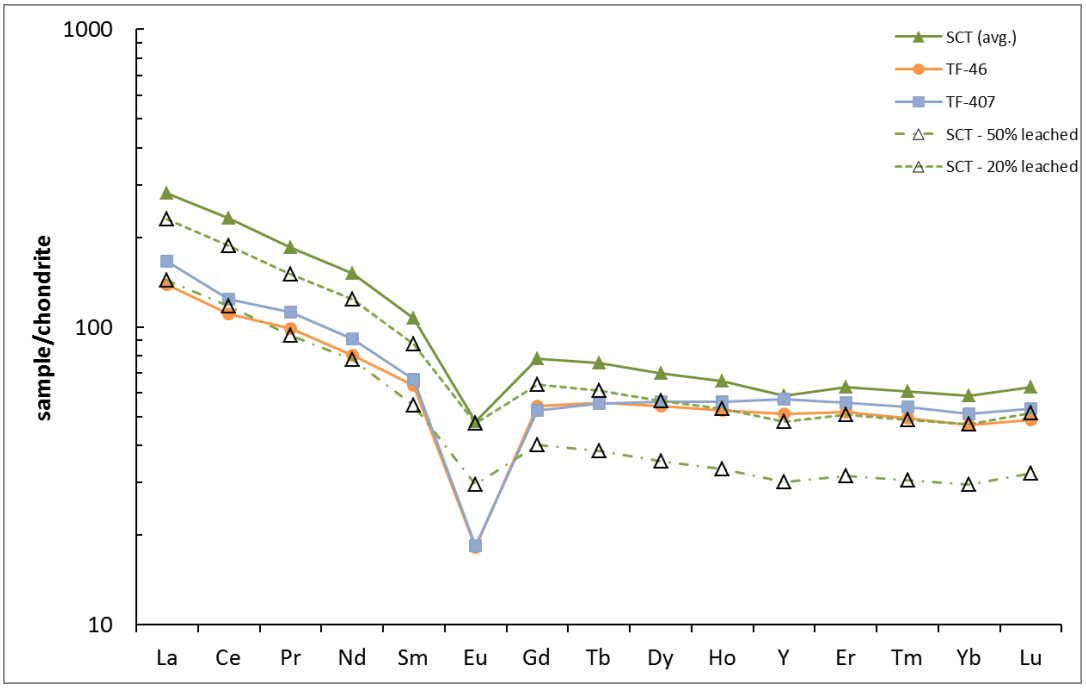

Figure 58: REE values for sediment samples TF-46 and TF-407 are nearly identical, much lower than those for Spring Creek Tuff. While 50% leaching is required for the LREE, only 20% leaching is required to achieve HREE content observed in tuffaceous sediments.

In the following model, the amount of REE lost was calculated from the silicified tuffaceous siltstone (TF-46), and its assumed protolith, the tuff of Spring Creek (Equation 1). These calculated abundances are plotted alongside the actual data on a chondrite normalized REE diagram (Figure 59). Note that the calculated losses of La and Ce are slightly greater than the amount remaining, while HREE were leached to a much smaller extent. Assuming both lava flow sample TF-330, and intermediate low-REE mafic clast TF-181 to represent non-enriched protoliths for high-REE mafic clasts, the concentrations of REE leached from tuffaceous siltstone were added incrementally to the REE concentrations of these samples (Equation 2). Shown below in a chondrite

normalized REE plot, are the original abundances for TF-330 (Figure 60, top) and TF-181 (Figure 60, bottom), alongside average abundances for high-REE clasts and REE concentrations of leachate (blue). The purple line represents the amount of REE lost from sediments multiplied by a factor of 40, and added to REE abundances of TF-330 and TF-181. This calculation assumes that each high-REE mafic clast is mineralized by leachate from a mass of sediment roughly 40 times that of the clast.

– Leaching of REE from the tuff of Spring Creek (SCT)

$$REE_{leached} = REE_{SCT} - REE_{sediments}$$

Example for lanthanum:

$$La_{leached} = 68\ ppm - 33\ ppm = 35\ ppm$$

– Addition of REE to mafic clast from leaching

$$REE_{high-REE} = (REE_{leached} \times 40) + REE_{low-REE}$$

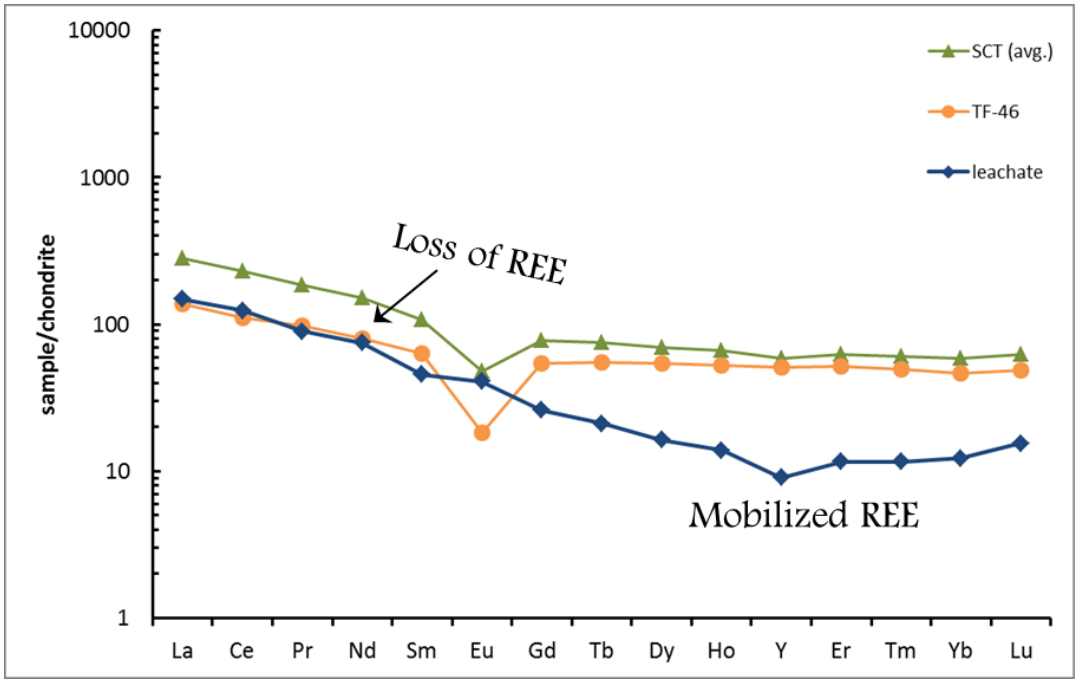

Figure 59: Differences in REE content between tuffaceous sediments (TF-46) from Spring Creek Tuff (SCT) are assumed here to be the result of leaching. Generalized values for the resulting leachate are given for the REE mobilized from SCT.

Results of this model show considerable agreement for most REE, falling in accord with the overall slope of REE abundance in the high-REE samples. Noticeable, however, are some differences in Ce, La, Y, and particularly Eu. The lack of Eu anomaly in model values, compared to the strong negative anomaly in high-REE samples is the most obvious mismatch in this model. Differences in stability for REE in solution with Cl and F may account for some variability in LREE and HREE, but the extreme variation in expected versus actual Eu enrichment is unexplained by these values. It is possible that Eu may not have been mobilized to the degree of other REE, tending to reside in residual phases such as plagioclase or sanidine, where it commonly substitutes for Ca as a 2^{+}

cation. As a result of this fractionation, leaching of glass only would produce a Eu value much closer to those observed in enriched clasts (Figure 61).

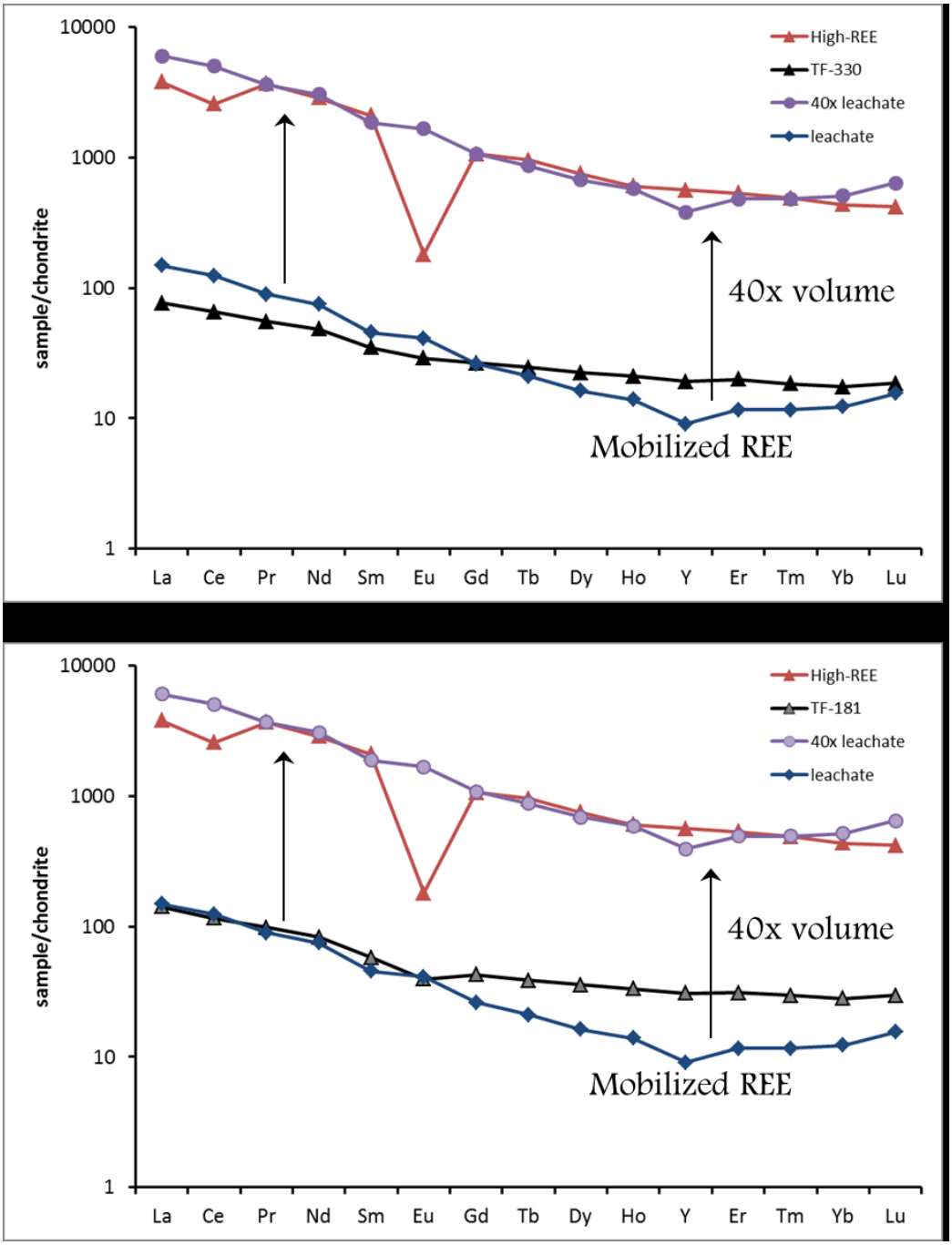

Figure 60: Forty times the concentration of REE within leachate were added to both mafic sample TF-330 (top) and intermediate sample TF-181 (bottom). The noticeable differences in REE patterns of the two protoliths are overprinted by mineralization of such high proportions.

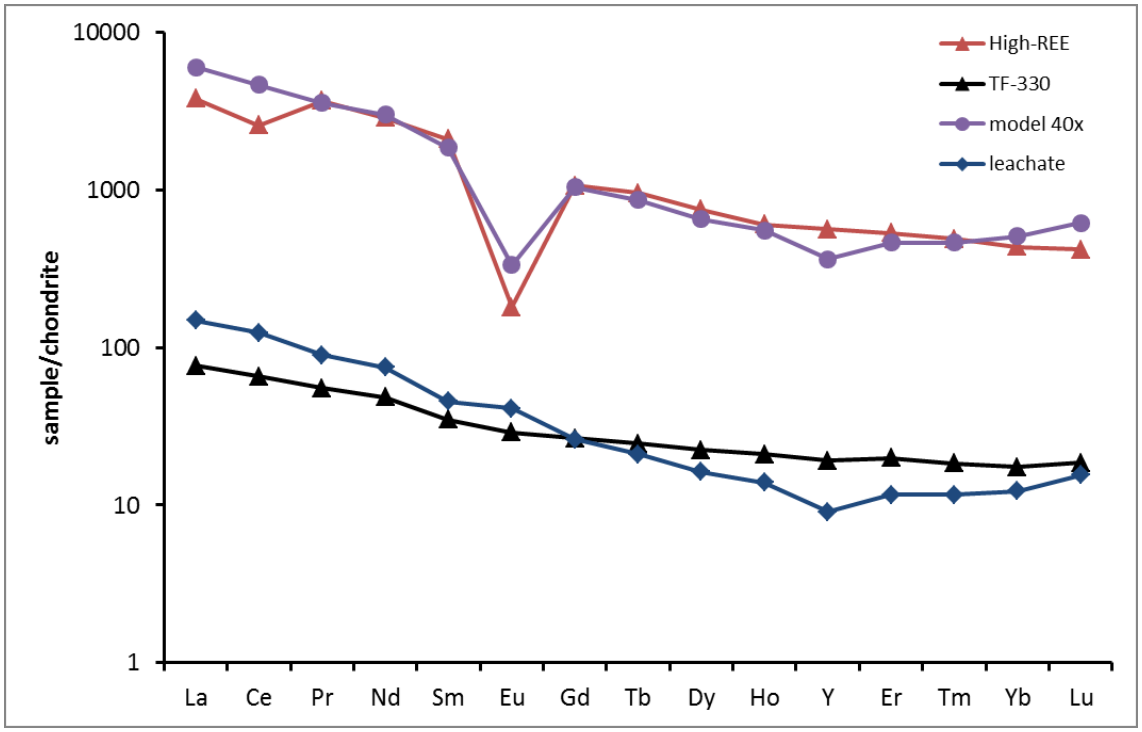

Figure 61: Results of leaching model with 15 percent alkali feldspar in Spring Creek Tuff. If all leaching is assumed to occur within glass, the strong fractionation of Eu into feldspar would significantly reduce its enrichment in mafic clasts. Partition coefficients from Streck and Grunder (1997).

If enrichment of REE in mafic clasts is hydrothermal in origin, a mechanism is required for the precipitation of REE mobilized from other rocks within a closed system. Likely scenarios for deposition of REE in solution with chloride and fluoride ions include increases in pH, lowering temperature, or exposure to higher calcium rocks. With distance from the hydrothermal reservoir, solutions would lose their capacity to hold REE complexes, resulting in mineralization. In the experimental data of Migdisov et al. (2009), prolonged exposure to circulating fluids containing REE complexes may reduce their ability to neutralize acidic, high temperature solutions. The relatively high calcium

content of mafic clasts could facilitate mineralization during water–rock interactions in the subsurface, leading to deposition of REE-bearing minerals on and near the surface exposed to a hydrothermal conduit. The substantial loss of REE from one rock type combined with substantial gain in another suggests a relationship, but the mechanism for redistribution remains unclear.

The mechanism of precipitation of REE in mafic clasts depends largely on the timing of REE mobilization and geographic proximity of the REE source material to the rock unit represented by entrained mafic clasts. In one scenario, mineralization was hosted within a cohesive, mafic to intermediate lava flow, or succession of flows which later were dispersed upon eruption of intra-caldera rhyolites. A second scenario involves in situ mineralization of mafic clasts within their rhyolitic host, a geographic correlation would be expected that is not shown by field evidence. The lack of a clear relationship between enrichment of clasts and geography suggests that REE enrichment occurred prior to clast dispersal, with distribution controlled by volcanic processes at a later time.

As discussed previously, changes in temperature dramatically reduce the mobility of REE in aqueous fluids, in addition to increases in pH and reduced activity of

Cl and F. Contact with Ca-bearing rocks is cited (Migdosov, et al. 2009; Williams-Jones, et al. 2012) to raise pH by providing a buffer to carbonate ions and readily reacting with fluoride ions to form CaF (fluorite) which is relatively insoluble. The very low Ca content in siliceous rocks of Three Fingers caldera may have limited these reactions with REE-laden hydrothermal waters, leaving more mafic rocks as ideal sites of REE mineralization. Average CaO content of mafic clasts sampled is 6.36 wt.% CaO, with the tuff of Spring Creek averaging 0.93 wt.%, and intra-caldera rhyolites at 0.40 wt.%. Phosphate also commonly reacts to form REE minerals like monazite, and the mafic clasts also contain roughly ten times as much phosphorus as their rhyolitic host rocks (0.32 wt.% P_2O_5 versus 0.04 and 0.03 wt.%, respectively).

The availability of calcium and phosphorus may be critical to explain why only mafic to intermediate rocks types experienced noticeable (and quite extensive) enrichment of REE above background levels. In the juvenile intra-caldera environment, a closed system likely existed with continuing circulation of groundwater through sedimentary material at ambient or somewhat elevated temperatures within the caldera moat sequence. Reactivation of intra-caldera faults and ring fractures along regional fault zones likely localized post-caldera magmatic activity, as evidenced by the

predominance of N-S striking rhyolitic dikes and ridges composed of overlapping domes. With the focus of post-caldera magmatic activity along these previously established faults, inputs of heat and volcanic gases would facilitate mineralization within the upper reaches of these zones (Rytuba, 1994). These same structures would also likely localize hydrothermal processes, driven by continued thermal input from a shallow magma chamber below the caldera. Mixing with cooler waters near the surface at more neutral pH would drive precipitation of REE complexes, possibly in combination with availability of Ca and P within these rocks.

Modern studies of REE behavior in hydrothermal systems (Wood and Williams-Jones, 1994; Migdisov et al., 2009; Williams-Jones et al., 2012), in addition to the known fluid-mobile properties of U and Pb (Oliver et al., 1999) in highly concentrated NaCl brines at elevated temperature and low pH provide an argument for enrichment by fluid mobilization. Enrichments of fluid mobile trace elements are accompanied by elevated Na_2O in all but one high-REE sample (Figure 62), compared to values for other samples. The elevated concentrations of these elements without accompanying increases in other trace elements also provide evidence against a magmatic enrichment process.

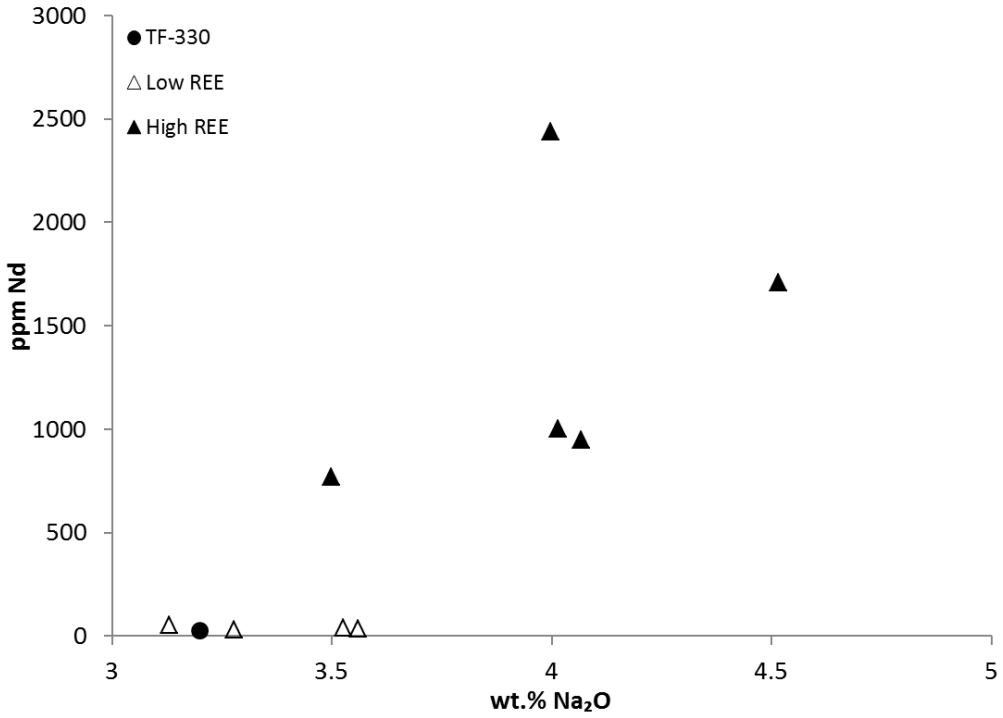

Figure 62: Nd versus Na_2O reveals most high-REE samples are considerably enriched in sodium, possibly a signature of NaCl-rich brines associated with REE mineralization.

2.5.3 – REE enrichment and field relations

The apparent geographic extent of REE-enriched mafic clasts is limited, but this may be due to the limited distribution of the clasts themselves. Few samples were taken outside the central portion of the study area (Figure 40) and the possibility remains that there are undiscovered deposits of REE-enriched mafic clasts. The NNW trend of enrichment suggests that mineralization was related either to volcanism from a particular vent structure, or hydrothermal processes associated with that vent. According to geologic mapping performed for this project and that previous map of

Vander Meulen et al. (1989), this trend follows a continuous ridge of dense devitrified rhyolite. Possibly, this eruption contained greater proportions of volatiles Cl, F, and SO_4 than other intra-caldera rhyolites, increasing the activity of fluoride and chloride species (Weaver et al., 1990).

Variations between relative enrichments of LREE and HREE are currently unexplained, but may correlate with distance from a hydrothermal reservoir. Migdisov et al. (2009) concluded that aqueous complexes of LREE and chloride were more stable than those of HREE (Figure 36). Furthermore, these differences are much greater at elevated temperatures, suggesting that fractionation between REE may occur in hydrothermal systems as a function of increased distance from the source region. High ratios of HREE/LREE, as in sample TF-386c-B may then indicate these rocks were present proximal to the source.

Samples TF-218c, TF-21c, and TF-431c exhibit the expected trend of mineralization at a more distant location, with enrichments in HREE declining from Er to Lu. Following this reasoning, the source region of hydrothermal mobilization may be constrained by plotting element ratios versus geographic location. Those with high

ratios of HREE/LREE would ideally cluster near the source, with lower ratios at increasing distance.

Ratios of HREE/LREE do not give any clear evidence for a centralized source of enrichment, based on stability of chloride or fluoride complexes. When these ratios are plotted geographically (Figure 63), there appears to be no significant relationship between clasts showing greater enrichment in either HREE or LREE. A faint NNW trend indicating high HREE/LREE ratios (green dots) loses significance with the close proximity of samples showing inverse behavior (yellow and red dots).

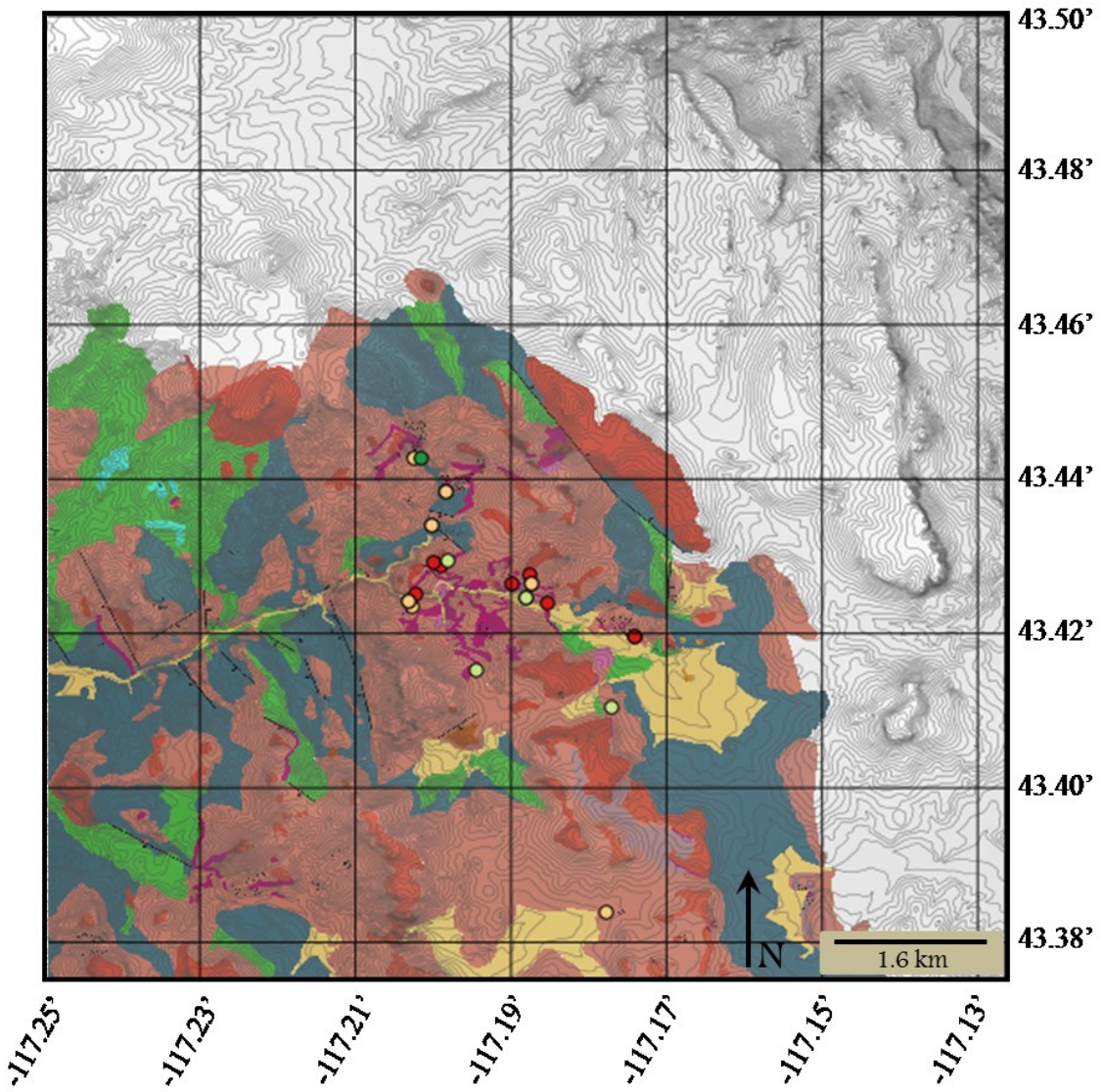

Figure 63: HREE/LREE ratios of enriched mafic clasts, plotted as the total of Er-Lu/La-Nd, on a geologic map of the study area. The trend of REE enrichment is clear from NNW to SSE, but ratios depicting distance from hydrothermal source have no definitive pattern. From highest to lowest ratio of HREE/LREE, dots are dark green, light green, yellow, and red.

Another possibility is more localized hydrothermal diffusion of REE through small fractures observed in intra-caldera rhyolites, each with a unique thermal and chemical fingerprint. Relative enrichments in this scenario would rely on stratigraphic position of both groundwater source and the site of mineralization, in addition to the

hydrothermal gradient, wall rock composition, and porosity of the host for mafic clasts. These factors would have implications for the temperature, pH, and pressure of the hydrothermal waters driving mineralization.

Correlations between Ni and Cu, and their inverse relationship to enrichment of REE may be magmatic in origin, but are also possibly due to leaching by acidic, oxidizing waters. Nickel can be highly mobile under these conditions (Figure 64), and is highly soluble in chloride, NO_3^-, and SO_4^{2-}, and very insoluble in compounds with CO_3^-, OH^-, and PO_4^{3-}. Copper is also mobile under oxidizing, acidic conditions, and is typically abundant in mafic rocks. Though decreases in both elements are typically indicators of increasing silica content, comparatively elevated Cu is often used to discriminate between sulfide deposits and mafic rocks (Salminen, 2013).

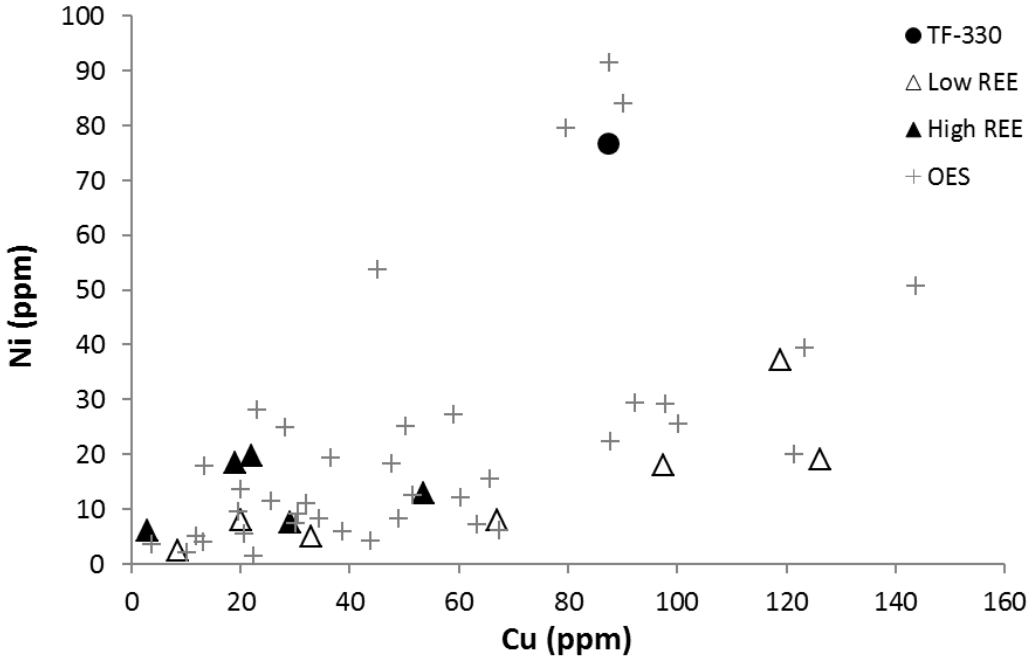

Figure 64: Ni versus Cu displays considerable correlation, but in two distinct trends at higher abundances. A subset of higher Ni samples is clustered near 80 ppm Cu, with most samples showing much less increase in Ni.

Despite their tendency for aqueous mobility, elevated levels of nickel and copper are at odds with fractionation of REE in study samples. Ni is also commonly substituted into olivine for Mg and Fe, and its fractionation typically correlates across these elements. This is not observed in the relationship between Ni and FeO however, where a wide variance in FeO is encountered at low Ni abundances (Figure 65). Another element that is quite compatible in spinel-bearing olivine is Cr, but unlike Ni and Cu is not typically fluid mobile. Comparisons of Cr versus Ni and Cu show no distinct trend, however and the scatter of highly REE enriched rocks argues against extreme crystal fractionation for their enrichment.

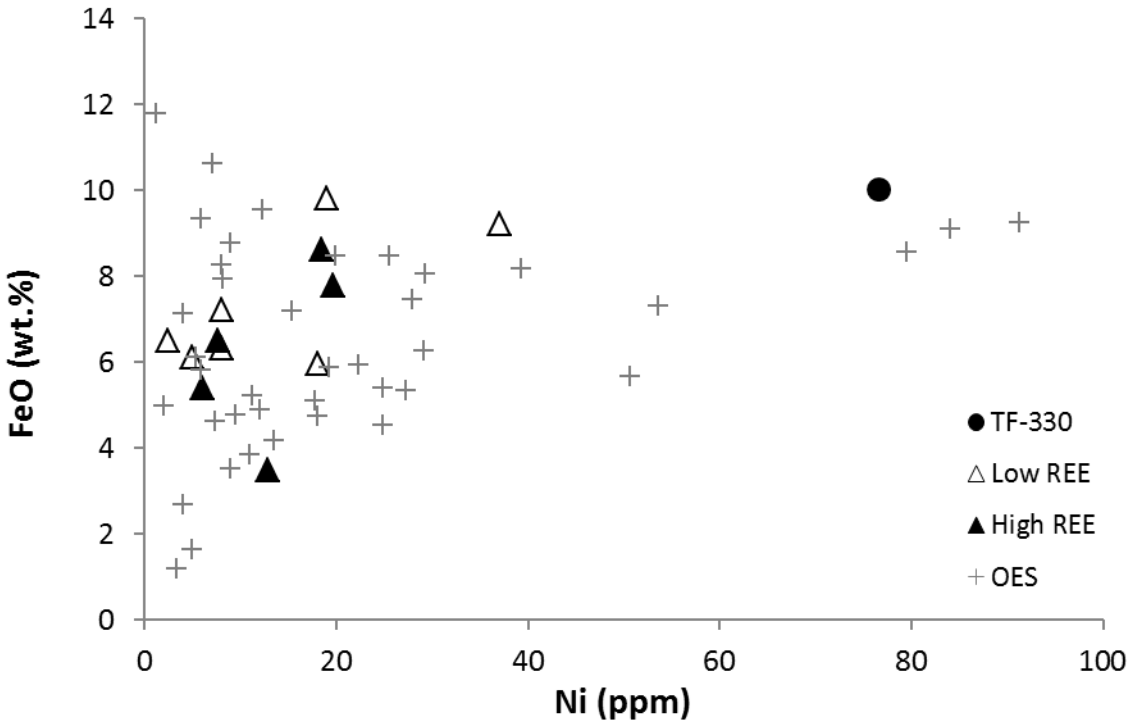

Figure 65: High variation in FeO corresponds to low Ni content in study samples, while high-Ni samples display little variation. Note also the variable distribution of high and low-REE mafic clasts.

2.6 – Conclusions

Enrichment of REE in mafic clasts within Three Fingers Caldera is limited to a narrow NNW striking zone, associated with a series of topographic highs underlain by intra-caldera rhyolite. High and low-REE clasts cover a wide range of major element compositions, from basaltic andesite to dacite, which does not correspond with REE enrichment. Among high-REE samples, significant differences exist in relative proportions of LREE and HREE that also do not correlate with major chemical differences. Steep negative anomalies in Eu are common to all REE enriched clasts, while

low-REE samples show little to no anomaly, suggesting Eu was available in much smaller proportions during enrichment or that reducing conditions induced its fractionation from other REE.

Extreme enrichment of REE in mafic clasts of Three Fingers caldera appears unlikely due to fractional crystallization processes, based on the very high level of crystallization required to produce such enrichments. Enrichments in REE, Pb, and U, combined with the lack of increase in HFSE elements Ta, Zr, Hf, and Ti suggest this is not a product of magmatic evolution, but rather of hydrothermal enrichment, likely involving chloride-rich solutions as the transport mechanism. The lack of correspondence in major element abundances correlates with these findings, showing a range of compositional variations that show no relationship to enrichment of REE.

Geographic distribution of REE-enriched mafic clasts suggests association with a single NNW trending magmatic conduit for eruption of intra-caldera rhyolites. Mobilization of REE and other elements was likely facilitated by hot, acidic solutions rich in chloride and fluoride. Leaching of intra-caldera sediments or silicic igneous rocks by these solutions resulted in the inevitable deposition of REE in mafic clasts. The significantly higher calcium content of mafic and intermediate rocks led to

neutralization of low-pH waters responsible for REE transport, thus becoming sites for mineralization.

Significant variations in LREE versus HREE enrichment are unexplained. Higher relative stability of aqueous LREE suggests that a central source of dispersal may be identified by this ratio, but no clear trend is observed. Therefore, mineralization of mafic clasts is thought to have occurred at a central location, such as within a magmatic conduit where these were originally a cohesive rock unit. Later eruption of intra-caldera rhyolite through this conduit likely plucked mafic clasts from the wall rock, dispersing both high and low-REE rocks fairly randomly in the earliest erupted products of lava flows and domes. This correlates with the relatively high concentration of mafic clasts near the base of intra-caldera rhyolite flows, with none observed in the later erupted, dense devitrified dome interiors.

In the intra-caldera environment following caldera collapse, enrichment may have occurred within a primary fault structure that offset one or more mafic to intermediate lava flows. Continued magmatism beneath the caldera likely provided heat and volcanic gases that were localized along previously established faults, driving hydrothermal activity and leaching of elements from unconsolidated tuffaceous

sediments. Steep negative anomalies observed in Eu are most likely the product of their residence in feldspar phases within the sediments more resistant to leaching, reducing conditions within the hydrothermal system, or physical sorting of Eu-bearing mineral grains from lacustrine deposits.

References

Behrens, H., Zhang, Y., 2009, H_2O diffusion in peralkaline to peraluminous rhyolitic melts: Contributions to Mineralogy & Petrology, v. 157, p. 765–780.

Castor, S.B., 2008, Rare Earth Deposits of North America: Resource Geology, v.58, no.4, p. 337–347.

Chao, E.C.T., Back, J.M., Minkin, J.A., Yinchen, R., 1992, Host–rock controlled epigenetic, hydrothermal metasomatic origin of the Bayan Obo REE–Fe–Nb ore deposit, Inner Mongolia, P.R.C. Applied Geochemistry, v. 7, p. 443–458.

Cordier, D.J., and Hedrick, J.B., 2010, USGS 2008 Minerals Yearbook – Rare Earths (Advance Release), 16 p.

Cummings, M.L., Evans, J.G., Ferns, M.L., and Lees, K.R., 2000, Stratigraphic and structural evolution of the middle Miocene synvolcanic Oregon–Idaho graben: GSA Bulletin, v.112, p. 668–682.

Erickson, M.S., Malcolm, M.J., Hoffman, J.D., and King, H.D., 1986, Analytical results and sample locality maps of stream–sediment and heavy–mineral–concentrate from the Honeycombs (OR–003–77A) and the Owyhee Canyon (OR–003–195) Bureau of Land Management Wilderness Study Areas, Malheur County, Oregon: U.S. Geological Survey Open–File Report 86–628; 48 p., 3 plates.

Evans, A.M., 1987, An Introduction to Ore Geology: London, Blackwell Scientific Publications, 358 p.

Ferns, M.L., 1997, Field trip guide to the eastern margin of the Oregon–Idaho graben and the middle Miocene calderas of the Lake Owyhee volcanic field: Oregon Geology, v.59, no.1, p. 9–19.

Ferns, M.L., and Cummings, M.L., 1996, Geologic Resources of the Vale and Mahogany Mountain 30X60 Minute Quadrangles: State of Oregon Department of Geologic and Mineral Industries open file report 0-94-10.

Haas, J.R., Shock, E.L., Sassani, D.C., 1995, Rare Earth Elements in hydrothermal systems. In: Jones, A.P., Wall, F., Williams, T. (eds)Rare Earth Minerals: Chemistry, Origin, and Ore deposits. Mineralogical Society Series 7, p. 105-150.

Hageman, P.L., King, H.D., Jones, J.L., and Erickson, M.S., 1993, Analytical results and sample locality map of stream-sediment, heavy-mineral-concentrate, and rock samples from the Upper Leslie Gulch (OR-003-074) and Slocum Creek (OR-003-075) Wilderness Study Areas, Malheur County, Oregon: U.S. Geological Survey Open File Report 93-259A, 26 p., 1 diskette.

Ishihara, S., Hua, R., Hoshino, M., and Murakami, H., 2008, REE Abundance and REE Minerals in Granitic Rocks in the Nanling Range, Jiangxi Province, Southern China, and Generation of the REE-rich Weathered Crust Deposits: Resource Geology, v. 58, no. 4, p. 355-372.

Jackson, W.D., and Christiansen, G., 1993, International Strategic Minerals Summary Report – Rare-earth Oxides: USGS circular 930 N.

Jones, A.P., Wall, F., and Williams, T.C., 1996, Rare Earth Minerals: Chemistry, origin, and ore deposits: Bodmin, Cornwall, Great Britain, 372 p.

Lipin, B.R. and McKay, G.A., 1989, Geochemistry and Mineralogy of Rare Earth Elements: Chelsea, Michigan, Mineralogical Society of America, 348 p.

MacDonald, R.W., Baginski, B., Belkin, H.E., Dzier, P., and Jezak, L., 2008, REE partitioning between apatite and melt in a peralkaline volcanic suite, Kenya Rift Valley: Mineralogical Magazine, v. 72, no. 6, p. 1147-1161.

McBirney, A.R., 1984, Igneous Petrology: San Francisco, Freeman, Cooper and Company, 504 p.

McKenzie, D. and O'Nions, R.K. (1991). Partial melt distributions from inversion of rare Earth element concentrations. Journal of Petrology 32: 1,021-1,091.

Migdisov, A.A., Williams-Jones, A.E., Wagner, T., 2009, An experimental study of the solubility and speciation of the Rare Earth Elements(III) in fluoride and chloride-bearing aqueous solutions at temperatures up to 300 ^{0}C: Geochimica et Cosmochimica Acta, v. 73, p. 7087-7109.

Molycorp announces start-up of Heavy Rare Earth Concentrate Operations at Mountain Pass, Calif. (2012). Retrieved August 27, 2013, http://www.businesswire.com/news/home/20120827005952/en/Molycorp-Announces-Start-Up-Heavy-Rare-Earth-Concentrate

Mosander, C.G., 1843, On the new metals, lanthanum and didymium, which are associated with cerium; and on erbium and terbium, new metals associated with yttria: Philosophical Magazine Series 3, v. 23, p. 241-254.

Morteani, G., Preinfalk, C., 1996, REE distribution and REE carriers in laterites formed on the alkaline complexes of Araxa and Catalao (Brazil) *in* Jones, A.P., Wall, F., and Williams, T.C., 1996, Rare Earth Minerals: Chemistry, origin, and ore deposits: Bodmin, Cornwall, Great Britain, p. 227-252.

Murakami, H. and Ishihara, S., REE Mineralization of Weathered Crust and Clay Sediment on Granitic Rocks in the Sanyo Belt, SW Japan and the Southern Jiangxi Province, China: Resource Geology, v. 58, no. 4, p. 373-401.

Noll, P D.; Newsom, H E.; Leeman, W P.; and Ryan, Jeffrey G., "The role of hydrothermal fluids in the production of subduction zone magmas: evidence from siderophile and chalcophile trace elements and boron" (1996). *Geology Faculty Publications.* Paper 165.

Peccerillo, A., Barberio, M.R., Yirgu, G., Ayalew, D., Barbieri, M., Wu, T.W., 2003, Relationships between Mafic and Peralkaline Silicic Magmatism in Continental

Rift Settings: a Petrological, Geochemical and Isotopic Study of the Gedemsa Volcano, Central Ethiopian Rift: Journal of Petrology, v. 44, no. 11, p. 2003–2032.

Reuters News Agency article, 2010: www.reuters.com/article/idUSTRE6AK0R620101121 accessed on 3/18/2011.

Rytuba, J.J., Vander Meulen, D.B., Barlock, V.E., and Ferns, M.L., 1990, Field Guide to hot-spring gold deposits in the Lake Owyhee volcanic field, eastern Oregon: Geology and ore deposits of the Great Basin: Geological Society of Nevada Field Trip Guide 10, 119 p.

Rytuba, J.J., and Vander Meulen, D.B., 1991, Hot-spring precious-metal systems in the Lake Owyhee Volcanic Field, Oregon-Idaho, in Raines, G., Lisle, R.E., Schafer, R.W., and Wilkinson, W.H., eds., Geology and ore deposits of the Great Basin: Geological Society of Nevada, Symposium Proceedings, v. 2, p. 1985–1096.

Rytuba, J.J., 1994, Evolution of volcanic and tectonic features in caldera settings and their importance in the localization of ore deposits: Economic Geology, v. 89, p. 1687–1696.

Salvi, S., Williams-Jones, A.E., 2006, Alteration, HFSE mineralization and hydrocarbon formation in peralkaline igneous systems: Insights from the Strange Lake Pluton, Canada: Lithos, v. 3, no. 40.

Saleh, G.M., 2006, Geologic relationships and mineralization of peralkaline/alkaline granite-syenite of the Zargat Na'am ring complex, Southeastern Desert, Egypt: Chinese Journal of Geochemistry, v. 25, no. 2.

Scaillet, B., and MacDonald, R., 2001, Phase Relationships of Peralkaline Silicic Magmas and Petrogenetic Implications: Journal of Petrology, v. 42, no. 4, p. 825–845.

Schairer, J.F., and Bowen, N.L., 1955, The System K_2O Al_2O_3 SiO_2: American Journal of Science, v. 253, p. 681–746.

Schairer, J.F., and Bowen, N.L., 1956, The System Na_2O Al_2O_3 SiO_2: American Journal of Science, v. 254, p. 129-195.

Shannon, R.D., 1976, Revised effective ionic radii and systematic studies of interatomic distances in halides and chalcogenides: Acta Crystallogr., Sect. A, v.32, p. 751-767.

Streck, M.J., Grunder, A.L., 1997, Compositional gradients and gaps in high-silica rhyolites of the Rattlesnake Tuff, Oregon. J. Petrol., 38: 133-163.

Taylor, R.P., Pollard, P.J., 1996, Rare Earth Mineralization in peralkaline systems; the T-zone REE-Y-Be deposit, Thor Lake, Northwest Territories, Canada *in* Jones, A.P., Wall, F., and Williams, T.C., 1996, Rare Earth Minerals: Chemistry, origin, and ore deposits: Bodmin, Cornwall, Great Britain, p. 167-190.

United States Geological Survey, 2002, Rare Earth Elements-Critical Resources for High Technology factsheet, 4 p.

United States Geological Survey, 2010, Mineral Commodities Summary, 2010, U.S. Geological Survey, 196 p.

Vander Meulen, D.B., Rytuba, J.J., King, H.D., Plouff, D., and Scott, D.F., 1986, Mineral Resources of the Honeycombs Wilderness Study Area, Malheur County, Oregon: U.S. Geological Survey Bulletin 1741-A. 15p.

Vander Meulen, D.B., Rytuba, J.J., Minor, S.A., and Harwood, C.S., 1989, Preliminary Geologic map of the Three Fingers Rock quadrangle, Malheur County, Oregon: U.S. Geological Survey Open-File Report 89-344.

Williams-Jones, A.E., Migdisov, A.A., and Samson, I.M., 2012, Hydrothermal Mobilization of the Rare Earth Elements – a Tale of "Ceria" and "Yttria": Elements, v. 8, p. 355-360.

Wu, C., 2008, Bayan Obo Controversy: Carbonatites versus Iron Oxide-Cu-Au-(REE-U): Resource Geology, v. 58, no. 4, p. 348-354.

Appendix 2A – Geochemical data for mafic clasts

XRF data for mafic clasts

	Ferns data			WSU – this study									
Sample	BBM-01	BBM-04	BBM-05	TF-21c	TF-152c-F	TF-158c	TF-181c	TF-218c	TF-316c	TF-330	386c-B	TF-388c	TF-431c
REE	Low	Med	Low	High	Low	Low	Low	High	Low	Low	High	High	High
XRF – wt.%													
SiO_2	64.97	65.33	62.64	58.06	54.48	64.44	65.51	62.04	56.51	52.09	64.93	55.86	56.02
TiO_2	1.02	1.02	1.46	2.18	1.30	1.19	1.25	1.69	1.38	1.34	1.56	1.30	1.54
Al_2O_3	14.32	13.98	14.76	21.77	16.09	14.90	14.33	20.52	14.86	16.43	16.94	16.64	17.28
FeO*	6.10	6.31	7.20	6.50	9.22	5.95	6.50	3.47	9.82	10.03	5.38	7.77	8.61
MnO	0.15	0.17	0.18	0.10	0.19	0.18	0.16	0.07	0.19	0.19	0.08	0.20	0.26
MgO	1.74	1.76	1.71	0.19	4.20	1.95	1.34	0.37	3.80	6.22	0.19	3.94	2.45
CaO	4.80	4.46	5.95	3.94	9.63	6.62	4.14	5.72	7.97	9.39	3.47	9.00	7.07
Na_2O	3.56	3.51	3.58	4.52	3.28	3.13	3.52	4.01	3.56	3.20	4.07	3.50	4.00
K_2O	3.10	3.19	2.11	2.33	1.29	1.32	2.84	1.73	1.45	0.66	3.04	1.36	2.38
P_2O_5	0.24	0.27	0.41	0.41	0.34	0.32	0.40	0.36	0.45	0.45	0.34	0.42	0.39
XRF – ppm													
Ni	5	8	8	7.6	37.1	18.1	2.5	12.8	19	76.6	6.1	19.7	18.5
Cr	22	8	22	0	121.9	90.7	2.6	124.7	51.2	142.5	2.5	115	52.6
Sc	15	14	24	27.3	34.7	28.9	19.8	26.3	32.9	31.8	9.9	34.8	31.7
V	198	195	302	309.7	277.3	253.1	33.1	204.8	297.4	264.8	235.7	270.8	299.8
Ba	614	769	733	869.2	436.2	448.2	1002.8	541.1	565.2	449.1	830.5	454.3	671.1
Rb	50.7	60.8	41.3	30.8	29.6	17.7	80.8	28.6	52.1	15.7	54.3	23.3	44.5
Sr	260	249	354	371.7	389.1	366.7	310	533.9	355.5	447.5	359.6	376.9	374
Zr	353	289	188	226.9	157.9	217.6	255.9	166.6	202.2	137.2	278.5	186.2	252.4
Y	260.1	121.8	182.5	429.5	76.6	88.5	48.4	537.7	73.2	31.2	1108.4	562.2	822.9
Nb	44.6	32.8	38.4	30.9	22	18.5	15.5	11.7	14	9.2	95.5	32.7	45.2
Ga	28.8	32.8	22	38.3	20	23.1	20	35.5	20.4	17.8	33.6	25.1	36.4
Cu	33	20	67	29.1	119	97.5	8.4	53.6	126.3	87.5	3	21.9	18.9
Zn	195	277	126	1944.8	117.8	156.7	117.2	1829.4	125.9	105.1	177.9	390.8	293.4
Pb	64	45	14	91	7.3	9.1	14.7	79	7.9	4.6	55.7	29.2	49.9
La	186	372	35	984.2	26.7	45.1	32.1	770.2	35.2	15.7	546.1	671.5	1515.4
Ce	241	923	80	3123	46.2	92.3	74.5	1710.5	60.7	43.6	1539.7	849.3	579.7
Th	11.5	11.2	3.8	4.5	2.8	5.2	8.1	2.8	3.5	1.5	18.2	6.9	6.1
Nd				1706.6	31.7	52.3	40.1	1002.7	33	24.5	948.8	770.5	2439.9
U	23.1	11.7	11.1	27.8	7.5	5.4	4.2	4.4	0.6	1.6	34	19.3	47.4
Cs				4.7		0			1.1	0	3	1.5	2.2

ICP-MS data for mafic clasts

	Ferns data			WSU – this study									
Sample	BBM-01	BBM-04	BBM-05	TF-21c	TF-152c-F	TF-158c	TF-181c	TF-218c	TF-316c	TF-330	386c-B	TF-388c	TF-431c
REE	Low	Med	Low	High	Low	Low	Low	High	Low	Low	High	High	High
ICP-MS – ppm													
La				969.9	24.8	42.4	33.6	841.6	35.5	18.2	552.1	661.9	1491.3
Ce				3150.7	44.0	89.7	71.0	1819.2	62.0	40.1	1476.6	854.5	577.5
Pr				482.6	7.2	11.7	9.3	262.9	8.2	5.2	254.0	167.4	589.5
Nd				1640.5	31.1	49.4	38.7	1125.8	35.1	22.5	909.0	739.0	2312.9
Sm				352.5	8.3	13.7	8.9	282.6	8.4	5.3	198.1	202.2	579.1
Eu				11.3	1.7	1.5	2.3	11.6	1.8	1.7	6.7	6.2	16.5
Gd				165.3	9.9	15.5	8.7	279.1	10.2	5.5	120.0	196.8	334.2
Tb				25.7	1.9	3.1	1.4	37.8	1.7	0.9	25.5	31.4	58.4
Dy				116.5	13.2	21.4	9.1	161.3	11.3	5.7	198.7	182.2	295.0
Ho				18.1	2.9	4.4	1.9	22.0	2.5	1.2	49.7	32.3	48.4
Er				42.2	8.7	12.0	5.1	39.7	6.8	3.3	159.1	84.3	114.5
Tm				5.4	1.3	1.7	0.8	4.2	0.9	0.5	25.0	12.3	15.3
Yb				30.3	8.4	9.8	4.8	20.6	5.5	3.0	152.1	79.9	87.1
Lu				4.5	1.3	1.4	0.8	2.8	0.9	0.5	23.0	11.4	11.6
Ba				861.3	435.2	446.6	1045.3	564.0	555.7	441.3	822.7	437.7	652.2
Th				4.5	2.7	4.5	7.6	2.9	4.0	1.4	18.4	5.9	5.3
Nb				30.0	21.0	17.4	15.3	12.2	13.9	8.8	94.7	31.5	44.6
Y				478.2	76.8	86.6	48.4	630.2	72.7	30.1	1650.8	642.6	1012.2
Hf				6.0	4.1	5.9	6.9	4.9	5.3	3.4	7.2	5.0	7.1
Ta				0.8	0.6	0.9	1.0	0.7	0.8	0.5	1.2	0.7	1.0
U				28.0	7.0	5.0	3.4	4.5	1.6	0.5	34.1	18.8	46.3
Pb				97.0	7.5	8.8	14.4	87.9	8.3	4.4	56.8	31.4	57.0
Rb				31.0	29.7	16.9	83.6	31.2	49.9	14.1	56.9	23.8	45.3
Cs				0.8	0.6	0.5	3.5	1.0	2.2	0.5	2.7	0.8	1.7
Sr				388.0	395.8	366.0	321.0	571.3	355.3	441.4	373.4	389.9	390.6
Sc				27.4	35.0	29.3	19.8	27.3	31.8	31.9	10.2	34.4	32.8
Zr				230.7	156.5	212.2	260.0	178.5	196.8	133.4	283.0	184.9	255.6

ICP-OES data for mafic clasts

	TEAL lab – May 2012													
Sample	TF-35c	TF-54c	TF-84c	TF-153c	TF-154c	TF-155c	TF-169c	TF-185c	TF-186c	TF-225c	TF-233c	TF-237c	TF-241c	TF-249c
	Low	High	Low	Low	Low	Low	Low	Low	Low	High	Low	Med	Low	Low
ICP-OES – wt.%														
SiO_2														
TiO_2	1.87	1.87	1.57	1.39	0.84	1.25	1.03	0.89	0.89	1.16	1.33	0.85	0.99	0.83
Al_2O_3	15.80	18.64	14.46	17.22	13.96	15.66	18.94	17.56	19.48	16.51	17.91	15.72	14.32	12.84
FeO*	11.77	4.96	7.13	8.16	5.87	8.05	3.82	7.29	4.51	4.62	7.45	5.08	5.32	5.38
MnO	0.24	0.10	0.13	0.17	0.18	0.24	0.08	0.18	0.13	0.13	0.15	0.10	0.13	0.17
MgO	4.02	0.10	1.72	4.62	2.92	5.15	0.38	4.23	1.17	0.26	4.54	2.51	3.07	3.56
CaO														
Na_2O	3.94	3.99	3.49	3.53	3.47	3.58	3.38	3.35	3.24	3.51	3.70	3.58	3.14	2.84
K_2O														
P_2O_5	0.75	0.34	0.41	0.37	0.24	0.33	0.42	0.18	0.18	0.29	0.42	0.19	0.25	0.20
ICP-OES –ppm														
Ni	1.3	2.0	4.0	39.3	19.3	29.3	11.0	53.7	25.0	7.4	27.9	17.9	27.2	24.9
Cr														
Sc														
V	237.3	252.9	308.2	274.9	155.9	241.3	98.2	162.6	109.4	175.8	241.8	138.4	176.8	151.0
Ba	901.6	851.8	696.1	544.0	375.6	467.7	361.0	255.0	384.9	428.8	391.2	296.0	249.0	224.2
Rb														
Sr	483.8	398.0	355.4	422.0	248.3	358.6	246.6	219.3	193.6	279.9	353.8	215.0	262.6	217.5
Zr	176.1	225.8	153.4	201.2	275.2	212.3	403.0	163.5	180.0	320.0	260.5	424.2	207.8	231.3
Y	41.8	556.7	183.2	1053.9	83.5	206.7	162.4	148.6	270.4	524.4	1464.0	477.9	194.8	161.8
Nb	12.0	67.1	15.0	27.9	29.3	46.0	76.2	20.9	29.9	53.6	45.2	36.7	62.7	23.7
Ga														
Cu	22.4	10.2	43.8	123.5	36.5	92.4	32.0	45.1	50.3	30.2	23.0	13.5	59.0	28.2
Zn	132.6	237.0	134.9	133.4	154.3	146.9	271.4	125.3	195.2	341.3	189.6	241.7	270.2	177.3
Pb	4.4	92.7	13.2	6.8	16.1	6.8	27.3	8.2	9.4	75.1	35.4	48.4	17.1	18.8
La	24.8	785.8	94.9	57.1	57.8	48.5	95.2	53.5	31.4	585.9	143.0	426.1	32.0	81.0
Ce	57.6	2324.2	103.9	98.9	130.1	77.5	209.1	107.7	83.1	1347.9	324.6	1028.6	81.9	158.1
Th														
Nd	104.4	1481.8	150.6	115.1	100.0	102.7	137.2	87.5	77.0	759.7	215.0	647.0	79.1	127.6
U														
Cs														

ICP-OES data for mafic clasts (continued)

	TEAL lab – May 2012													
Sample	TF-35c	TF-54c	TF-84c	TF-153c	TF-154c	TF-155c	TF-169c	TF-185c	TF-186c	TF-225c	TF-233c	TF-237c	TF-241c	TF-249c
REE	Low	High	Low	Low	Low	Low	Low	Low	Low	High	Low	Med	Low	Low
ICP-OES – ppm														
La	24.8	785.8	94.9	57.1	57.8	48.5	95.2	53.5	31.4	585.9	143.0	426.1	32.0	81.0
Ce	57.6	2324.2	103.9	98.9	130.1	77.5	209.1	107.7	83.1	1347.9	324.6	1028.6	81.9	158.1
Pr	16.0	450.0	31.1	27.1	26.1	24.7	29.3	24.9	18.9	195.5	51.4	182.5	19.6	32.4
Nd	104.4	1481.8	150.6	115.1	100.0	102.7	137.2	87.5	77.0	759.7	215.0	647.0	79.1	127.6
Sm														
Eu	1.0	7.5	0.9	0.7	0.5	0.8	0.5	0.3	0.5	5.2	0.7	3.2	1.5	0.6
Gd	17.2	86.7	29.7	61.5	20.4	26.5	30.3	23.7	23.7	138.6	82.0	130.3	21.1	34.0
Tb														
Dy	6.6	82.5	35.7	104.1	17.2	34.4	25.2	22.0	35.7	115.1	178.2	143.5	38.0	35.3
Ho	0.2	17.9	6.7	26.9	2.9	7.0	4.7	4.1	8.2	20.7	50.9	27.5	8.6	6.9
Er	9.3	49.6	23.9	61.2	10.6	22.7	14.5	14.3	22.5	40.3	122.3	55.4	27.6	17.8
Tm	2.9	5.0	3.7	4.6	2.0	2.9	2.2	2.0	2.7	3.2	12.2	5.1	3.7	2.2
Yb														
Lu	1.6	6.1	3.4	3.9	1.5	2.4	2.2	1.5	2.5	3.6	14.5	6.6	4.8	2.1
Ba	901.6	851.8	696.1	544.0	375.6	467.7	361.0	255.0	384.9	428.8	391.2	296.0	249.0	224.2
Th														
Nb	12.0	67.1	15.0	27.9	29.3	46.0	76.2	20.9	29.9	53.6	45.2	36.7	62.7	23.7
Y	41.8	556.7	183.2	1053.9	83.5	206.7	162.4	148.6	270.4	524.4	1464.0	477.9	194.8	161.8
Hf	5.2	6.6	4.0	3.9	7.1	4.7	10.1	3.2	4.5	7.5	4.5	10.3	4.1	4.8
Ta														
U														
Pb	4.4	92.7	13.2	6.8	16.1	6.8	27.3	8.2	9.4	75.1	35.4	48.4	17.1	18.8
Rb														
Cs														
Sr	483.8	398.0	355.4	422.0	248.3	358.6	246.6	219.3	193.6	279.9	353.8	215.0	262.6	217.5
Sc														
Zr	176.1	225.8	153.4	201.2	275.2	212.3	403.0	163.5	180.0	320.0	260.5	424.2	207.8	231.3

ICP-OES data for mafic clasts (continued)

	TEAL lab – September 2012												
Sample	TF-225c-B	TF-276c	TF-288c	TF-316c	TF-320c	TF-323c	TF-327c	TF-329c	TF-333c	TF-355c	355c-C	TF-356c	TF-358c
REE	Low	Low	Low	Low	High	Low	High	Low	Low	Low	High	Low	Med
ICP-OES – wt.%													
SiO_2													
TiO_2	0.86	1.41	0.12	1.37	1.61	1.99	1.68	1.39	2.23	1.10	1.16	1.56	1.94
Al_2O_3	16.57	15.58	5.03	8.60	20.48	18.19	22.78	5.95	10.37	21.36	21.23	8.81	20.27
FeO*	4.72	5.67	1.16	8.45	7.93	9.54	4.77	9.23	10.61	3.52	2.65	8.47	8.25
MnO	0.20	0.22	0.01	0.25	0.16	0.32	0.14	0.26	0.32	0.15	0.10	0.26	0.35
MgO	3.31	1.53	0.13	2.43	1.04	0.69	0.49	3.84	1.29	0.72	0.73	2.31	0.47
CaO	6.55	5.47	0.22	7.74	4.80	4.66	4.60	11.55	3.97	5.06	5.05	7.40	4.66
Na_2O	2.97	3.37	0.20	2.84	4.82	4.55	3.85	3.54	4.52	4.69	4.40	3.39	4.42
K_2O	2.89	3.83	1.94	1.40	3.10	3.88	5.14	0.66	1.65	2.95	3.37	1.42	2.83
P_2O_5	0.15	0.27	0.01	0.32	0.17	0.35	0.11	0.34	0.50	0.23	0.63	0.33	0.47
ICP-OES –ppm													
Ni	18.1	50.6	3.4	19.9	8.2	12.4	9.6	91.3	7.1	9.0	4.0	25.5	8.1
Cr	86.2	110.1	2.6	54.7	58.5	5.8	35.2	166.9	4.4	111.3	89.9	56.8	5.7
Sc	35.3	17.5	1.2	7.2	29.5	18.3	21.1	5.9	3.2	30.9	31.9	5.9	26.5
V	178.1	238.5	8.3	282.9	293.2	384.9	229.0	259.5	347.7	150.9	124.6	322.2	346.5
Ba	345.9	727.3	139.7	457.2	710.6	896.5	742.3	459.8	746.6	409.3	516.9	544.2	882.7
Rb													
Sr	277.4	264.6	12.8	315.0	419.1	420.5	405.2	492.3	542.3	310.4	367.4	368.9	412.2
Zr													
Y	410.0	17.6	102.5	36.1	116.3	107.8	922.7	22.7	2.5	195.1	1610.6	22.1	139.1
Nb													
Ga													
Cu	47.8	143.9	3.9	121.5	48.9	51.7	19.6	87.6	63.3	30.6	13.2	100.2	34.5
Zn	176.5	677.7	57.1	127.6	1393.3	589.6	1116.9	110.7	845.5	502.7	408.7	383.3	477.1
Pb	6.4	3.7	8.4	5.8	53.5	90.6	55.8	3.5	17.6	18.8	222.1	8.7	76.0
La	106.5	7.7	53.5	31.4	559.9	112.2	248.1	17.7	6.2	60.9	1409.2	29.4	174.2
Ce	184.9	19.2	110.1	55.1	872.1	423.2	1219.6	25.6	17.9	105.0	2750.2	59.8	645.4
Th													
Nd	124.9	34.1	59.0	52.5	712.8	372.5	376.5	40.4	35.3	73.2	1864.5	72.5	588.0
U	17.9	17.4	3.2	22.4	22.0	26.6	19.6	27.0	26.8	11.2	19.1	23.1	25.0
Cs													

ICP-OES data for mafic clasts (continued)

	TEAL lab - September 2012												
Sample	TF-225c-B	TF-276c	TF-288c	TF-316c	TF-320c	TF-323c	TF-327c	TF-329c	TF-333c	TF-355c	355c-C	TF-356c	TF-358c
REE	Low	Low	Low	Low	High	Low	High	Low	Low	Low	High	Low	Med
ICP-OES - ppm													
La	94.9	2.2	50.8	24.2	524.5	101.4	231.5	10.2	2.0	52.4	1327.1	21.6	159.5
Ce	251.4	26.0	149.7	74.9	1185.6	575.3	1658.2	34.8	24.4	142.8	3739.2	81.3	877.5
Pr	25.8	6.1	13.5	12.7	164.8	80.0	77.2	10.3	9.2	13.9	378.0	16.4	118.8
Nd	112.7	30.8	53.3	47.4	643.1	336.1	339.8	36.4	31.8	66.1	1682.4	65.4	530.5
Sm	37.7	11.6	28.4	15.6	144.6	99.5	80.4	11.7	3.1	16.5	443.0	16.8	142.3
Eu	1.8	0.7	0.7	1.3	6.4	3.8	8.6	1.4	0.7	1.6	26.1	1.6	5.8
Gd	36.4	11.4	12.3	19.2	103.4	72.4	106.2	17.1	16.8	19.7	390.4	21.3	89.7
Tb	10.3	2.3	4.1	2.1	4.3	5.5	29.5	2.4	2.6	3.5	62.2	2.3	8.1
Dy	48.3	26.1	34.8	27.0	60.2	62.6	139.8	26.1	25.8	31.8	275.6	29.4	79.0
Ho	12.7	9.1	2.7	8.0	17.1	17.1	32.0	6.6	10.3	10.2	46.5	10.2	20.6
Er	36.9	12.3	8.8	13.0	25.6	29.8	80.5	12.0	11.4	19.3	104.4	14.7	44.7
Tm	4.1	4.0	1.6	4.0	4.5	5.1	7.7	4.1	5.2	3.8	6.1	4.1	5.8
Yb	31.8	6.4	10.1	2.9	10.3	15.8	68.5	2.1	0.1	11.6	72.7	4.1	32.8
Lu	5.8	3.0	1.9	1.3	3.8	5.1	12.9	1.9	2.8	3.5	11.6	2.6	7.3
Ba	345.9	727.3	139.7	457.2	710.6	896.5	742.3	459.8	746.6	409.3	516.9	544.2	882.7
Th													
Nb													
Y	878.6	37.8	219.5	76.2	246.5	228.1	1942.6	48.6	4.8	416.8	3385.3	47.0	293.7
Hf													
Ta													
U	17.9	17.4	3.2	22.4	22.0	26.6	19.6	27.0	26.8	11.2	19.1	23.1	25.0
Pb	6.4	3.7	8.4	5.8	53.5	90.6	55.8	3.5	17.6	18.8	222.1	8.7	76.0
Rb													
Cs													
Sr	277.4	264.6	12.8	315.0	419.1	420.5	405.2	492.3	542.3	310.4	367.4	368.9	412.2
Sc	35.3	17.5	1.2	7.2	29.5	18.3	21.1	5.9	3.2	30.9	31.9	5.9	26.5
Zr													

ICP-OES data for mafic clasts (continued)

	TEAL lab - September 2012												
Sample	TF-359c	TF-363c	TF-372c	TF-384c	TF-386c-A	TF-389c	TF-390c	TF-391c	TF-396c	TF-399c	TF-410c	TF-426c	TF-430c
REE	Med	Low	Low	Low	Med	Low	High	Med	Low	Low	Low	Low	Med
ICP-OES - wt.%													
SiO_2													
TiO_2	1.16	1.00	1.81	1.33	1.59	1.38	0.99	0.68	1.19	1.23	1.81	0.82	1.29
Al_2O_3	16.69	15.61	21.13	5.54	18.15	6.23	20.72	14.94	13.09	11.61	15.77	15.51	12.48
FeO*	5.81	4.88	8.77	8.55	6.11	9.09	1.61	4.16	5.92	6.27	9.34	5.22	7.17
MnO	0.22	0.22	0.22	0.22	0.20	0.28	0.05	0.17	0.18	0.20	0.59	0.12	0.30
MgO	2.13	4.20	0.59	3.46	2.52	3.90	0.20	2.93	2.91	2.63	2.55	2.80	2.47
CaO	5.63	7.81	4.83	10.59	7.23	11.23	1.23	5.30	8.93	10.37	5.98	7.19	7.86
Na_2O	3.26	3.72	3.75	2.93	3.93	3.48	3.77	3.45	3.37	3.58	4.03	4.03	2.89
K_2O	3.38	2.50	3.38	0.68	1.83	0.76	3.39	3.26	1.56	1.54	3.43	2.97	1.72
P_2O_5	0.29	0.51	0.05	0.32	0.33	0.33	0.24	0.11	0.24	0.28	0.45	0.16	0.31
ICP-OES -ppm													
Ni	5.9	12.0	9.0	79.5	5.4	84.0	5.0	13.5	22.4	29.2	6.0	11.3	15.4
Cr	9.2	38.9	51.7	123.9	3.4	200.3	48.9	67.1	117.5	111.2	4.0	26.9	52.0
Sc	34.0	33.3	24.8	5.8	37.7	4.1	14.2	15.0	12.9	15.8	26.1	26.1	14.6
V	232.1	192.0	299.7	229.2	307.9	255.3	96.3	124.1	254.2	262.8	282.0	150.6	265.3
Ba	647.6	537.4	669.1	528.0	941.4	460.7	358.3	282.9	432.8	426.0	1062.3	506.9	458.5
Rb													
Sr	300.8	276.0	446.3	523.8	447.4	473.6	113.0	176.3	393.6	385.9	456.8	217.9	306.7
Zr													
Y	1281.5	702.7	148.7	26.2	1019.1	23.2	471.9	233.3	180.5	137.6	89.6	331.1	517.3
Nb													
Ga													
Cu	38.7	60.5	30.6	79.7	20.7	90.2	12.0	20.0	87.8	98.0	67.5	25.6	65.8
Zn	458.0	212.4	459.4	105.3	246.2	114.8	192.2	338.9	246.2	138.3	146.6	156.9	469.0
Pb	34.7	12.1	61.6	3.9	19.5	4.9	29.4	84.0	6.8	6.4	3.9	10.6	18.3
La	461.5	198.8	181.1	15.6	540.9	17.1	494.0	582.3	84.2	42.1	23.2	148.7	662.1
Ce	329.9	281.0	268.5	28.1	752.7	28.5	1601.3	582.1	128.9	63.6	51.6	155.5	280.2
Th													
Nd	366.5	257.3	217.2	40.8	588.0	41.8	958.4	813.0	149.5	101.1	64.2	131.1	707.1
U	22.7	18.9	23.6	23.9	28.4	25.5	12.8	16.9	20.5	19.9	28.0	17.7	24.9
Cs													

ICP-OES data for mafic clasts (continued)

	TEAL lab – September 2012												
Sample	TF-359c	TF-363c	TF-372c	TF-384c	TF-386c-A	TF-389c	TF-390c	TF-391c	TF-396c	TF-399c	TF-410c	TF-426c	TF-430c
REE	Med	Low	Low	Low	Med	Low	High	Med	Low	Low	Low	Low	Med
ICP-OES – ppm													
La	433.0	183.7	164.4	10.8	507.7	11.1	464.2	545.9	73.4	35.8	18.3	135.0	613.6
Ce	448.6	382.1	365.0	38.2	1023.4	38.8	2177.1	791.4	175.3	86.5	70.2	211.4	381.0
Pr	79.2	54.1	51.1	10.2	114.9	10.9	219.2	193.4	30.3	20.2	15.3	27.6	148.4
Nd	330.7	232.2	196.0	36.8	530.6	37.7	864.8	733.6	134.9	91.2	57.9	118.3	638.0
Sm	64.5	77.6	47.3	15.6	156.4	13.0	200.5	161.9	48.0	37.1	21.5	36.5	152.4
Eu	2.7	4.0	2.2	1.4	7.1	1.5	10.9	4.2	1.7	1.4	1.6	1.7	3.4
Gd	67.8	83.5	43.6	16.2	149.2	17.0	125.1	84.6	46.5	32.6	25.5	34.6	144.3
Tb	34.8	20.2	3.1	2.5	32.5	2.5	21.3	7.9	4.3	3.2	2.4	4.8	15.8
Dy	114.9	101.7	40.4	25.6	148.9	25.6	125.4	88.3	67.0	46.8	29.1	40.6	128.6
Ho	25.8	19.4	14.3	7.1	32.2	8.2	25.7	14.1	14.2	10.7	10.8	9.9	20.4
Er	100.7	59.8	25.0	12.2	110.8	12.7	54.8	39.7	39.6	25.8	18.7	25.1	64.5
Tm	8.4	5.2	5.2	4.0	10.2	4.1	4.2	3.8	4.6	3.9	4.8	3.5	5.3
Yb	75.2	37.9	14.9	2.4	116.4	2.6	40.0	33.6	27.2	15.9	7.3	19.1	45.3
Lu	12.4	6.4	4.4	2.0	20.5	2.1	7.5	5.5	5.5	4.1	3.9	3.9	8.0
Ba	647.6	537.4	669.1	528.0	941.4	460.7	358.3	282.9	432.8	426.0	1062.3	506.9	458.5
Th													
Nb													
Y	2695.2	1479.8	316.1	55.5	2129.0	49.4	1006.8	491.2	383.0	292.0	189.8	703.7	1101.7
Hf													
Ta													
U	22.7	18.9	23.6	23.9	28.4	25.5	12.8	16.9	20.5	19.9	28.0	17.7	24.9
Pb	34.7	12.1	61.6	3.9	19.5	4.9	29.4	84.0	6.8	6.4	3.9	10.6	18.3
Rb													
Cs													
Sr	300.8	276.0	446.3	523.8	447.4	473.6	113.0	176.3	393.6	385.9	456.8	217.9	306.7
Sc	34.0	33.3	24.8	5.8	37.7	4.1	14.2	15.0	12.9	15.8	26.1	26.1	14.6
Zr													

Appendix 2B – REE diagrams using ICP-OES data

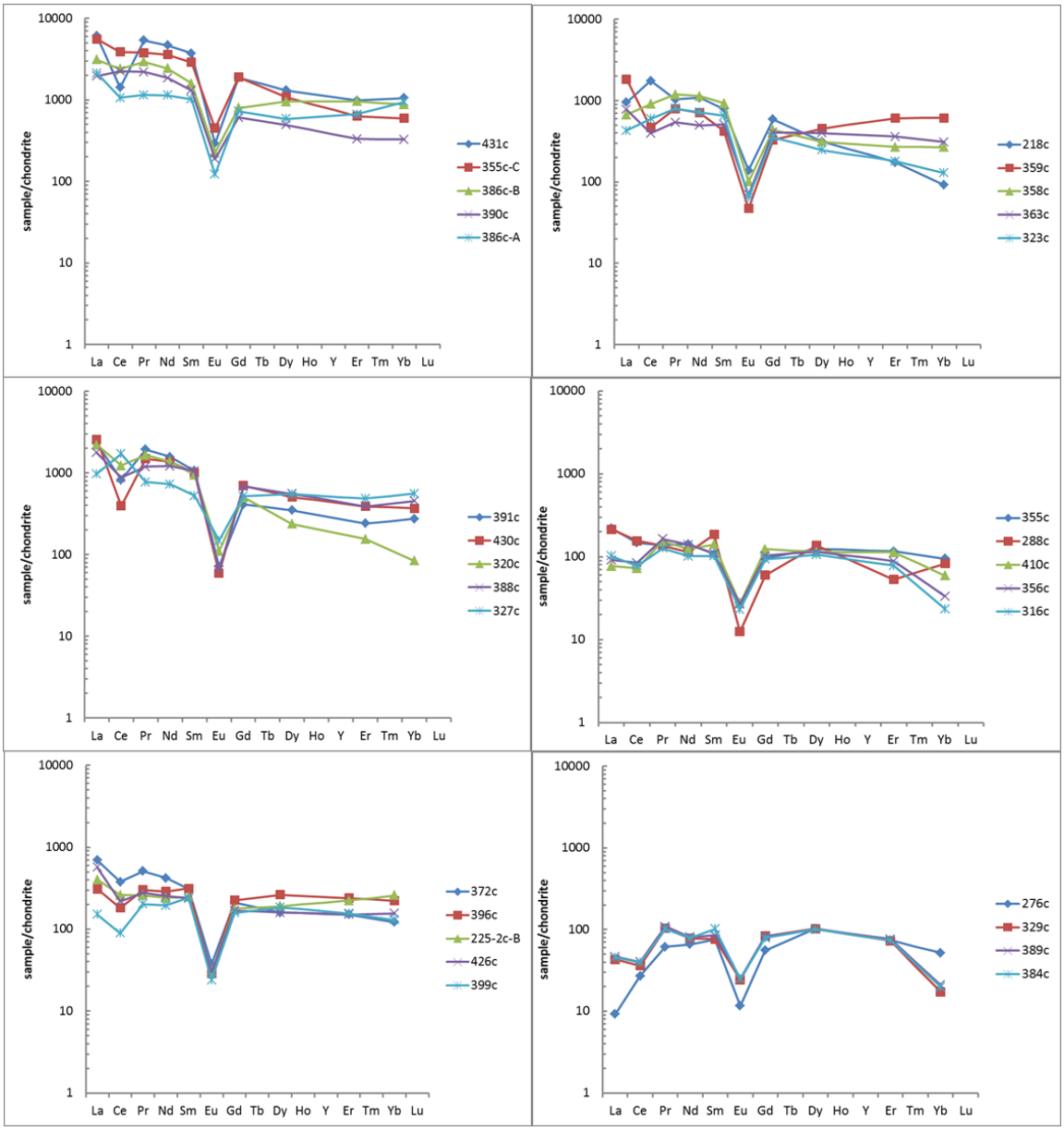

Chondrite mormalized REE diagrams for mafic clasts using ICP-OES data. Chondrite values of Sun & McDonough (1989).